STUDY OF TRANSMUTATION, GAS PRODUCTION AND DISPLACEMENT DAMAGE IN IRON, TUNGSTEN AND CHROMIUM FOR D-T NEUTRON IRRADIATION

By

MAYANK RAJPUT

(ENGG06201504004)

Institute for Plasma Research, Gandhinagar

A thesis submitted to the

Board of Studies in Engineering Sciences

In partial fulfillment of requirements

for the Degree of

DOCTOR OF PHILOSOPHY

of

HOMI BHABHA NATIONAL INSTITUTE

November, 2019

STATEMENT BY AUTHOR

This dissertation has been submitted in partial fulfilment of requirements for an advanced degree at Homi Bhabha National Institute (HBNI) and is deposited in the Library to be made available to borrowers under rules of the HBNI.

Brief quotations from this dissertation are allowable without special permission, provided that accurate acknowledgement of the source is made. Requests for permission for extended quotation from or reproduction of this manuscript in whole or in part may be granted by the Competent Authority of HBNI when in his or her judgment the proposed use of the material is in the interests of scholarship. In all other instances, however, permission must be obtained from the author.

Mayank Rajput

DECLARATION

I, hereby declare that the investigation presented in the thesis has been carried out by me. The work is original and has not been submitted earlier as a whole or in part for a degree/diploma at this or any other Institution / University.

Mayank Rajput

LIST OF PUBLICATIONS ARISING FROM THE THESIS

1. Mayank Rajput, S. Vala, R. Srinivasan, M. Abhangi, PV Subhash, B. Pandey, CVS Rao, D. Bora, "Calculated differential and double differential cross section of DT neutron induced reactions on natural chromium (Cr)," *Indian Journal of Physics 92,1*, pp. 91-96, (2018).
2. Mayank Rajput, S. Vala, PV Subhash, R. Srinivasan, M. Abhangi, R. Kumar, "PKA, gas production and displacement cross section (NRT) for Tungsten and Chromium irradiated with neutrons at energies up to 14.1 MeV," *Fusion Engineering and Design* 130 114–121 (2018).
3. Mayank Rajput, P. Kanth, PV Subhash, S. Vala, R. Srinivasan, "Reproduction of true energy spectrum of charged particles with Monte Carlo method*" Journal of instrumentation* 13 P12030 (2018).
4. Mayank Rajput, PV Subhash, R. Srinivasan, "Displacement damage study of Tungsten, Iron for fusion neutron irradiation", *Fusion engineering and design*, 150 110370 (2020).
5. Mayank Rajput, R. Srinivasan, "study of transmutation, gas production and displacement damage in chromium for fusion neutron irradiation" *Annals of nuclear energy* 138 107187 (2020).

LIST OF PAPERS PRESENTED IN INTERNATIONAL AND NATIONAL CONFERENCES

1. Mayank Rajput et al., Transmutation, gas production and displacement damage in tungsten for fusion applications, *The 17th International Conference on Plasma-Facing Materials and Components for Fusion Applications 2019 (PFMC-17),* Eindhoven University, Netherlands
2. Mayank Rajput et al., "Energy differential and displacement damage cross section of DT neutron induced reactions on fusion reactor materials (Fe, Cr & W*)", Fusion energy conference 2018 (FEC-2018),* Gandhinagar
3. Mayank Rajput et al., "Neutron induced Primary knock-on spectra and displacement damage on fusion reactor materials (W, Fe, Cr) at energies up to 14.1 MeV energy" *30 Symposium on fusion technology (SOFT-2018),* Giardini Nexos, Italy
4. Mayank Rajput et al., "Energy differential cross-section, gas production and displacement cross section (NRT) of Tungsten and Chromium for neutrons of up to 14.1 MeV neutron energy" *International conference on high energy radiation and applications (ICHERA-2017),* MS University Baroda, India
5. Mayank Rajput et al., "Differential and double differential cross sections for neutron-induced reactions on iron, nickel, and chromium" *DAE-BRN Symposium on nuclear physics (2015),* Sri Sathya Sai Institute of Higher Learning, Andhra Pradesh, India

ACKNOWLEDGEMENT

My Ph. D Journey is about to end with many cherishable and unforgettable moments that have shaped me not only into a better researcher but also made me a better individual. There is a lot of scientific and social support from multiple people in this thesis and this thesis can not be completed without acknowledging them.

I would like to express my deep gratitude to my thesis supervisor, Dr R. Srinivasan, Institute for Plasma Research, Gandhinagar, for his valuable guidance not only as a thesis supervisor but also as a mentor. His continuous support and encouragement boost me to complete my Ph. D. Without his guidance and mentorship, this thesis would have not been completed. I would like to express my deep gratitude to my co-guide, Dr PV Subhash, ITER-INDIA, for his continuous scientific and intellectual support. Scientific discussions with him helped me a lot to finish my research work.

It is my pleasure to express my deep gratitude to Prof. Shishir Deshpande, Dr Mainak Bandyopadhyay, Dr Pintu Bandyopadhyay, Mr Sudhirsinh Vala, and Dr Vipul Tanna for their valuable assessment of my work progress and suggestions. Their assessment of my Ph. D work provided me a rightful path that leads to the completion of this thesis.

It is my pleasure to express my deep gratitude to Neutronics lab head, Mr Sudhirsinh Vala and labmates, Mr Mitul Abhangi and Mr Ratnesh Kumar for their scientific and moral support. They always helped me whenever I needed any. It is my utmost pleasure to extend my thank to Dr CVS Rao for providing me an opportunity to work in the field of fusion neutronics at the institute for plasma research, Gandhinagar. I am also very thankful to IPR academic committee for their kind and valuable support during my Ph. D tenure.

I am also very thankful to my friends for their continuous support and love. It is due to them only, this thesis journey was so pleasing and cherishable that it holds a very special place in my life. I am also thankful to my fellow scholars for their kind and social support.

Last but not the least, I would like to thank my family and God for their unconditional blessing and love.

November 2019 Mayank Rajput

Gandhinagar

CONTENTS

LIST OF ABBREVIATIONS

ADP	Angular dependent potentials
ADSS	Accelerated driven subcritical system
Arc-dpa	Athermal recombination corrected-displacement per atoms
ASTM	American Society for Testing and Materials
BCA	Binary collision approximation
BCC	Body centred cubic
BFM	Back shifted fermi gas model
BWR	Boiling water reactor
CMS	Centre of mass system
CTM	Constant temperature model
DD	Deuterium Deuterium
DDX	Double differential cross section
EU DEMO	European demonstration fusion power plant
DFT	Density functional theory
DPA	Displacement per atom
DT	Deuterium Tritium
EAF	European activation files

EAM	Embedded atom model
EDNF	Evaluated nuclear data files
EDX	Energy differential cross section
FENDL	Fusion evaluated nuclear data library
FGM	Fermi gas model
FP	Frenkel pairs
FPY	Full power year
FW	First wall
FWHM	Full width at half maximum
GPA	Gas production per atom
GSM	Generalized superfluid model
HRTW	Hofmann-Richert-Tepel-Weidenmuller
JEFF	Japanese Evaluated fusion files
JENDL	Japanese Evaluated nuclear data library
LAMMPS	Large-scale Atomic/Molecular Massively Parallel Simulator
LDM	Level density model
LSS	Lindhard-Scharff-Schiott
MCNP	Monte-Carlo neutral particles transport

MD	Molecular dynamics
MFP	Mean free path
MPD	Mean per cent deviation
MSD	Multi step direct
NRT	Norgett, Robinson and Torrens
PHWR	Pressurise heavy water reactor
PKA	Primary knocked on atoms
PPM	Part per million
SE	Standard error
SS	Stainless steel
SST	Steady state tokamak
TENDL	TALYS Evaluated nuclear data library
TFP	True flight path
WFC	Width fluctuation correction
ZBL	Ziegler- Biersack-Littmark

SYNOPSIS

Deuterium (D) and tritium (T) are chosen as the primary nuclear fuel in the fusion reactors due to their higher reaction cross-section, lower energy threshold, and higher energy release compared to other nuclear fusion reactions. The D-T fusion reaction produces the 14.1 MeV neutron and 3.5 MeV alpha particle. The reliability of fusion reactor materials depends on our understanding of how the material properties are changed due to the harsh environment of these 14.1 MeV neutrons. These energetic neutrons cause displacement of atoms, produce hydrogen and helium gases, and induce transmutation in the reactor materials. These three important nuclear responses, 1) transmutation, 2) gas production, and 3) displacement damage, have adverse effects on the microstructural and engineering properties of reactor components. The typical fusion reactor materials presently proposed are iron, tungsten and chromium where iron and chromium are used as structural materials and tungsten is used to take high heat load as the divertor material. The reaction channels such as (n,p), (n,np), (n,α) and (n,nα) produce helium and hydrogen gases in the fusion reactor materials as well as transmutate an element into another element of different atomic number and mass thus changes its chemical and other engineering properties. The D-T neutrons produce energetic recoil atoms or primary knock-on atoms (PKA) in target materials. These PKA initiate damage cascade in the reactor materials and produce secondary and other knock-on atoms. At the end of this damage cascade, stable interstitials and vacancies are formed. A pair of interstitial and vacancy is known as the Frenkel pair. The estimation of gas production, transmutation and displacement damage are essential to quantify the lifecycle of various reactor components. Typical limits of dpa are 20 dpa and 40 dpa in the starter and secondary blanket of EU DEMO fusion reactor and after

which blankets are needed to be replaced. These typical limits of dpa can be different for different blanket configurations and neutron spectra. This study is aimed to investigate these quantities of transmutation, GPA (gas production per atom) and dpa (displacement per atom) accurately so that these materials can be used effectively and efficiently in the fusion reactors.

To calculate these nuclear responses, nuclear cross-section data of all the open reaction channels are required. These cross-section data either can be taken from the evaluated data libraries such as the ENDF and TENDL or can be calculated with the nuclear reaction code TALYS-1.8. In the present thesis, nuclear models are optimized for each element of our interest to reproduce the available experimental data. These optimized nuclear models are later used to calculate the cross-section and differential cross section of all the open reaction channels. The discrepancies between the nuclear cross-section data from the evaluated nuclear data libraries and experimental data libraries have been stated. The nuclear reaction cross section and differential cross section data obtained with the optimized nuclear models come out to be in better agreement with experimental data than the nuclear data from evaluated data libraries such as ENDF and TENDL. Based on the optimized nuclear models in the TALYS-1.8 code, the recoil spectra from all the open reaction channels in all stable isotopes of iron, chromium and tungsten have been calculated.

The estimation of GPA and transmutation requires the reaction cross section data of charged particles production reaction such as (n,p), (n,np), (n,α), and (n,nα), etc.. In the previous studies of gas production, helium and hydrogen production in iron were reported. Only helium production was reported for tungsten and chromium. In the present thesis, the nuclear cross section of (n,p), (n,np), (n,α), and (n,nα) reaction

channels in iron, chromium and tungsten have been calculated with the optimized nuclear models. Based on the calculated cross-section, hydrogen and helium production in iron, tungsten and chromium have been predicted for different neutron environments such as neutron spectrum at the first wall armour of ITER and EU DEMO and neutron spectrum at the first wall of EU DEMO. Hydrogen production in chromium and tungsten is reported for the first time in this thesis for the fusion related applications. These values of the GPA have been compared with other results from the existing literature and discussed. For example, helium and hydrogen production in iron at the first wall location of EU DEMO comes out to be 128 appm/FPY and 561 appm/FPY, respectively while Gilbert et al had predicted these values to be 141 appm /FPY and 657 appm /FPY, based on the TENDL-11 data library which was released in 2011. Previous studies of transmutation gave an overview of the overall change in the concentration of natural elements. In the previous studies, important radioisotopes that get produced during the burn-up had not been reported. In the present thesis, transmutation studies in all the stable isotopes of iron, chromium and tungsten have been carried out for the D-T neutrons irradiation with the ACTYS code. The time evolution of transmutated isotopes including the radioactive ones in iron, tungsten and chromium are reported for the first time in this thesis. This time evolution of different isotopes is important in quantifying the radioactive waste and also provide the fraction of impurity elements (transmutated elements), produced during the reactor operations.

The radiation-induced displacement damage is calculated with the displacement damage cross-section. It requires the energy differential cross section of recoil species and the number of Frenkel pair produced by the recoil atom, as the essential input parameters. The energy spectra of recoils can be reproduced from the evaluated nuclear

data libraries using the NJOY, Spectre and PKA-spectra codes and later used to produce the damage matrices based on the Norgett, Robinson and Torren (NRT) approach. Limitations of uncertain nuclear data and outdated damage mechanism used by the NJOY, PKA-spectra and Spectre codes cause an overestimation in the predictions of displacement defects. In the present thesis, the quantification of Frenkel pairs has been carried out with the NRT method, Molecular dynamics simulation (MD simulations) and Arc-dpa approach. The energy spectra of recoils have been calculated with the TALYS-1.8 code using the optimized nuclear models. The available literature on the MD simulations of displacement damage in iron, tungsten and chromium have been explored and it is found that the MD simulations of displacement damage had been carried out for iron and tungsten and had not been carried out for pure chromium. In the previous MD simulations of iron, reported by Stoller et al, electronic losses of PKA energy had not been included in the damage cascade, thus the number of displacement defects were overestimated. In the present thesis, the MD simulations of self or native PKA cascade have been carried out for up to 200 keV damage energies using the LAMMPS code. Energy loss of PKA in the electronic excitations have been calculated using the Lindhard-Scharff-Schiott (LSS) functions and two-temperature method of MD simulations, and are incorporated in damage cascade. Based on the results of MD simulations, constant parameters of the Arc-dpa method have been calibrated which are later used to calculate the displacement damage cross section of iron, tungsten and chromium for neutron irradiation of up to 15 MeV energy. The time evolution of damage cascade has been studied with the MD simulation using the LAMMPS and Ovito codes for iron, tungsten and chromium. The dpa values have been predicted in iron, tungsten and chromium for neutron spectrum at the first wall armour of the ITER

and EU DEMO and the first wall location of EU DEMO. For the first time, values of dpa in iron, tungsten and chromium have been predicted using the MD simulations and Arc-dpa method.

To validate the nuclear models for predicting the recoil spectra, the energy spectra of outgoing charged particles are required. The measured energy spectra of charged particles obtained by the radiation detectors are degraded due to the loss of energy and particles within the target foil, itself. Thus, the measured energy spectra of outgoing charged particles need to be corrected to have the true energy spectrum. A Monte-Carlo method based on the transport of charged particles is developed and validated with GEANT-4.1. This method includes multiple scattering and the concept of true flight path in its approach. The above-mentioned method has been compared with the existing methods used in earlier experiments. The inclusion of the threshold energy of detector setup in our method reduces the noise in the prediction of true energy spectrum at the lower energy region of outgoing charged particles.

Important highlights of these studies carried out in this thesis are;

- The nuclear models are optimized to produce the reaction and differential cross section data of outgoing particles. The nuclear cross section data, obtained with optimized nuclear models are found to be in better agreement with the experimental data than the nuclear data from the evaluated data libraries.
- The transmutation studies of individual isotopes and time evolution of transmutated isotopes (including the radioactive ones) are reported for the first time in this thesis.
- Gas production (helium and hydrogen) cross section obtained with the appropriate nuclear models and prediction of helium and hydrogen production in iron,

chromium and tungsten for typical D-T neutron spectrum have been carried out. Hydrogen production in chromium and tungsten are reported for the first time for the fusion applications.

- The MD simulation of damage cascade in iron, tungsten, and chromium for the damage energies of up to 200 keV have been carried out. The loss of energy of PKA in electronic excitation is included in the MD simulations using the Lindhard-Scharff-Schiott functions and two-temperature method of the MD simulations. This inclusion of energy loss of PKA in the electronic excitation is included in the MD simulation of displacement damage in iron, tungsten and chromium. This energy loss of PKA in the electronic excitations in the damage cascade for iron were not included in the earlier MD simulations. The MD simulations of displacement defects in pure chromium are also reported for the first time in this thesis. Results of the MD simulations are used to calibrate the constant parameters of the Arc-dpa method.
- The calculation of displacement damage cross section is carried out with the NRT and Arc-dpa methods. Based on the displacement damage cross section of iron, tungsten and chromium, values of dpa is predicted in them.
- A Monte-Carlo method based on the transport of charged particles to reproduce the true energy spectrum of charged particles have been developed and validated with the GEANT-4.1.

This thesis is organized as follows; Chapter 1 gives the introduction to the nuclear fusion and important nuclear responses that need to be evaluated to predict the lifetime of reactor components. Chapter 2 gives an overview of existing scientific literature on gas production, transmutation, and displacement damage in iron, tungsten and

chromium. Limitations of the existed work have been detailed in this chapter. Chapter 3 contains the introduction of different nuclear models, level density models. In this chapter, the optimization approach to select and validate the nuclear model are explained for $^{56}Fe(n,n')^{56}Fe$ reaction channel at 14.1 MeV neutron energy. Chapter 4 contains the calculation of reaction cross section and energy differential cross section data of outgoing particles from open reaction channels in stable isotopes of iron, chromium and tungsten. These cross section data are calculated to select and validate the nuclear model for iron, tungsten and chromium. The energy spectra of recoils from all the stable isotopes of iron, tungsten and chromium are calculated and presented in this chapter. Chapter 5 contains the results of helium production, hydrogen production and transmutation in iron, tungsten, and chromium for typical D-T neutron spectra. Chapter 6 contains the results of the MD simulation of damage cascade in iron, tungsten and chromium. The Arc-dpa parameters are calibrated with the results of the MD simulation. The calculation of displacement damage cross section and prediction of dpa in iron, chromium and tungsten are reported in this chapter. In chapter 7, a Monte-Carlo method based on the transport of charged particles to reconstruct the true energy spectrum of charged particles has been demonstrated and explained. Chapter 8 contains the summary and conclusion of this thesis.

LIST OF FIGURES

CHAPTER 1: INTRODUCTION

CHAPTER 3: NUCLEAR CROSS SECTION DATA: INTRODUCTION AND OPTIMIZATION OF NUCLEAR MODELS

CHAPTER 4: CALCULATION OF DIFFERENTIAL CROSS SECTION OF OUTGOING PARTICLE AND RECOILS

LIST OF TABLES

CHAPTER 1: INTRODUCTION

CHAPTER 3: NUCLEAR CROSS SECTION DATA: INTRODUCTION AND OPTIMIZATION OF NUCLEAR MODELS

CHAPTER 4: CALCULATION OF DIFFERENTIAL CROSS SECTION OF OUTGOING PARTICLE AND RECOILS

CHAPTER: 5 GAS PRODUCTION AND TRANSMUTATION IN IRON, TUNGSTEN AND CHROMIUM

CHAPTER: 1 INTRODUCTION

Nuclear fission and nuclear fusion are the two-fundamental phenomena with which nuclear energy can be harnessed to produce electricity and other forms of energy. In the nuclear fission, a heavy nucleus splits into two lighter nuclei along with additional neutrons, whereas in nuclear fusion, two lighter nuclei fuse to form a heavier nucleus. In both nuclear fission and fusion, lightly bound nuclei convert into tightly bound products. It results in the liberation of energy in the form of the kinetic energy of the outgoing particles. This nuclear energy can be converted into electrical energy in nuclear reactors. In the present scenario, nuclear fission-based reactors have a contribution of about 13% of the total electricity production in the world. In the nuclear fission-based reactors, oxides of uranium and plutonium are used as the primary fuel. Uranium has fewer abundances on the earth and plutonium (^{239}Pu) can only be produced artificially in the fission-based reactors using the ^{238}U, the most abundant isotope of uranium. Other limiting factors of the fission-based reactor are the production of long-lived radioactive waste, requirement of fissile fuel, complicated control, and safety requirements. Contrary to nuclear fission, nuclear fusion has the potential to produce green electricity using the isotopes of hydrogen as the primary fuel. Nuclear fusion produces less long-lived radioactive waste and has less complicated control and safety requirements [1]. Nuclear fusion is explained in the next Section 1.1.

1.1 Nuclear Fusion:

In the nuclear fusion, low Z materials (Z<20) of low binding energies are fused to form heavier Z material of higher binding energy and energy is produced in the form of the kinetic energy of reaction products [1]. Nuclear fusion is the source of energy in stars

and has the potential to provide the power to mankind in the future. To achieve nuclear fusion, lighter nuclei are needed to come close enough so that they can interact with each other by overcoming the coulombic barrier between the two positively charged nuclei. To overcome the coulombic barrier between positively charged nuclei, adequate kinetic energy must be provided so that the reaction products can come out via the quantum tunnelling. The threshold energies of different nuclear fusion reactions, their Q values and maximum gain are given in Table 1.1.

Table 1.1: Nuclear fusion reactions with their threshold energies, Q values, and maximum gain

Fusion reaction	Threshold energy (keV)	Q value (MeV)	Maximum gain
$^{2}H+^{3}H\rightarrow^{4}He+^{1}n$	10	17.6	1800
$^{2}H+^{2}H\rightarrow^{3}He+^{1}n$	50	3.2	70
$^{2}H+^{2}H\rightarrow^{3}H+^{1}H$	50	4.0	80
$^{2}H+^{3}He\rightarrow^{4}He+^{1}H$	100	18.3	180
$^{11}B+^{1}H\rightarrow 3\ ^{4}He$	300	8.7	30

Out of above mentioned potential fusion reactions, D(^{2}H)-T(^{3}H) fusion reaction is preferred for fusion reactors due to its low threshold and higher maximum gain [2] and also has a higher reaction cross section compared to other potential fusion reactions. The D-T fusion reaction starts at around 5 keV due to quantum tunnelling and has the highest cross section at around 100 keV energy [2]. At the energy range of 1 to 100

keV, matter exists in the plasma form which is an ionized gas of free electrons and positive ions [1]. To successfully commercialize the nuclear fusion, density, energy of the plasma, and confinement time must satisfy the Lawson criteria as [1], [2];

$$n.\ T.\ \tau_E > 3\ X\ 10^{21}\ keV.\ s.\ m^{-3} \quad (1.1)$$

where n represents the plasma density, T represents the temperature of plasma in keV and τ_E represents the energy confinement time of plasma. The essential requirements to satisfy this criterion are; 1) high Q value of nuclear fusion reactions, 2) high reaction cross section to achieve the high fusion yield, 3) high energy confinement time of plasma, and 4) high density of the plasma. The D-T fuel in the plasma state would need to be prevented from contacting the surface material of the vessel to avoid heat losses thus requires the plasma confinement. To achieve the high yield in nuclear fusion, plasma should be confined for an appreciable time. This confinement can be achieved either with the magnetic confinement or inertial confinement. Both schemes of confinement are briefly explained in the next sections.

1.1.1 Inertial confinement

In this scheme of confinement, the D-T fuel is used in the form of pellets and are bombarded with laser beams to compress the D-T fuel pellets to 10^3 to 10^4 times of its initial density for a very short time-period [1]. At these high densities of D-T fuel, D-T fusion is achieved just before the pellets blow apart and reduce their temperature to the surrounding temperature. In the inertial fusion, the required plasma density (n) and confinement time (τ_E) are of the order of 10^{25} cm^{-3} and 10^{-11} s, respectively. In this approach, the D-T fuel assembly consists of an inner shell of D-T gas surrounded by the D-T fuel layer with the outermost layer of high Z material. To achieve the high

threshold energy and temperature to attain nuclear fusion, these fuel capsules need to be bombarded with the huge amount of energy (to heat 1 mm diameter fuel assembly, 10^5 Joules energy is required) supplied by the drivers. This energy must be supplied in a very short time-period of about 10^{-12} seconds and energy distribution should remain as symmetrical as possible [3]. Due to the bombardment of this enormous energy, ablation occurs and the outermost part of the fuel assembly which is made up of high Z material, blasts off. Following this, the D-T fuel layer is accelerated inward to the centre of the fuel assembly. As the D-T fuel accelerated towards the centre of the fuel assembly, it is compressed to high densities and temperatures. This compression generates the shock waves which further drive the fuel to thermonuclear densities and temperature and cause ignition at the centre of the fuel assembly. Following the ignition, fusion energy is released in the outward direction and overcome the imploding waves. Inertial confinement can be achieved with lasers, electron beam and ion beam. Inertial confinement fusion consists of following stages; 1) Interaction phase, 2) Compression phase, 3) Deceleration phase, 4) Ignition and burn up phase. In this scheme of nuclear fusion, the radius of the fuel assembly decides the confinement time (for 100 μm, τ_E comes out to be 10-20 ns) [3].

1.1.2 Magnetic confinement

In the magnetic confinement, plasma is confined in the vacuum vessel using the suitable magnetic fields [1], [4]. In the plasma state, a magnetic field bends the ion and electrons trajectories into a helical path around the magnetic field lines. Due to this magnetic field, charged particles move freely in a longitudinal direction but are restricted in the perpendicular direction. This concept of the closed orbit is best observed with the ring-shaped or doughnut-shaped magnetic lines. Doughnut shaped vessels are the best suited

for confining plasma in a magnetic field for a longer time-period of few seconds. In the magnetic confinement, the gases of deuterium and tritium are injected into the torus-shaped vacuum vessel. Magnetic fields are produced by passing the electric current on the coils which are wound on the torus. Plasma current also creates a poloidal magnetic field which along with the toroidal field tends to confine the plasma inside the vessel. Such a device is known as tokamak and this device is extensively studied worldwide [5]–[7]. A tokamak machine based on the toroidal and poloidal magnetic field is being constructed as International thermonuclear experimental reactor (ITER) [8]. ITER is a joint venture of 35 nations including the European Union, India, China, Russia, Korea, United States of America and Japan. ITER will be the first device that will check the technological and material limitations to achieve nuclear fusion and will provide the pathway to various commercial fusion reactors such as the European DEMO, Indian DEMO, etc. India also has its fusion program started with the steady-state tokamak -1 (SST-1). It is a steady-state tokamak, capable of producing single and double null plasma. As a second step to Indian fusion program, SST-2 is planned and it will be a D-T fusion reactor of 100 MW thermal fusion power. The SST-2 will provide scientific and technological input and expertise to Indian Demo fusion reactor. Indian Demo fusion reactor will produce 1GW electrical power. Its lifetime is estimated to be 40 years. To successfully construct and operate such a huge fusion device, various fundamental physics and technological advancement are required and being explored in the field of physics modelling, superconditing magnets, divertor, and radiation resistant materials. Due to the higher gain, high fusion reaction cross section and comparatively low threshold energy for fusion, the D-T fuel cycle is opted as the primary fusion fuel and is detailed in the next section.

1.2 D-T fuel cycle

Deuterium is an isotope of hydrogen and constituent of sea-water with the ratio of 1:6500 with hydrogen. Equivalently, 1 kg deuterium can be extracted from 30,000 kg of seawater. The extraction of deuterium is carried out with the isotope separation method. Tritium is another isotope of hydrogen and does not occur naturally on the earth. It can only be artificially produced from various nuclear reactions. Due to its rare resources available for fusion reactors, it is essential to produce tritium in the fusion reactor, itself. This production of tritium often known as tritium breeding and can be done using the blankets of lithium. Lithium has two isotopes, ^{6}Li (7.59 %) and ^{7}Li (92.41 %). Each of them can produce tritium but with different neutron energies as given in the following nuclear reactions [1], [2];

$$^{7}_{3}Li + ^{1}_{0}n \text{ (High energy neutrons)} \rightarrow ^{3}_{1}T + ^{4}_{2}He + ^{1}_{0}n \quad (1.2)$$

$$^{6}_{3}Li + ^{1}_{0}n \text{ (Thermal energy neutrons)} \rightarrow ^{3}_{1}T + ^{4}_{2}He + 4.38 \text{ MeV} \quad (1.3)$$

The neutrons from $^{7}_{3}Li$(n,T)n reaction are further thermalized and react with $^{6}_{3}Li$. The interactions of thermal neutrons with the $^{6}_{3}Li$ again produce tritium. This tritium will be extracted and used in the fusion reactor at later stages. This D-T fuel produces a 14.1 MeV energy neutron and 3.5 MeV alpha particle. These high energy neutrons and their impact on reactor materials are explained in the next section.

1.3 Fusion neutrons

Nuclear fusion of deuterium and tritium produces a 3.5 MeV energy alpha particle and 14.1 MeV energy neutron. This alpha particle will further heat the plasma. Plasma will remain ignited only when heating by the alpha particles exceeds the heating losses in plasma. Neutrons as uncharged particles cannot be trapped in plasma thus come out

from plasma and interact with the plasma-facing components and other structural materials. The energy of neutrons cannot be extracted directly due to their uncharged nature. These energetic neutrons also interact with the lithium blanket and breed tritium. Neutrons also lose some fraction of their energies as they transport in different mediums of fusion reactors. ITER machine will be the 500 MW thermal power fusion device having the source strength of 1.77 x 10^{20} neutrons.sec^{-1} [9]–[11]. The proposed EU Demo fusion reactor will be the 1600 MW thermal power plant having the source strength of 5.6 X 10^{20} neutrons.sec^{-1} [8], [9]. They will be the first of their kind devices to check the limitations of existing materials, technologies and will address the requirement of technological advancement to achieve the commercial success of nuclear fusion [8]. These high energy neutrons of 14.1 MeV can transport through the structural materials without getting absorbed. The neutron spectra at different locations in ITER (DT and DD campaign) and EU Demo fusion reactor are presented in Figure 1.1. These neutron transport studies of fusion reactor [9]–[11] confirm that high energy neutron spectrum will be available to all the structural materials of ITER and upcoming fusion reactors. These energetic neutrons can cause transmutation, gas production and displacement damage in the fusion reactor materials. These effects are explained in the next sections.

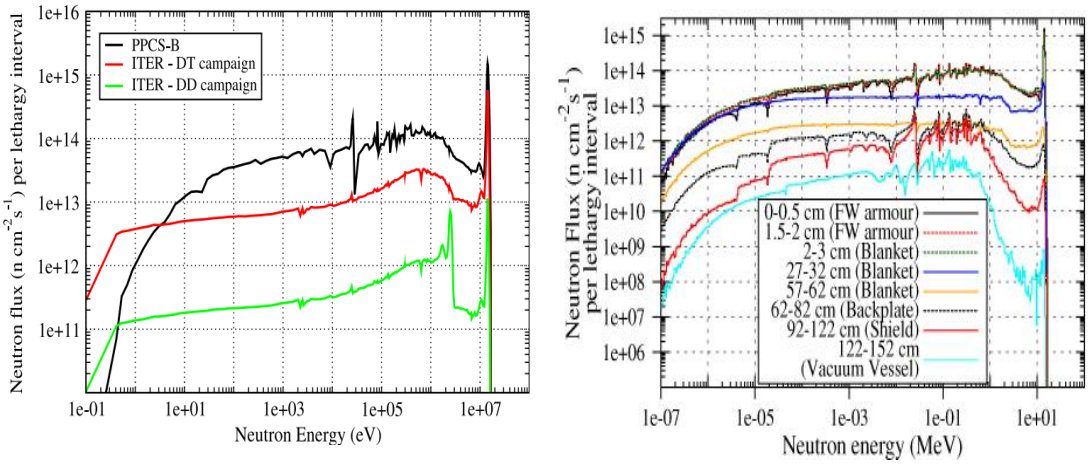

Figure 1.1 Neutron spectra at the first wall armour of ITER (DT & DD campaign) and EU Demo fusion reactor (Courtesy of Gilbert et al [9] [12]).

1.4 Primary effect of neutrons on fusion reactor materials

Neutrons interact with the materials either via scattering or absorption. Due to high energies of D-T neutrons, reaction channels e.g. (n,n'), (n,p), (n,α), (n,np), (n,γ), (n,nα), (n,2n), and (n,d) are open for the interaction of D-T neutrons with the fusion reactor materials. These reaction channels produce energetic outgoing particles e.g. scattered neutrons, protons, alpha particles and gamma rays. The scattered neutrons further transport in the surrounding materials and interact with them until they are absorbed in the material or leave the materials. As neutrons are the chargeless particles, they cannot directly transfer their energy to surrounding materials but can produce charged particles. The outgoing charged particles such as protons and alpha particles transfer their energy to surrounding materials and cause nuclear heating. This nuclear heating by the charged particle is an important parameter to accurately estimate the heat generated by the D-T fusion. Recoil atoms of different mass and energies are also produced along with the outgoing particles. These energetic recoil atoms are the first atom those are shifted from their origin, thus act as the primary knock-on atoms. These primary knock-on atoms

initiate the displacement damage cascade and lead to the production of interstitials and vacancies. In the charged particles production reaction channels, the parent element converts into another element following neutron absorption. This neutron-induced phenomenon of conversion of an element into another element is known as a nuclear transmutation. Another important neutron effect on the structural materials is the gas production and it happens when charged particle such as protons and alpha particles are produced. These charged particles become hydrogen and helium by picking up electrons while slowing down in structural materials. These nuclear responses such as transmutation, gas production, displacement damage occur in the following order;

1. Interaction of neutrons with target atoms and the production of outgoing particles & energetic recoils
2. Transmutation of an element into another element through reaction channels of charged particles production, through inelastic scattering, radiative capture and (n,2n) reactions with subsequent alpha or beta decay
3. Production of hydrogen and helium as protons and alpha particles pick up electrons while slowing down in the target
4. Formation of damage cascade after generation of recoil nucleus which acts as primary knocked on atom
5. Formation of stable defects such as interstitials and vacancies, both collectively known as Frenkel pairs

Different types of nuclear reactions, transmutation, gas production and displacement damage have been explained in the upcoming sections.

1.4.1 Types of nuclear reactions

The very first step to study the nuclear responses in the fusion reactor materials is to study the neutron-induced reactions in the fusion reactor materials. Neutrons can interact with the target nuclei via scattering and absorption. In the scattering interactions, energy is exchanged between the target and projectile and gets redistributed between outgoing or scattered particles and recoil nucleus. After the scattering interaction, a neutron is deflected at some angle with the reduced energy. The scattering interactions are of two types namely, elastic scattering and inelastic scattering. In the absorption nuclear reaction, an incident neutron is absorbed in the nucleus and new particle is emitted. These types of reactions are briefly explained in the next sections. Due to the high energy of DT neutrons, reaction channels e.g. (n,2n), (n,α), (n,p), (n,d), (n,np), and (n,nα) are also open [13]. These reaction channels are not open for many structural materials in fission-based reactors as these reaction channels have reaction threshold of several MeVs. All these open reaction channels complicate the prediction of nuclear responses and need to be modelled as accurately as possible. In the next section, different reaction channels are detailed;

1.4.1.1 Elastic scattering

Neutrons being the uncharged particles can interact with the nucleus of target material via two-body scattering. In the elastic scattering of a neutron, It is scattered at an angle θ from the target atom with no loss or gain in kinetic energy in the centre of mass system (CMS). To study the radiation damage, the energy transferred to the atom of target lattice is an essential input parameter. Incident neutron of energy (E_i) transfers a fraction of energy (T) to the recoil atom which acts as a primary knocked on atom (PKA). The energy differential cross section of recoil atom is needed to predict the number of

Frenkel pairs [14]–[17]. Elastic scattering cross-section of neutron-induced reaction can be explained and calculated with shape elastic scattering (direct reaction mechanism) and compound elastic mechanism [18]. The direct, compound and pre-equilibrium reaction modes are the modes of nuclear reaction and are explained in detail in Chapter 3.

1.4.1.2 Inelastic scattering

In the inelastic scattering, incident neutrons or any other particles interact with the target nucleus and get scattered with reduced energy [18]. The emission of lower energy neutron leaves the target nuclei in an excited state. The excited target nucleus comes to the ground state by emitting one or two gamma photons. Thus, in inelastic scattering, a fraction of energy of the incident neutron is used to excite a target nucleus which later comes to the ground state by emitting gamma photons and lower energy neutron. In this process, energy does not remain conserved. A lower energy neutron, gamma photons and recoil nucleus are formed in the inelastic scattering.

1.4.1.3 Absorption reaction channels

The absorption reactions are those, in which neutron or projectile is retained by the nucleus and new particles are emitted. The nuclear fission, radiative capture, charged particles production reaction are the types of absorption reaction channels. The radiative capture and nuclear fission occur at relatively low energy neutron irradiation while charged particles production reaction and (n,2n) reactions occur at high energy neutrons irradiation. Nuclear fission with slow and high energy neutrons is limited only to high Z materials of actinides family. In the (n,γ) or radiative capture reaction, neutrons are absorbed in the target nucleus and form an excited nucleus. This excited nucleus comes

to the ground state via emitting gamma photons. The charged particles production reaction or (n,p) and (n,α) reaction channels only take place if produced charged particles have sufficient energy to overcome the coulombic potential while coming out from the nucleus. The charged particles production reactions with the slow neutrons are only possible for low Z materials for which coulombic potential is small for the charged particle to come out from the nucleus [14]. For the high energy neutrons (>1 MeV), the (n,p) and (n,α) reaction channels are open for medium to high Z materials. The (n,2n) reaction is another absorption reaction where neutrons of high energy (>10 MeV) are absorbed in the nucleus and two lower energy neutrons are emitted. Other absorption reactions that could also take place for high energy neutrons (>10 MeV) are (n,np) and (n,nα). The charged particle production reactions transmutate an element into another element and also produce helium and hydrogen gases in the target materials. All these reaction channels produce energetic recoil atoms which lead to the damage cascade. These nuclear responses are explained in the next section.

1.4.2 Transmutation and gas production

The charged particle production reaction channel e.g. (n,p/np) and (n,α/nα) converts an element into another element of decreased atomic number, thus changing its isotopic and chemical composition over a long period of neutron irradiation. This process is known as transmutation. The transmutated element can also be radioactive. The transmutation has adverse effects on the reliability of the structural materials as chemical, mechanical and thermal properties of the alloys are changed after long neutron irradiation. The transmutation which changes the original composition of structural alloys affects the engineering properties of alloys due to the accumulation of transmutated impurities. These impurities are produced via the transmutation and can

drastically affect the intended performance of structural alloys under neutron fluence. It was studied earlier that the neutron irradiation equivalent to 52.1 dpa on pure tungsten, converted 5% of pure tungsten to rhenium and tantalum [19]. M. Fujitsuka et al [20] reported that this 5 % conversion of pure tungsten into rhenium would decrease its thermal diffusivity to half. Due to their huge impact on the performance and reliability of structural elements, estimation of transmutated products are essential. Similarly, these transmutation impurities tend to change the electrical resistivity of W-Os alloy [21]. This transmutation and gas production is not much critical in case of the fission-based reactor as the available neutrons in fission based reactors are up to 2 MeV energy and these charged particles reaction channels have threshold of several MeV in many structural elements. These transmutated elements if radioactive raise another issue of radioactive waste disposal and are needed to be quantified accurately using the accurate nuclear models and parameters. The produced charged particles such as proton (^1_1H) and alpha particles (^4_2He) pick up electrons while slowing down in the surrounding material and become hydrogen and helium gas. Helium and hydrogen even in the low quantities have adverse effects on the lifetime and strength of structural components due to their low solubility in metallic lattice. They also tend to form clusters and accumulate at the grain boundaries thus eventually lead to the swelling or embrittlement in the structural alloys. Helium and hydrogen available in the large fraction in the structural alloys can enhance the microstructural changes such as the creation of helium and hydrogen bubble and interstitial loops. These gaseous bubbles result in the surface roughness, void swelling and intergranular embrittlement [22]. These helium and hydrogen productions are often quantized by the gas production per atom (GPA) and need to be evaluated to predict the lifetime of reactor materials.

1.4.3 Radiation induced damage in fusion reactor materials

The energetic radiations such as neutrons, charged particles and gamma photons when interacting with the atoms of a target material, transfer a fraction of their energy to the atoms of target material based on their interaction mode. Atoms in the target which were initially at equilibrium now gain some kinetic energy and get shifted from its origin. The first recoil atom that receives energy from nuclear reaction acts as the primary knocked-on atom (PKA) and tend to interact with the other atoms in the solid lattice. If the energy of recoil or PKA exceeds the threshold displacement energy of that target, then it shifts other atoms from their equilibrium position. PKA creates other knocked on atoms and initiates the displacement damage cascade. This displacement cascade continues until the energy of all the atoms becomes less than the threshold damage energy of the target. Any atom leaving its origin creates a vacancy and if occupies in between the location of other atoms creates an interstitial. The interstitials and vacancies are collectively known as the Frenkel pairs and this phenomenon is known as the displacement of atoms. The damage mechanism, caused by the neutron irradiation is more complicated due to its uncharged nature and multiple probable reaction channels. Neutrons interact with the target atoms and produce an outgoing particle and recoil atom. The outgoing particle may be a scattered neutron, charged particle or gamma photon and deposits its energy in the target material to cause electronic excitations and nuclear heating. Recoil nucleus of different mass and energy are produced along with these outgoing particles and cause displacement damage. The displacement damage which is quantized by the displacements per atom (dpa), can cause different phenomenon such as swelling, phase change, growth of cracks and segregation, etc. The radiation induced segregation which is the phenomenon of redistribution of alloying

elements at a certain location occurs at large extent due to the neutron irradiation at higher temperatures. This displacement damage affects the microstructural and engineering properties of target lattice and has adverse effects on the integrity and reliability of structural materials. These effects are needed to be evaluated for designing radiation-resistant alloys and to predict the life cycle of structural materials in the fusion reactors. The prediction of dpa values is the first and essential step to study the radiation induced effects and to quantitatively compare two materials under same or different neutron spectrum. The damage mechanisms can be classified into two stages namely, primary and long scale damage, based on their time scale. In the primary damage stage, surviving Frenkel pairs are formed and it lasts up to nanoseconds. The long scale damage is due to the interaction of defects with each other and can last from nanoseconds to months. The dpa values can be calculated with the Norgett Robinson and Torrens (NRT) [23], binary collisional approximation (BCA) [24], athermal recombination corrected dpa (Arc-dpa) [25] and Molecular dynamics (MD) simulation [26]. All these methods have been explained in detail in Chapter 6.

1.5 Energy loss correction of charged particles

The accurate nuclear cross section and differential cross section data of outgoing particles are essential input data to predict the transmutation, gas production and displacement damage. All these nuclear responses will only be calculated accurately if accurate nuclear data is available. To validate the nuclear models and parameters for these calculations, reaction and energy differential cross section of outgoing particles e.g. protons, neutrons, and alpha particles need to be measured experimentally. The measurement of energy differential cross section (EDX) of outgoing charged particles plays an important role in the studies of nuclear reaction modes and treatment of cancer

using the neutrons beams. During the experimental measurement of EDX of outgoing charged particles, energy spectra of charged particles are downgraded in their energy and numbers due to their slowing down and absorption in the target foil. This loss of energy and charged particles need to be corrected to obtain the accurate differential cross section data. This phenomenon of energy loss is explained in Chapter 7. Soderberg et al [27], Rezentes et al [28], Slypen et al [29] and Pomp et al [30] had solved this problem by solving the Fredholm equations [31]. In the present thesis, a Monte-Carlo method based on the transport of charged particles is developed and demonstrated. This proposed method includes multiple scattering of charged particles with the atoms of the target foil. The proposed method has been demonstrated in Chapter 7. The proposed method of true energy reconstruction has been validated with the GEANT 4.1 and has been tested for different charged particle species e.g. protons and alpha particles.

1.6 Motivation

The nuclear responses e.g. transmutation, gas production and displacement damage, take place in the fusion reactor materials. These nuclear responses affect the engineering and microstructural properties of fusion reactor materials, thus affecting their lifetime and strength. The estimation of transmutation, gas production and displacement are essential for the reliable operation of the fusion reactor. Iron, tungsten and chromium are important materials for fusion reactors. Tungsten is the primary candidate to be used at the divertor location and iron and chromium being the constituents of stainless steel (SS) are used as the structural materials of fusion reactors. The D-T neutrons induced reactions produce helium and hydrogen gases. These reactions also change isotopic compositions of stable isotopes and induce displacement damage in the lattice of reactor materials. All of these alterations are essential to be quantified with accurate nuclear

models and precise damage mechanisms. Due to the lack of experimental data available for whole D-T neutron spectrum, several evaluated data libraries are produced to provide the nuclear data for fusion related applications. These nuclear data libraries show some discrepancies with the existing nuclear cross section data. Similarly, damage mechanisms that were used in the previous studies of defects have some well-known limitations. These limitations and shortcomings of previous works on nuclear responses are detailed in chapter 2. In this thesis, these nuclear responses have been studied using the accurate nuclear models and advanced damage mechanism.

The energy differential cross section (EDX) of outgoing charged particles are required to optimize the nuclear models for damage evaluation and is also important to study the different nuclear reaction modes. The EDX of outgoing charged particles, measured by the silicon surface barrier detectors are degraded in the energy and number of particles and need to be reconstructed to obtain true energy spectrum of charged particles. Previously, this reconstruction of the true energy spectrum of charged particles was carried out using the statistical methods using the Fredholm equation. In this thesis, this problem is tackled with the Monte-Carlo approach based on the transport of charged particles. The objectives of this thesis are given in the next section.

1.7 Objective of this thesis

Various structural alloys in the ITER machine and other upcoming fusion reactors e.g. European (EU) DEMO, Indian DEMO will be facing the high energy neutron flux of $\approx 10^{15}$ neutron/second at the first wall. These high-intensity neutrons produce different outgoing particles and recoil species of different mass and energy. The nuclear reaction cross section data of all the open reaction channels are required to evaluate the gas

production and transmutation in the structural elements. This nuclear reaction cross section data can be experimentally measured or can be predicted with the nuclear reaction codes such as the TALYS-1.8 [32] and EMPIRE-3.2 [33]. To calculate the dpa values in the structural materials, EDX data of recoils and the number of Frenkel pairs produced by the energetic recoils are essential input parameters. In the present thesis, the transmutation, gas production and displacement damage in iron, tungsten and chromium are studied using the nuclear data calculated with the TALYS-1.8 code and damage matrices obtained with the NRT, MD simulations and Arc-dpa method. Objectives of this thesis are given below;

1. To validate the nuclear models and parameters to predict the double and energy differential cross section of outgoing particles and their comparison with the existing evaluated and experimental data
2. To calculate the energy differential cross of protons, neutrons, alpha particles and their associated recoils
3. To estimate the transmutated products, produced in the charged particles production reaction channels and subsequent decay of reaction products from all the stable isotopes of iron, tungsten and chromium
4. To calculate the hydrogen and helium production cross section and prediction of GPA in iron, tungsten and chromium for the first wall neutron spectra of fusion reactors
5. To carry out the MD simulation of self recoil in iron, tungsten and chromium to study the displacement damage cascade and time evaluation of interstitials and vacancies

6. To calibrate the constant parameters of arc-dpa method and calculation of displacement damage cross section of iron, tungsten and chromium for neutron irradiation of up to 15 MeV with arc-dpa and NRT methods
7. To predict the values of dpa in iron, tungsten and chromium for fusion neutron spectrum of ITER and EU DEMO fusion reactor
8. To develop a Monte-Carlo method based on the transport of charged particles to reconstruct the true energy spectrum of charged particles

1.8 Contribution of this thesis

Major scientific contributions of this thesis are given below;

1. The nuclear cross section data such as the reaction cross section, EDX and double differential cross section (DDX) of outgoing particles are calculated with the validated nuclear models. The calculated data obtained with the TALYS code are compared with the experimental data from the EXFOR and evaluated nuclear data from data libraries e.g. the evaluated nuclear data files-VIII (ENDF-VIII) and TALYS evaluated nuclear data libraries-17/15 (TENDL-17). The discrepancies in the nuclear data from ENDF and TENDL data library with the experimental data from EXFOR are identified and discussed. The calculated cross section data are in better agreement with the experimental data compared to the data from ENDF and TENDL.
2. The study of transmutation in iron, tungsten and chromium for typical fusion reactor neutron spectrum are carried out with the validated nuclear models and parameters. Transmutated isotopes including the radioactive one in stable isotopes of iron, tungsten and chromium and their time evolution have been reported for the first time as per the explored literature survey. Helium and

hydrogen production cross section of iron, chromium and tungsten are calculated for neutron irradiation of up to 15 MeV energy. Hydrogen production in chromium and tungsten for the fusion neutron spectrum are reported for the first time.

3. Molecular dynamics simulations of damage cascades initiated by a self recoil atom have been carried out at up to 200 KeV damage energies in iron, tungsten and chromium. The energy loss of PKA in electronic excitation is included in the MD simulation of displacement damage in iron for the first time. The MD simulations of pure chromium are carried out for the first time. The results of the MD simulations have been used to derive the constant parameters of the Arc-dpa method.
4. Based on the nuclear data calculated with the TALYS code and damage matrices obtained with the Arc-dpa method, MD simulations, and NRT method, displacement damage cross section of iron, tungsten, and chromium are calculated. This calculated displacement damage cross section is further used to predict the values of dpa/FPY at different neutron environments of ITER and European demo fusion reactor.
5. A Monte Carlo method to reconstruct the true energy spectrum of charged particles is developed and reported in this thesis. This method is based on the transport of charged particles and includes multiple scattering in its approach. This method has been demonstrated and validated with the GEANT-4.1.

1.9 Organization of thesis

This thesis is organized as follows; Chapter 1 gives the introduction to the nuclear fusion and important nuclear responses that need to be evaluated to predict the lifetime

of reactor components. Chapter 2 gives an overview of existing scientific literature on gas production, transmutation, and displacement damage in iron, tungsten and chromium. Limitations of the existed work have been detailed in this chapter. Chapter 3 contains the introduction of different nuclear models, level density models. In this chapter, the optimization approach to select and validate the nuclear model are explained for $^{56}Fe(n,n')^{56}Fe$ reaction channel at 14.1 MeV neutron energy. Chapter 4 contains the calculation of reaction cross section and energy differential cross section data of outgoing particles from open reaction channels in stable isotopes of iron, chromium and tungsten. These cross section data are calculated to select and validate the nuclear model for iron, tungsten and chromium. The energy spectra of recoils from all the stable isotopes of iron, tungsten and chromium are calculated and presented in this chapter. Chapter 5 contains the results of helium production, hydrogen production and transmutation in iron, tungsten, and chromium for typical D-T neutron spectra. Chapter 6 contains the results of the MD simulation of damage cascade in iron, tungsten and chromium. The Arc-dpa parameters are calibrated with the results of the MD simulation. The calculation of displacement damage cross section and prediction of dpa in iron, chromium and tungsten are reported in this chapter. In chapter 7, a Monte-Carlo method based on the transport of charged particles to reconstruct the true energy spectrum of charged particles has been demonstrated and explained. Chapter 8 contains the summary and conclusion of this thesis.

CHAPTER: 2 LITERATURE SURVEY: OVERVIEW OF EXISTING WORK AND METHODS

2.1 introduction

The transmutation, gas production and displacement damage have been introduced in the previous chapter. The estimation of gas production requires the nuclear reaction cross section data of (n,p), (n,np), (n,α), (n,nα) reaction channels and the estimation of transmutation requires the cross section data of all the open reaction channels of parent and daughter element. The cross section data of these reaction channels can be experimentally measured and can also be calculated with the nuclear codes such as the TALYS-1.8 [32], Empire [33] and GNASH [34]. To study the displacement damage in fusion reactor materials, the displacement damage cross section (σ_{dpa}) are predicted for a given neutron spectrum and is calculated with Equation 2.1 as;

$$\sigma_{dpa}(E_n)_i = \int_{Ed}^{Tmax} \left(\frac{d\sigma}{dE}\right)_i \upsilon(T)_i \, dT \qquad (2.1)$$

where E_d is the threshold energy of displacement damage, T_{max} is the maximum energy available to the recoil nucleus, $\frac{d\sigma}{dE}$ is the Rutherford scattering cross section of a projectile (neutron) to transfer a fraction of its energy to the recoil, υ(T) is the number of Frenkel pairs created due to the energetic recoil, T is the damage energy of the recoil and E_n is the energy of incident neutrons. In the case of neutron irradiation, $\frac{d\sigma}{dE}$ is the energy spectra or EDX of recoil nucleus. It is noted from the eq. 2.1 that the essential input parameters to calculate the σ_{dpa} are the energy spectra of recoils and number of Frenkel pairs created due to the dynamics of recoil atoms in the reactor material. The energy spectra of recoil species cannot be measured with the experiments due to their

high mass and very low range in the target foils. This energy spectra of recoils can be deduced from the EDX of their respective outgoing particles such as neutrons, protons and alpha particles. The experimental measurement of EDX of outgoing particles also plays an important role to study the different modes of nuclear reactions e.g. direct, pre-equilibrium and compound nuclear reaction mechanism [35]. The theoretical and experimental approaches to obtain the reaction cross section data are explained in the next sections.

2.2 Nuclear cross section through experiments and nuclear reaction codes

The nuclear reaction cross section is the probability of occurring a particular nuclear reaction. This nuclear reaction cross section provides information about the number of reactions that could take place for a given neutron flux. The DDX of outgoing particles provides the information of energy distribution of outgoing particles at a particular angle or vice versa. The EDX of outgoing particles is the angle integrated double differential cross section and provides the information of the energy spectrum of outgoing particles. These reaction cross section data can be measured experimentally and also can be calculated using the nuclear reaction codes such as TALYS-1.8 and EMPIRE-3.2. The prediction of cross section data using the experimental technique and theoretical calculations are introduced in the next section.

2.2.1 Nuclear cross section estimation using experimentation technique

The neutron activation and online spectroscopy of outgoing particles are the two experimental methods with which reaction cross sections are measured. In the neutron activation technique, a target is irradiated with the neutrons and later induced gamma photons are recorded using the high purity germanium or any other gamma detector.

Different reaction channels produce different reaction products which have specific gamma characteristics. By identifying the energy and intensity of gamma photons, the cross section is deduced. This activation method can only be used when a reaction product is radioactive and emit gamma photons after neutron irradiations. Another method to measure the reaction cross section is the online spectroscopy of charged particles. In the online spectroscopy of charged particles, the energy spectra of charged particles are measured using the silicon-based detectors during the neutron irradiation. Online spectroscopy of charged particles has the following limitations;

1) Background noise suppression needs to be carried out as charged particles are also produced from the scattering chamber or other auxiliary systems of experimental setup during neutron irradiation.

2) For the high energy neutron irradiation, different species of charged particles are produced simultaneously and is required to be identified.

3) Charged particles produced in the target foil lose a fraction of their energy in the target foil itself while coming out from it and sometimes get absorbed in it. Due to this, energy spectra of charged particles obtained with silicon-based detectors are degraded in the energy and number of particles. This loss of energy and particles depends on the thickness of the target foil. Preparing very thin self-supporting target foil of non-malleable materials e.g. chromium and tungsten is a complicated process thus refrain to have the online spectroscopy of charged particles in these materials. There are methods with which true energy spectrum of charged particles can be reconstructed and are explained later in this chapter and chapter 7. Experimental measurement of EDX of

outgoing particles and reaction cross section for D-T neutron irradiation has some known limitations and given below;

1) Unavailability of experimentation facilities that can produce the monoenergetic neutron beam covering all the D-T neutron spectra [36]. Available neutron facilities are mostly of 14.1 MeV, 14.8 MeV neutrons which are based on the D-T beam fusion and 2.5 MeV neutrons which are based on the D-D beam fusion [37]. Intense monoenergetic neutron beams of intermediate neutron energies are not available at the laboratories.

2) The low intensity of neutron flux available in the D-T and D-D neutron facilities compared to the neutron flux available in ITER and proposed DEMO reactors.

3) Fabrication issues of very thin foils of some non-malleable materials such as chromium and tungsten that cause hindrance in experiments to measure the EDX of outgoing charged particles.

Despite these experimentation limitations, several researchers have recorded the energy differential cross section of outgoing neutron and charged particles for fusion applications [35], [38]–[40] [39]. The study of the transmutation, gas production and displacement damage require the nuclear data of reaction cross section of all open reaction channels and energy differential cross section of recoils at up to 14.1 MeV neutron energies. The experimental data is quite insufficient for these studies due to the scarcity of data for full D-T neutron spectrum. Due to these reasons, the nuclear cross sections data are estimated using the nuclear reaction codes and their details are given in the next section.

2.2.2 Nuclear cross section estimation using theoretical codes

The nuclear reactions codes e.g. TALYS-1.8 [18], EMPIRE3.2 [33] were developed to predict the nuclear cross section data. These codes use different nuclear models and parameters to calculate the reaction cross section and the differential cross section of outgoing particles. Different nuclear data libraries such as the ENDF [41], TENDL [42], and fusion evaluated nuclear data libraries (FENDL) [43] that consists of the nuclear data for fusion reactor related elements were produced. Some of the cross-section calculations from these nuclear data libraries are validated with the existing nuclear data from the EXFOR data library [44]. These data libraries provide nuclear data in the form of ENDF-VI format that can be processed with the NJOY code [45] to predict the displacement damage. Similarly, European activation file (EAF) [46] was also developed and consists of all the nuclear data required to calculate activation, transmutation and gas production. The reliability and accuracy of their data and their existing literature have been reviewed in the upcoming sections.

2.3 Overview of existing nuclear data for fusion applications

Due to experimental limitations, experimental data is not abundant for the D-T neutron spectrum. Grimes et al [47] had carried out the double differential cross section (DDX) studies on chromium, nickel, copper and iron to understand the different reaction modes for the neutron irradiation of 14.8 MeV energy. Kondo et al [38] had designed a facility to measure the DDX of charged particles from florine, beryllium, carbon and aluminium at 14.1 MeV neutron irradiation. Kokoo et al [40] had measured the DDX cross section data of outgoing charged particles from cobalt, vanadium, iron, chromium, niobium and molybdenum for DT neutron irradiation. Lalremuerata et al [39] had measured the DDX of outgoing alpha particles from nickel and aluminium for 14.8 MeV neutron

irradiation. These DDX data of outgoing charged particles play a vital role in validating nuclear data for fusion applications. The nuclear data in the form of reaction cross section of open reaction channels, DDX, and EDX of outgoing particles, EDX data of recoil, decay, and half-life data of radioactive isotopes are essential data to predict the nuclear responses. These nuclear data are not only required to predict the nuclear responses e.g. transmutation, gas production and displacement damage but are also essential in the transport calculation and radiation waste classification [48]. Gas production and transmutation require the reaction cross section data of all reaction channels, displacement damage requires EDX data of recoils, and transport calculations and radioactive waste classification require the neutron induced reaction cross section of all the open reaction channels. The nuclear data also plays an important role in fission based nuclear reactors such as PHWR and BWR, etc. In fission-based reactors, neutrons of up to 2.5 MeV energies are mostly produced during the operation and most of them remain available to fuel assembly due to the use of moderator. Hence most of their interactions take place in the reactor core. Major reaction channels that are open for these energy neutrons are nuclear fission and radiative capture in the actinides. Other reaction channels e.g. (n,p), (n,α) and (n,2n) do not contribute much to radiation damage or other nuclear responses due to their high reaction threshold. Due to these reasons, gas production and transmutation are not very dominant in the fission-based reactors. In case of a fusion reactor, neutron of 14.1 MeV energies are produced in the D-T fusion and interact with the alloying elements of plasma-facing component, blankets, shield modules before being absorbed in the reactor environment. Due to the high energy and intensity, neutrons during their lifetime transport from plasma chamber to shield module and produce gases, additional neutrons, and cause transmutation and displacement

damage in many materials including mid-range structural elements such as Fe, Cr, etc,. to high Z materials e.g. tungsten [48]. This broad importance and requirement of evaluated nuclear data led to the beginning of FENDL-1 [49]. The creation of FENDL-1 was based on the most reliable data of that time from other core data libraries e.g. ENDF (evaluated nuclear data library), JEFF (joint European fusion files), and JENDL (Japanese evaluated nuclear data library). The benchmarking of FENDL-1 [49] was carried out in 1997-98 and led to the creation of FENDL-2 and FENDL-2.1 [43]. The recent version of FENDL-3 was released and benchmarked in 2014 [50]. Other nuclear data libraries such as ENDF-VIII [41], TENDL-17 [18] also contain nuclear data not only for fusion neutrons but also for other applications such as accelerated driven subcritical system and medical applications. These nuclear data libraries contain double differential cross section of outgoing particles from all respective reaction channels and are written in ENDF-VI format [51]. The FENDL-3 data library contains nuclear data of neutron, protons and deuteron induced reactions for up to 150 MeV for transport and general-purpose applications and at up to 60 MeV neutron irradiation for activation applications [50]. The FENDL-3 data library was produced from the nuclear data from TENDL-11 [42] (TALYS evaluated nuclear data library). The TENDL-11 had been produced using the TALYS-1.2 code [32] with its default and modified nuclear parameters. The latest, ENDF-VIII data library is produced with the EMPIRE nuclear reaction code [33]. These nuclear data libraries consist of reaction cross section data, double differential cross section of different outgoing particles such as protons, alpha particles, gamma photons, scattered neutrons and additionally produced neutrons and resonance data for nuclear structure. These nuclear data libraries do not possess the energy spectrum or the energy differential cross section of recoils species. The nuclear

data processing codes e.g. NJOY [45], Spectra-PKA [52] and Spectre [53] use the DDX of outgoing particles to produce the EDX of respective recoil species. These codes neither calculate any cross-section data by themselves nor check their accuracy. Any uncertainty in the DDX data would result in the inaccurate estimation of EDX of recoils. The uncertainties in the differential cross section data from ENDF-VIII, and TENDL-17 have been observed with the experimental data and discussed in the 3rd and 4th chapter of this thesis. As the importance of accurate nuclear data in the estimation of transmutation, dpa and GPA has been summarised earlier in previous and this chapter, all the cross-section data presented in this thesis (reaction cross section data, EDX, and DDX data of all the open reaction channels) are calculated with the appropriate nuclear models with the TALYS-1.8 code. Nuclear models and parameters have been validated with the experimental data from the EXFOR data library and are discussed in Chapter 3 & 4.

2.5 Overview of studies of gas production and transmutation in fusion reactor materials

The transmutation in the fusion reactor materials designates the change in the elemental composition of fusion reactor materials. The changes in the isotopic and elemental composition alter the microstructure and engineering properties of structural alloys thus affect their intended functionality in the fusion reactors. The transmutation of reactor materials is needed to be evaluated to estimate the following;

1. Conversion of an atomic species to other following charged particle production reaction channels and the radioactive decay of reaction products
2. Production of long-lived radioisotopes to monitor the effective radioactive waste management

3. Gamma dose and nuclear heating

Fusion reactor materials such as iron, chromium and tungsten are converted into other elements via direct absorption reaction channels such as (n,xp), (n,xα) and (n,xd) as well as via radioactive decay of radioisotopes produced from radioactive capture and (n,2n) reaction channels. This transmutation of materials in the neutron environment is solved with the Bateman equation [54]. It is a first-order differential equation. The transmutation studies can be carried out with the ACTYS [55] and FISPACT [56] codes. Both of these codes solve the Bateman equation using the nuclear data from EAF-7 [46] (European activation file). The EAF-7 contains the nuclear data of excitation functions of 816 target isotopes ranging from ^{1}H to ^{257}Fm. The nuclear data in EAF-7 was extracted from multiple data libraries such as JENDL, ENDF and TENDL. The accuracy of reaction cross section data from EAF-7 is checked with the experimental data and discussed in Chapter 4. Some reactions in iron, chromium and tungsten shows discrepancies with the existing experimental nuclear data and reported in the Chapter 3 and 4. To overcome the limitations of nuclear data, reaction cross section data of major charged particles production reactions e.g. (n,p), (n,np), (n,α), and (n,nα) are calculated using the appropriate nuclear models with the TALYS-1.8 code and discussed in the chapter 3 and 4.

Gilbert et al [10] [12] [57] [9] [58], Noda et al. [19] and Forty et al. [59] had studied the transmutation and gas production in fusion reactor materials. Some important outcomes from existing literature on transmutation are given below:

1. Gilbert et al [22] studied the transmutation in tungsten, tantalum, and titanium alloys irradiated with the neutron spectrum of EU demo reactor. Gilbert et al

[22] also checked the dynamics of various transmutated elements in tungsten with respect to full power year (FPY). Gilbert et al used the EAF data library for cross section of different excitation functions and reported the compositional changes of the natural elements during the 5 full power year reactor operation of EU demo. The changes in the isotopic composition with respect to FPY had not been reported by Gilbert et al [22]. Some of the transmutated isotopes are radioactive and play an important role in decommissioning and waste management after operations.

2. Gilbert et al [12] [57] [9] reported the values of dpa(NRT), helium and hydrogen production in fusion reactor material for the D-T neutron irradiation of EU Demo fusion reactor using the TENDL-2011/17 data library and FISHPACT activation code.
3. Gilbert et al [58] had reported the transmutation of natural elements ranging from hydrogen to bismuth for the neutron irradiation at the first wall of EU demo fusion reactor using the EAF data library.

All these existing transmutation studies on fusion reactor materials were carried out for natural elements. All of these above-mentioned transmutation and gas production studies were performed using the EAF-2003/2007 data library which requires up-gradation of its data due to recent advancement in experimental nuclear cross section measurements. In the present thesis, the nuclear cross section of all the open reaction channels in stable isotopes of iron, tungsten and chromium have been calculated with the TALYS-1.8 code and later used in the transmutation calculation with this data of iron, tungsten and chromium along with the remaining data of reaction by-products from EAF-07. In the present thesis, transmutation studies are carried out in iron,

tungsten and chromium for the D-T neutron spectra of EU DEMO fusion reactor and change in the isotopic composition of transmutated elements from all the stable isotopes of iron, tungsten and chromium are reported. The radioactive transmutated isotopes that are produced during the burnup are also studied and reported. Helium production in iron, tungsten, and chromium and hydrogen production in iron were studied by Gilbert et al [12], [57]. Hydrogen production in tungsten and chromium was not reported in the previous studies of gas production. In this thesis, helium and hydrogen production in iron, tungsten and chromium are reported for the D-T neutron spectra of fusion reactors using the calculated nuclear data obtained with the TALYS-1.8 code.

2.8 Overview of damage studies in fusion materials

The energetic particles having energies more than the threshold displacement damage energy are produced in many accelerator devices, commercial fission and fusion-based reactor. These energetic particles create damage cascade and end up creating interstitials and vacancies. Several analytical and simulation methods have been introduced by researchers to quantify the number of Frenkel pairs and are given below;

1. Kinchin-Pease and NRT models
2. Binary collisional approximation method
3. Molecular dynamics simulations
4. Kinetic Monte Carlo method
5. Arc-dpa method

Kinchin-Pease method [60] was the very first method to calculate the number of displacements. In this model, the number of displacements is calculated, based on the transfer of kinetic energy of the recoil to the target atoms above threshold energy to

cause single displacement. As per the original K-P model, the number of displacement is calculated by dividing the kinetic energy of recoil ion with the twice of threshold energy [60]. Later it was observed that the kinetic energy of recoil is transferred to the electrons, causing electronic excitation and to the atoms, causing displacement damage. Thus, in the modified K-P model kinetic energy of recoil is replaced with the damage energy. The damage energy is the kinetic energy of PKA minus the energy lost in electronic excitations. This approach is used in SRIM code [61] in its quick damage calculations for ion irradiation. Later, Norgett, Robinson and Torren (NRT) added the factor of 0.8 in modified K-P method to predict the displacements in materials and proposed the NRT method of damage evaluation [23]. This factor of 0.8 was added based on computer-based binary collision simulations. The NRT method allows quantitative assessment of displacement damage and also facilitate comparison of produced damage in two materials. Due to widespread application of displacement damage in many communities such as nuclear fission, ion accelerators, and nuclear fusion, etc, and its rapid estimation of displacement damage, NRT model became an international standard to quantify the displacement damage. NRT method was extensively used in the damage studies for different structural materials [17], [62]–[64][65]. Most of these studies were carried out using nuclear data from evaluated nuclear data libraries such as ENDF, TENDL, etc. This approach had also been adopted by ASTM to predict the displacement damage of structural materials at up to 20 MeV neutron irradiation [66] using the nuclear data from ENDF-IV. However, despite its widespread use, the NRT method has some well-known limitation such as;

1. It does not include many body interactions in its approach

2. It does not include the interaction of interstitials and vacancies that results in annihilation and recombination of defects
3. At low recoil energy near to threshold damage energy, defect production increases more gradually than the step function of the NRT model

Due to these limitations, it predicts the overestimated values of actual defects. Binary collision approximation model (BCA) can also be used to predict the number of displacements. The BCA based codes such as SRIM [61] and Dart [24] do not incorporate the many-body interactions and interactions of interstitials and vacancies with each other in their approach, thus their usage is also limited. The molecular dynamics simulations (MD simulations) [26] [68] [69] [70] can also be used to predict the number of displacements produced due to the energetic recoils in the target. The MD simulations are the computational approach to model atomic systems at successive time steps. The MD simulations can simulate the damage cascade very accurately within the limits of the Born-Oppenheimer approximations if carried out using the accurate repulsive penitential and adaptive time step. In the MD simulations, forces on atoms are calculated using the Newton's equation at every time step until the desired time step is achieved. To study the displacement cascade with the MD simulations, a specified atom known as a recoil or PKA is provided the desired energy and direction. This recoil atom later interact with other atoms of the target. During its interaction with the atoms of target, recoils transfers fraction of its energy to surrounding atoms and forms damage cascade. The energy and location of all the interacting atoms along with the location of recoil are recorded at different time steps until the saturated defects are formed. The accuracy of the MD simulation depends on the accuracy of interatomic potentials and time steps [67]. The MD simulations have limitations of time scale and

sample size. Despite the wide potentials of MD simulation in radiation damage studies, it is often not used to predict the cumulative displacement damage for neutron irradiation. Fikar et al [26], Warrier et al [68] [69], Stoller et al [70] had performed the MD simulation of displacement damage in natural iron and tungsten for fusion applications. Warrier et al had carried out the MD simulation of self recoil in tungsten at up to 5 keV damage energies and Fikar et al [26] had carried out the similar simulation at up to 50 keV damage energies in tungsten. Stoller et al [70] had carried out the MD simulation of self recoil in iron at up to 50 keV recoil energies. Stoller et al had not included of loss of energy of PKA in electronic excitation, thus overestimates the value of displacement defects. The MD simulations of displacement damage of self recoil in pure chromium have not been reported in the literature. It has been noted that due to the high energies of the neutrons in the D-T neutron spectrum of a typical fusion reactor, recoil or PKA of up to 300 keV energies are produced. The MD simulations require huge computation time and interatomic potentials of interactions between PKA species and target atoms. Due to these requirements, it is often not considered in materials optimization for fusion applications. Charged particles production reaction channels where recoil atoms are of different species than parent target, MD simulation requires the interatomic potential for those recoil species and target atoms which is time consuming and requires substantial efforts. To tackle this limitation of MD simulations, Nordlund et al [25] proposed the athermal recombination corrected-dpa (arc-dpa) model. Nordlund et al modified the NRT formulation and include an additional term, known as the defect production efficiency term. This defect production efficiency term accounts many body interactions, recombination and annihilation of interstitials and vacancies. Defect production efficiency term consists of two constant parameters (arc-

dpa parameters) that is fitted with the results of the MD simulation results. In the present thesis, the constant parameters of arc-dpa method have been calibrated with the results of MD simulations of iron, tungsten and chromium. The Arc-dpa predictions have been compared with the MD simulations and NRT model in this thesis and discussed in Chapter 6.

In the past, most of the predictions of dpa had been carried out with the NRT approach. Recently, Konobeyev et al. had developed a data library of displacement damage cross section using the NRT and arc-dpa method [71]. The constants parameters of the Arc-dpa method were adopted from Konobeyev et al. [72]. Konobeyev et al. used MD simulations results of Stoller et al and Nordlund et al. for iron and tungsten to derive the constant parameters of arc-dpa approach. The empirical parameters for chromium were selected based on other materials as no MD simulations results were available for pure chromium. Stoller et al did not include energy loss of PKA in electronic excitation thus overestimated the numbers of Frenkel pairs. In the present work, the energy loss of PKA in electronic excitation is included in the damage cascade using the LSS potentials and two temperature model and MD simulations of damage cascade in pure chromium are carried for the first time.

The prediction of dpa at different locations of the EU DEMO fusion reactor was carried out by Gilbert et al [14], [52] using the NRT method. In this thesis, the prediction of dpa has been carried out with the NRT, MD simulations and arc-dpa method. These results have been discussed in Chapter 6.

2.9 Overview of methods to reconstruct the true energy spectrum of charged particles

The energy and double differential cross section of outgoing charged particles and neutrons are essential data to validate the nuclear models and parameters for the evaluation of nuclear data for displacement damage. Neutron-induced charged particles lose a fraction of their energy and sometimes are absorbed in the target foil. Due to this loss of energy and particles, measured energy spectrum is degraded in the energy and loss of particles. This measured energy spectrum needs to be corrected to have the true energy spectrum of charged particles. Previously, this problem of loss of energy and particles were solved using the Fredholm equation [73]. Johnson et al [74], Slypen et al [29], Pomp et al [30] and Rezentes et al [28] developed methods to reconstruct the true energy spectrum based on single incident energy of charged particles. They did not consider successive interactions of charged particles with the atoms of target foil. The charged particles after each interaction with the atom of target lose a fraction of their energy, thus their stopping power is also changed for the next interaction. Soderberg et al [27] had considered the multiple scattering in its approach while solving the Fredholm equation. Only Slypen et al had considered the detector threshold energy in the reconstruction of the true spectrum. In this thesis, A Monte Carlo code based on the transport of charged particles has been developed and demonstrated. The multiple scattering of charged particles has been included in its approach. During reconstruction of true energy spectrum of charged particles, detector threshold energy is taken into consideration to decrease the noise at lower energies in the energy spectrum. The proposed method and other existing methods based on the Fredholm equation are compared and discussed in Chapter 7.

2.10 Summary and major improvements from this thesis

In this thesis, the nuclear responses (transmutation, gas production, and displacement damage) in iron, tungsten and chromium have been evaluated for the D-T neutron spectrum of typical fusion reactors. The transmutation studies have been carried out with the ACTYS code using the nuclear data obtained with the TALYS-1.8 code and EAF-7 data library. Gas production cross section has been calculated with the appropriate nuclear models and later used to predict the amount of helium and hydrogen production in iron, chromium and tungsten. Displacement damage cross section has been calculated with the NRT and MD simulation. The constant parameters of the Arc-dpa method are calibrated with the MD simulation results. The dpa values in iron, tungsten and chromium are calculated for the D-T neutron spectrum. Major improvements which this thesis provides to the fusion community are:

1. Transmutation studies have been carried out for all the stable isotopes of iron, tungsten and chromium. The time evolution of the isotopic composition of all the major transmutated isotopes including the radioactive ones is reported and discussed for the first time.
2. Gas production in iron, chromium and tungsten have been predicted with the validated nuclear models and parameters. Hydrogen production in tungsten and chromium are reported for the first time for fusion reactor neutron spectrum.
3. Molecular dynamics simulation of self recoil in iron and tungsten have been carried out at up to 200 keV damage energies. The energy loss of PKA in electronic excitation have been included in damage cascade and reported first time for iron. Similar MD simulations have been carried out for pure chromium and reported for the first time in literature.

4. The constant parameters of the Arc-dpa approach have been calibrated using the MD simulation results and later used to calculate the displacement damage cross section of iron, chromium and tungsten. These displacement damage cross section data have been used to predict the values of dpa in iron, chromium and tungsten for the typical D-T neutron spectra of a fusion reactor.
5. A Monte Carlo code, based on the transport of charged particles have been developed to reconstruct the true energy spectrum of charged particles.

CHAPTER: 3 NUCLEAR CROSS-SECTION DATA: INTRODUCTION AND OPTIMIZATION OF NUCLEAR MODELS

3.1 Introduction

ITER machine and EU DEMO fusion reactor will be the first of their kind devices that will check the limitations of the materials and their functionality in the intense field of high energy neutrons. As introduced in the chapter-1, 2, these high energy neutron flux cause transmutation, gas production and displacement damage in fusion reactor materials. In the fusion reactors, Iron, tungsten and chromium are used at multiple locations. Iron as the major constituents of SS will be used at the first wall, thermal shield, vacuum vessel, ports, blanket and divertor location in the fusion reactors [75]. Tungsten will be used at the divertor location due to its high melting temperature, higher sputtering threshold energy and mechanical stability [75]. Chromium will be used at the first wall, blanket, and divertor as Cu-Cr-Zr alloy and also at other places as one of the constituents of the SS [75]. These materials interact with neutrons via different reaction channels. Due to high energies of incident neutrons, the multiple reaction modes such as compound nuclear formation, pre-equilibrium and direct nuclear reaction contribute to the total reaction. These nuclear reaction mechanisms are explained in the next sections.

3.1.1 Compound nuclear reaction mechanism

At low projectile energies, incident projectile (neutron) enters into the nucleus of mass A and shares its energy among all the nucleons. The kinetic energy of this extra neutron plus binding energy of the newly bound neutron is the excitation energy of the newly

formed nucleus of (A+1) mass. This excited nucleus is very unstable and can decay via many probable reaction channels. This excited nucleus can decay via emitting neutron of low energy, light charged particle, gamma photons and nuclear fission. This de-excitation process takes time of the order of 10^{-16} to 10^{-18} seconds and during this time an intermediated stage is formed and known as the compound nuclear formation. Compound nucleus formation is represented as;

$$A+n \rightarrow C^* \rightarrow B+b \tag{3.1}$$

Here, C* is the compound nucleus and it decays into an outgoing particle b and a recoil nucleus B. It takes some time to form compound nucleus after interaction of neutron with target A and energy of incident neutron are shared among all the nucleons. Due to these, it lost the memory of its entrance channels and outgoing channels depend on the excitation energy and composition of the compound nucleus. This independence hypothesis was verified by Ghosal et al. [76]. Experimentally, it has been observed that the angular distribution of outgoing particle remains isotropic in the compound nuclear reaction mechanism. The compound nuclear mechanism is described with the two models namely; Weisskopf-Ewing Theory and Hauser-Feshbach theory.

3.1.1.1 Weisskopf-Ewing Theory

The cross section for nuclear reaction (eq. 3.1) is given by

$$\sigma(n,b) = \sigma_{CN}(n)\ P(b) \tag{3.2}$$

where $\sigma_{CN}(n)$ is the cross section of compound nuclear formation and $P(b)$ is the probability of the compound nucleus to decay into B+b reaction channels. In the compound nuclear reaction mechanism, outgoing particles are emitted through the

statistical fluctuation among the nucleons of compound nuclear similar to the analogy of evaporation of liquid drops. Due to this analogy in the compound nuclear mechanism, outgoing particles approach the Maxwellian distribution. The cross section of reaction A(n,b)B as derived by the Weisskopf -Ewing theory is given by;

$$\sigma(n,b)= \sigma_{CN}(n)\frac{(2I_b+1)\,\mu_b\,\sigma_{CN}(b)\,\rho(E_b)\,dE_b}{\sum_a \int_0^{E_{max}(a)} (2I_a+1)\,\mu_a\,\sigma_{CN}(a)\,\rho(E_a)\,dE_a} \tag{3.3}$$

Symbols in Eq. 3.3 represent the following;

a & b = entrance and exit channel

I_a & I_b = spin of entry and exit channels

$\rho(E_a)$ & $\rho(E_b)$ = density of levels of entry and exit channels

According to Weisskopf -Ewing theory, the spectrum of outgoing particles follows the Maxwellian distribution. The conservation of angular momentum has not been explicitly considered in this theory due to which it could not provide the information of the angular distribution of outgoing particles. Thus, to predict the angular distribution of outgoing particles, Hauser Feshbach's theory was introduced and is explained in next section.

3.1.1.2 Hauser Feshbach theory

The conservation of angular momentum is included in this theory and cross section of A(n,b)B reaction at angle θ is given as;

$$\sigma(a,E_b,\theta) =\frac{\pi \lambda_a^2}{(2I+1)\,(2S_a+1)} \sum_{l,\,j,J,j',l'} A_j(l,j \mid l', j' \mid \theta \frac{T_l(E_a)T_{l'}(E_b)}{\sum_b \sum_{l'} T_l(E_b)} \tag{3.3}$$

The symbols in eq. 3.3 represent the followings;

I and I' = angular momentum of entry and exit channels

S_a = spin of projectile (neutron)

Π = parity of the system

T_l and $T_{l'}$ = transmission coefficient of entry and exit channels

At low projectile energies, there exist a correlation between the entrance and exit channel that enhances the elastic scattering reaction channel and decreases the contribution of other absorption reaction channels. This factor is accounted with width fluctuation correction factor (WFC) in the expression of Hauser Feshbach model (simplified) as

$$\sigma_{nb}=\frac{\Pi}{k_a^2}\frac{T_a T_b}{\sum_c T_c} W_{nb} \quad (3.4)$$

Here, W_{nb} is the WFC and can be calculated with the Hofmann-Richert-Tepel-Weidenmuller (HRTW), and Moldauer models. In the HRTW approach, elastic scattering channels is assumed to have the major effect of this correlation and W_{nb} is calculated as

$$W_{nb}=\frac{VnVb}{\sum_c Vc}(1+\Delta_{nb})(W_a-1)\frac{\sum_c Tc}{TnTb} \quad (3.5)$$

Here, V is the effective transmission coefficient, and W_a represents the elastic enhancement factor. Moldauer also proposed a method to quantify the WFC based on the assumption that partial width T can also be calculated with the Porter-Thomas distribution and χ^2 of υ degree of freedom is applied to them. Moldauer has derived the following formula to calculate the WFC [18] and given as;

$$W_{nb} = (1+ \delta_{nb}\frac{2}{\upsilon_a})\int_0^{\infty} dx \prod_c (1 + \frac{2T_c}{\upsilon_c \sum_i T_i}x)^{-\delta_{ac}-\delta_{bc}-\upsilon_c/2} \quad (3.6)$$

Another method with which WFC can be predicted is the GOE triple integral model [18]. The energy differential cross section of outgoing particles is calculated with the following formula based on the Hauser Feshbach model [18] as;

$$\frac{d\sigma}{dE} = \sum_{j\pi} \sigma^{CN}(E_n) \frac{\sum_{l\pi} \Gamma_b(U,J,\pi,E,I,\pi)\, \rho_b(E,I,\pi)}{\Gamma(U,J,\pi)} \quad (3.7)$$

Where $\sigma^{CN}(E_n)$ is the compound nucleus formation cross section for projectile (a) of E_a energy, Γ_b is the transmission coefficient for the emission of ejectile (b), $\rho_b(E,I,\pi)$ is the nuclear level density of the residual nuclei, (U,J,π) and (E,I,π) are the energy, angular momentum and parity of the compound and residual nuclei, respectively [18].

3.1.2 Direct nuclear reaction mechanism

If the energy of the incident neutron is high, its interaction time with nucleons becomes less which results in the interaction of incident neutron with limited numbers of nucleons only. These types of reaction proceed without forming an intermediate stage of compound nuclear formation, hence are called direct nuclear reaction mechanism. The direct nuclear reaction mechanism is different from the compound nuclear reaction mechanism due to the very low time period available (10^{-22} second) to transverse a neutron through the target nucleus. The compound nuclear reaction mechanism has this period of 10^{-14} to 10^{-20} sec. The direct nuclear reaction is of three types that could take place in the D-T neutron environment namely; inelastic scattering, stripping reactions, and knock-out reactions [77]. The direct nuclear reactions are single step processes and governed by the energy and momentum of the incident channel. The angular distributions of outgoing particles are mainly forward peaked and outgoing particles are

emitted with higher energy compared to the compound nuclear reaction mechanism. The differential cross section for direct nuclear reaction mechanism is calculated as;

$$\frac{d\sigma}{d\Omega} = \frac{m_n.m_b}{(2\pi.\hbar^2)^2}\frac{k_b}{k_n}\left|V_{fi}\right|^2 \quad (3.8)$$

Where m_α and m_β are the reduced mass of the incident and ejected particles, k_α and k_β are the wave number of incident and exit channel, and V_{fi} is the transition matrix element of the initial state (i) to the final state (f).

3.1.3 Pre-equilibrium reaction mechanism

Between the two extremes of fast direct nuclear reaction and comparatively slow compound nuclear reaction mechanism, there exists a third mode of nuclear reaction mode known as the pre-equilibrium or pre-compound nuclear reaction mechanism. The pre-equilibrium nuclear reaction mechanism represents an intermediate stage between direct and compound nuclear reaction mechanisms. As a projectile (neutron) interacts with the target nuclei and proceeds toward the statistic equilibrium for compound nucleus formation, the energy of the incident neutron is shared with the increasing number of nucleons. At the initial stage, the numbers of interacting nucleons are less and the energy available to them is large. Consequently, particles emitted at this stage will carry more energy than emitted from the equilibrated compound nucleus and represent the pre-equilibrium nuclear reaction mechanism. The pre-equilibrium emission of outgoing particles shows forward peaking in angular distribution as well as shows a substantial cross section at the backward angles. The pre-equilibrium nuclear reaction mechanism is explained with the exciton and multi-step direct compound nuclear reaction model. These models are briefly introduced in the next section.

3.1.3.1 Exciton model

In this model, the degree of freedoms or the number of excited holes and particles are referred to as the excitons. This model is based on the assumption that projectile such as neutron interacts with nucleons of the target nucleus and forms excited configuration of excitons through two-body collisions. The energy of the projectile is shared among a greater number of nucleons which gives rise to the number of excitons and system tend to proceed towards equilibrium. During this transition of different exciton states, any particle can be emitted if its energy is greater than its separation energy. The pre-equilibrium component of the energy differential cross section of outgoing particles are calculated using the exciton method of Kalbach [78] and is given below:

$$\frac{d\sigma}{dE} = \sigma^{CF} \sum_{p_\pi=p_\pi^0}^{p_\pi^{eq}} \sum_{p_n=p_n^0}^{p_n^{eq}} \omega_k (p_\pi, h_\pi, p_n, h_n, E_k)\, S_{pre} (p_\pi, h_\pi, p_n, h_n, E_k) \quad (3.9)$$

Where p_π is the proton particle number, p_n is the neutron particle number, h_π is the proton hole number and h_n is the neutron hole number. In the present calculations, $p_n^{eq} = p_\Pi^{eq} =$ 6 has been considered as the upper limit of summation. Up to $p_n^{eq} = p_\Pi^{eq} = 6$, EDX is calculated with Eq. 3.9 and the rest of the spectra are calculated using the Hauser Feshbach method (eq. 3.4). ω_k is the emission rate of ejectiles, σ^{CF} is the compound nuclear cross section and S_{pre} is the strength function which characterizes the time period of the exciton configuration. ω_k is calculated with the Cline and Blann approach and given by the formula [32];

$$\omega_k(p_\pi, h_\pi, p_n, h_n, E_k) = \frac{2s_k + 1}{\Pi^2\hbar^3}\mu_k E_k \sigma_{k.inv} (E_k) \frac{\omega(p_\pi\text{-}Z_k,\ h_\pi,\ p_n\text{-}N_k,\ h_n,\ E_x)}{\omega(p_\pi, h_\pi, p_n, h_n, E^{tot})} \quad (3.10)$$

where $\sigma_{k.inv}$ is the inverse reaction cross section calculated with the optical model, ω is the two-component particle-hole state density.

3.1.3.2 Multi step compound model

Feshbach, Kerman and Koonin proposed a quantum mechanical theory to describe the pre-equilibrium emission by breaking the preequilibrium emission into multi step direct and multi-step compound emission [79]. During the initial stage when the system shifts towards the equilibrium of the compound nuclear mechanism, the number of particles that have been excited are less in the cascade of two body interactions. Thus, the particles have the excitation energies more than that of the being unbound particles. Due to which, some of the particles get emitted with the finite probability. These emissions are termed as the multi step direct (MSD) emissions. When a greater number of nucleons share the energy of the projectile, excitation energy per particles becomes less than that of the unbound particle. At this stage, particles can jump to continuum due to statistical fluctuations and leads to the emission of particles. This type of emission occurs when a system has not yet reached to equilibrium stage and known as the multi-step compound emission. The formula with which multi-step contribution is calculated, are given below:

$$\frac{d\sigma}{dE}=\sigma_{abs}\sum_{P=P_0}^{P_{avg}} S_u(p,h)T_u(p,h)\lambda_c^u\,(p,h,\varepsilon) \qquad (3.11)$$

Where P and P_{avg} represent the number of excited particles in a compound nucleus, T_u(p,h) is the lifetime of the n^{th} exciton state, $S_u(p,h)$ represents the probability of finding the excited nucleus in (p,h) state and $\lambda_c^u(p,h,\varepsilon)$ represents the emission rate with the energy ε.

3.1.4 Level density parameters

The compound nuclear reaction mode strongly depends on the nuclear level density. Nuclear level density is the degree of freedom of nucleons to be placed in a particle

orbit with the excitation energy lying between E and E+dE. Nuclear level densities are widely spread at low excitation energies and closely spaced at the higher excitation energies. The production rate of the outgoing particles in a compound nuclear reaction mechanism is proportional to the level density of the residual nucleus of excitation energy in between E and E+dE. Different approaches have been adopted to formalize the level density and are briefly detailed in the following section.

3.1.4.1 Fermi gas model and Fermi back shifted model

Fermi gas model, one of the best-known level density models is based on the assumption that single-particle states are uniformly distributed and collective levels don't exist. Fermi gas density for two fermion systems is calculated as;

$$W_{ab}^{tot} = \frac{\sqrt{\pi}\exp(2\sqrt{aU})}{12\,U^{5/4}a^{1/4}} \tag{3.12}$$

$$U = E_{ex} - \Delta \tag{3.13}$$

Here, Δ is the energy shift and is related to the pairing energy of nucleons to include the even-odd effect in nuclei, a is level density parameter ($a = \frac{\pi^2}{6}v_f$) and v_f is the single-particle density at Fermi surface. Fermi gas level density is derived assuming the total angular momentum to be randomly coupled and given as;

$$\rho_f^{tot} = \frac{\sqrt{\pi}\exp(2\sqrt{aU})}{2\sqrt{\pi\sigma}\,12\,U^{5/4}a^{1/4}} \tag{3.14}$$

Here σ is the square root of cut off spin parameter. σ^2 represents the total width of the angular momentum distribution of level densities.

The Fermi back shifted model (BFM) is a modified version of the Fermi gas model. In the BFM model, the pairing energy is an adjustable entity and level densities are calculated up to the lowest possible energy. In BFM model, U (effective excitation energy) is calculated as

$$U=E_x-\Delta^{BFM} \tag{3.15}$$

$$\Delta^{BFM}=\chi\frac{12}{\sqrt{A}}+\delta \tag{3.16}$$

where Δ^{BFM} is the energy shift, χ is -1 (for odd-odd nuclei), 0 (for odd-even nuclei) and 1 (for even-even nuclei) and δ is an adjustable parameter which is fitted with the experimental data of nuclear structures. Original BFM model was modified by Grossjean et al. [80] and Demetriou et al. [81] to fix the divergence problem in the expression of level density at U =0 and derived the expression for total level density as

$$\rho_{BFM}^{tot}(Ex)=\left(\frac{1}{\rho_F^{tot}(Ex)}+\frac{1}{\rho_0(t)}\right)^{-1} \tag{3.17}$$

Here, $\rho_0(t)$ is calculated as

$$\rho_0(t)=\frac{\exp(1)}{24\sigma}\frac{(a_n+a_p)^2}{\sqrt{a_n a_p}}\exp(4a_n a_p t^2) \tag{3.18}$$

Here a_n and a_p is equal to a/2 and t is equal to $\sqrt{U/a}$.

3.1.4.2 Constant temperature model

A. Gilbert and Cameron introduced the constant temperature model (CTM) for level density parameters. In this model, A. Gilbert et al. [82] divided excitation energy into two regions. The first one is the low energy region from 0 MeV to the matching energy (EM) and constant temperature law is applied in this energy region. The other is the

high energy region above the matching energy where fermi gas model is applied. The nuclear level density as per the CTM model is given as;

$\rho^{tot}(Ex) = \rho_T^{tot}(E_x)$, If $E_x \leq E_M$

$= \rho_{FGM}^{tot}(E_x)$, If $E_M \leq E_X$ (3.19)

$\rho_T^{tot}(E_x) = \frac{1}{T} \exp\left(\frac{E_x - E_0}{T}\right)$ (3.20)

Here, T is the nuclear temperature and E_0 is the parameter that is adjusted with the experimental discrete nuclear level.

3.1.4.3 Microscopic level densities and Generalized superfluid model

S. Goriely has evaluated the nuclear level densities based on the Hartree- Fock method for the excitation energies of up to 150 MeV and spin values of up to 30 [32]. These values were calculated for the reference input parameter library (RIPL). In this approach, the deformed Skyreme-Hartree-Fock-Bogolyubiv approach was adopted to predict the nuclear density. The generalized superfluid model (GSM) model includes superconducting pairing into its approach based on the Bardeen-Cooper-Schrieffer theory [32]. This method is also divided into two regions of low and high energy. High energy region is described by the FGM model and low energy region is characterized by a phase transition from superfluid behaviour. In the low energy region, the nuclear level density is influenced by the pairing correlations. GSM model calculates nuclear density for low energy region as:

$\rho_{GSM}^{tot}(E_x) = \frac{1}{\sqrt{2\pi\sigma}} \left(\frac{e^S}{\sqrt{D}}\right)$ (3.21)

Here, D is related to saddle point approximation and s is the entropy of the system. As per the GSM model, the effective excitation energy is given by

$$U = E_x + \chi\Delta_0 + \delta \quad (3.22)$$

χ is 2 (for odd-odd nuclei), 1 (for even-odd nuclei) and 0 (for even-even nuclei) and δ is an adjustable parameter fitted with experimental data.

3.1.5 Double differential cross section

Kalbach and Mann studied the experimental data of DDX of outgoing particles and based on their study, they derived an empirical formula to predict the double differential cross section as [18];

$$\frac{d^2\sigma}{dEd\Omega} = \frac{1}{4\Pi}\left(\frac{d\sigma^{PE}}{dE}+\frac{d\sigma^{Comp}}{dE}\right)\frac{b}{sinb}(\cosh(b\cos\theta)+f_{msd}(E_k)\mathrm{Sinh}(b\mathrm{Cos}\theta)) \quad (3.23)$$

Here, θ represents the scattering angle, b represents the slope parameter which is based on the angular distribution of outgoing particle, and f_{msd} represents the multi-step ration which is given by;

$$f_{msd} = \frac{d\sigma^{PE}}{dE} / \left(\frac{d\sigma^{PE}}{dE}+\frac{d\sigma^{Comp}}{dE}\right) \quad (3.24)$$

Here, $\frac{d\sigma^{PE}}{dE}$ is the preequilibrium spectra and $\frac{d\sigma^{Comp}}{dE}$ is the compound nuclear spectra.

3.2 Contribution of different reaction modes to total nuclear reaction rate

In this section, the contribution of different reaction modes to total reaction is studied for tungsten, iron and chromium. Iron and chromium are the medium Z materials while tungsten is a high Z material. The energy differential cross section (EDX), often termed as the energy spectra (dσ/dE), is the probability of emitting an outgoing particle at a particular energy. It provides the information of energy distribution of the outgoing

particle. The EDX of outgoing particles also gives an insight into different reaction mechanism in the total reaction. To check the contributions of different nuclear reaction modes to total reaction, the EDX of outgoing protons and alpha particles from neutron induced reactions on ^{184}W at 10, 12 and 14 MeV energy are calculated and presented in Fig. 3.1. The nuclear models that are used in these calculations are given in Chapter 4. From the ^{184}W(n,p) reaction channel, it is evident that the contribution from the pre-equilibrium and direct reaction mechanisms are dominant while the contribution from compound nuclear mechanism is negligible. Avrigeanu et al. [83] had also studied the preequilibrium emission of proton in neutron induced reaction in ^{184}W and stated the same dominant nature of pre-equilibrium emission in the (n,p) reactions in ^{184}W for fusion neutrons. The calculated EDX data of outgoing protons and alpha particles have also been compared with the data from the ENDF-VIII [41] and TENDL-2017 [84]. The nuclear data in the ENDF-VIII data library for ^{184}W was evaluated with the Empire-2.1 code [33] using the Hauser Feshbach model along with the HRTW width fluctuation model for compound nuclear reactions, exciton model for pre-equilibrium calculation with the PCROSS code, and direct and optical model calculations with ECIS03 code. The nuclear data in the TENDL-2017 library was evaluated with the default models of TALYS code except for the modification in level density parameters, and optical model parameters (rv and av). The level density parameters were adopted from the Fermi back shifted model. rv and av parameters were modified using rvadjust and avadjust input keywords in TALYS code. rv and av parameters were modified to 1.01 for the (n,p) reaction channels and 0.96 for the (n,α) reaction channels. The calculated EDX of outgoing protons comes out to be higher than the EDX from TENDL-2017 for 10, 12 and 14 MeV incident neutrons. Validation of these nuclear models are detailed in

Chapter 4. On the contrary to tungsten or high mass elements, low and medium mass elements e.g. iron and chromium show dominant contribution from compound nuclear reaction mechanism.

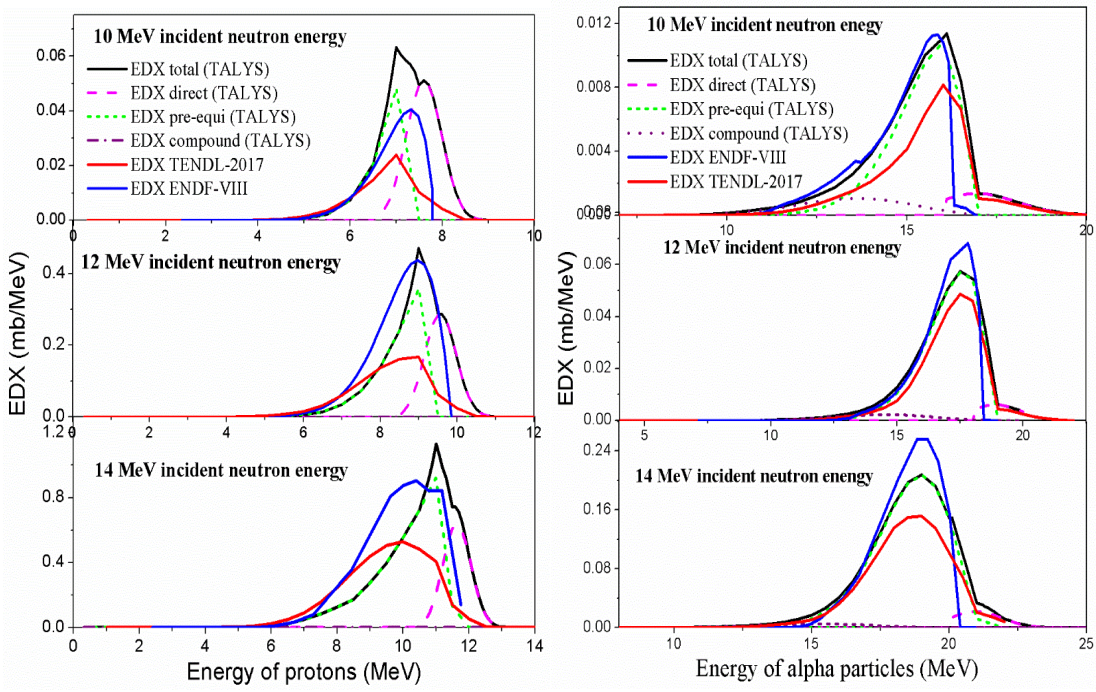

Fig 3.1 Calculated EDX of protons and alpha particles from ^{184}W at 14, 12 & 10 MeV neutron energy

Similarly, the contribution of these three reaction modes namely, compound nuclear, pre-equilibrium and direct nuclear reaction mechanism are also checked in chromium and iron and presented in fig. 3.2. The most probable protons to be emitted from ^{184}W, comes out to be of 7, 9, 11 MeV energy for the incident neutron of 10, 12 and 14 MeV energy, respectively. For the medium mass materials of 50-60 range, most probable emitted protons are of 5 MeV energy at 14 MeV incident neutrons. From the $^{184}W(n,\alpha)$ reactions, it is evident that the most probable emitted alpha particles to be emitted are 16, 17.5 and 19 MeV energy for the incident neutrons of 10, 12 and 14 MeV energy.

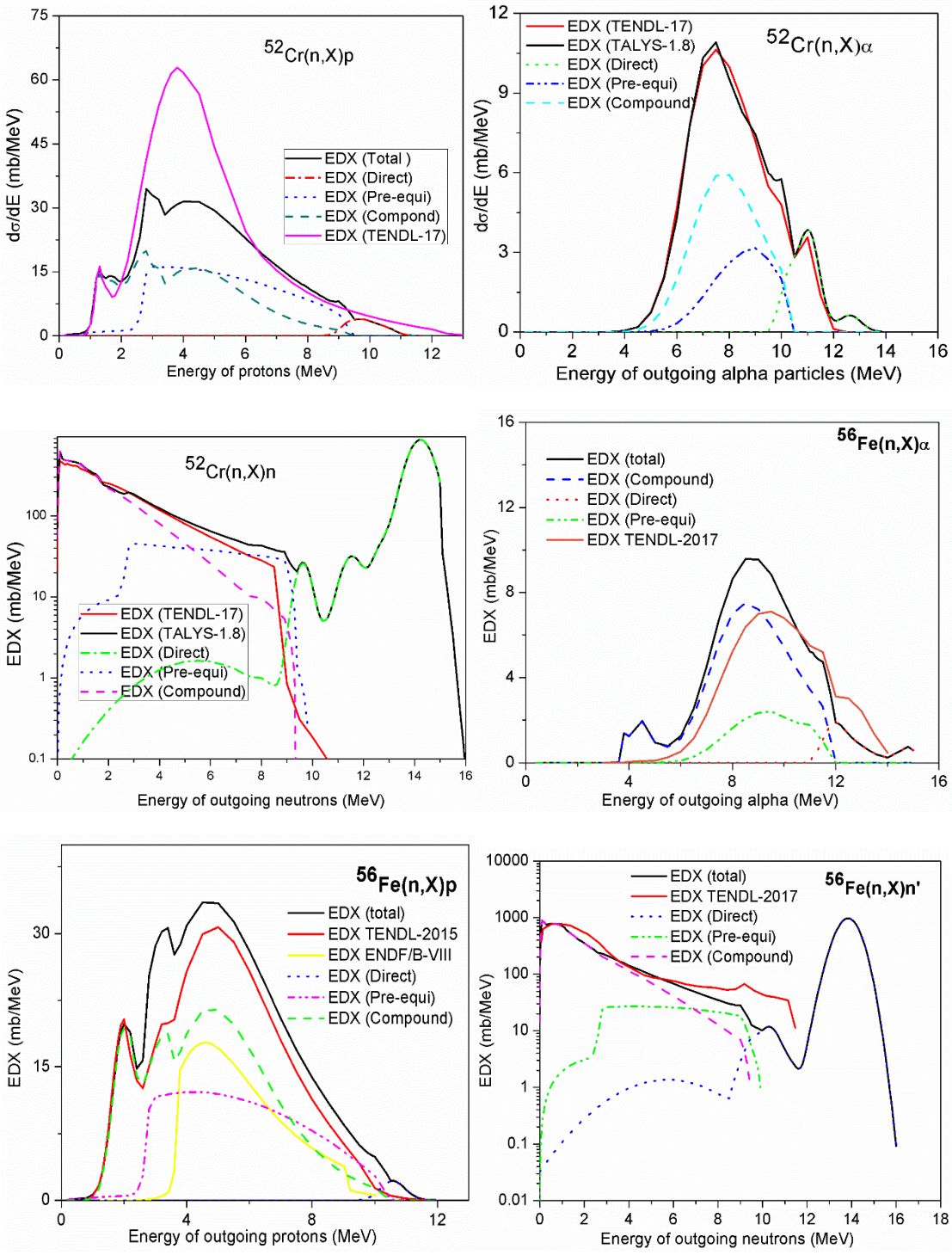

Fig. 3.2 Contribution of direct, pre-equilibrium and compound nuclear mechanism to total reaction rate for ^{52}Cr, ^{56}Fe target for 14.1 MeV neutron irradiation

The dominant reaction mechanism comes out to be pre-equilibrium reaction mechanism. The contributions from direct and compound nuclear reaction mechanism

to total reaction are less compared to the pre-equilibrium mechanism. Most dominant alpha particles to be emitted from (n,α) reactions from the isotopes of the mass region of 50-60 are of 8 to 10 MeV energy at 14.1 MeV neutron energy.

The higher energy protons and alpha particles are produced due to the greater contribution of pre-equilibrium and direct nuclear reaction mechanisms in ^{184}W. In iron and chromium, the major contribution to the total reaction rate is from compound nuclear reaction mechanism and pre-equilibrium emission. EDX of the outgoing neutron is also calculated for ^{52}Cr and ^{56}Fe and presented in Fig. 3.2. It is clear from this study of different reaction modes that compound nuclear, pre-equilibrium and direct reaction contribute to the total reaction and these three must be considered in the estimation of total reaction cross section.

3.3 Methodology and calculation methods to predict the nuclear cross section data

As discussed in the previous chapters, the reaction cross section data, EDX and DDX data of outgoing particles are important to quantify the displacement damage, transmutation and gas production. Due to the scarcity of these experimental data, it is essential to evaluate these data using the nuclear reaction codes e.g. TALYS, Empire and GNASH. In the present thesis, these nuclear data are calculated with the TALYS 1.8 code. In its default mode, nuclear models used by the TALYS-1.8 code are given below;

- Optical model and direct reaction calculations with the optical model parameters of Konning et al [42]
- Compound nucleus calculations with Hauser Feshbach mechanism along with the Moldauer width fluctuation correction factor

- Pre-equilibrium calculations with two-component exciton model
- Direct reaction calculations with distorted wave born approximation mechanism
- Level density parameters are taken from Fermi temperature and gas model

Apart from these models, many alternate nuclear models and parameters can be revised. In the present thesis, nuclear models are selected based on their agreement with existed nuclear data from the EXFOR data library [44]. In the next section, the optimization of nuclear models and their comparison with the experimental data has been demonstrated for $^{56}Fe(n,n')^{56}Fe$ reaction channel.

3.4 Optimization of nuclear models for $^{56}Fe(n,n')^{56}Fe$ reaction channel

As the energy spectra of recoils cannot be measured experimentally but is evaluated with the energy differential spectra of respective outgoing particles, associated with that recoil. To select and validate the nuclear models and parameters in the present work, EDX data of outgoing particles (neutrons, protons and alpha particles) are calculated and compared with the experimental data from the EXFOR library and evaluated nuclear data from the ENDF-VIII [41] and TENDL-17 [42]. The first step in the optimization of nuclear models is to calculate the differential cross section of outgoing neutrons at 14.1 MeV incident neutron with different combinations of nuclear models and compare their predictions with the existing experimental data. These nuclear models are selected in TALYS-1.8 code. The EDX of outgoing neutron for 14.1 MeV neutron irradiation is calculated with the different set of nuclear models and compared with the experimental data of Kozyr et al [85]. This comparison is given in Fig. 3.3. In this comparison, the EDX is calculated with different combinations of nuclear models and their details are given as;

1. Default models of TALYS code that are mentioned in Section 3.3.
2. Width fluctuation correction factor calculated with the Hofmann Richert Tepel Weidenmuller model (WFC2), Level density parameters calculated with the Fermi back shifted model (LDM2), and preequilibrium calculations calculated with the exciton model (Preequi2) are used. The nuclear models and parameters other than these are the default nuclear models.
3. Pre-equilibrium calculations carried out with the multi-step nuclear models (Preequi4) are implemented with the other default nuclear models of TALYS code.
4. Pre-equilibrium calculations carried out with the multi-step nuclear model (Preequi4) and level density parameters calculated with level densities from Goriely's table (LDM4) are implemented with the other default models of TALYS code.
5. Compound nuclear calculations carried out with the pure Hauser Feshbach model (WFC0), pre-equilibrium calculations carried out with the multi step compound nuclear model (preequi4), level density parameters calculated with the constant temperature and fermi gas model (LDM1) along with the other default models of TALYS code are implemented.

These five combinations of nuclear models are used to calculate the EDX of outgoing neutrons and their predictions are compared with the EDX data of Kozyr et al [85]. This comparison is presented in Fig. 3.3. In the energy spectra of outgoing neutrons, neutrons from (n,el), (n,inel), (n,np) and (n,2n) reaction channels have been taken into consideration. Kozyr et al. [85] had reported only inelastic scattering cross sections at 14.1 MeV incident energy neutrons. The mean per cent deviation (MPD) which is the

measure of deviation in the measured or calculated value from the expected or true value is calculated as

$$\text{MPD}=\frac{1}{n}\sum\left(\frac{observed\ value-actual\ value}{actual\ value}\right)*100 \quad (3.25)$$

MPD has been calculated for all the predicted EDX data with respect to the experimental data from the EXFOR data library and given in Table 3.1.

Table 3.1 MPD of all predicted EDX of outgoing neutrons with respect to experimental data

Sr. No.	Nuclear models	MPD
1	Default nuclear models of TALYS	11.20 %
2	WFC2, LDM2, Preequi2	10.6 %
3	Preequi4	11.25 %
4	LDM4, Preequi4	10.56 %
5	WFC0, Preequi4, LDM1	9.9%

Based on this comparison, WFC0, Preequi4, LDM1 are chosen to be the preferred nuclear models for these calculations. These selected nuclear models (WFC0, Preequi4, LDM1) predict the best-fitted data whose values are close to the experimental data. The calculated EDX data, obtained with the TALYS code, are again compared with the data from Empire calculations (using its default nuclear models), experimental data of Kozyr et al. [85], G. Stengl et al. [86], T. Villaithong et al. [87], S. Matsuyama et al. [88], A. Takahashi et al. [89], and evaluated data from the ENDF/B-VIII [11] and TENDL-15/17 [12] data libraries. This comparison of the EDX data of the outgoing neutrons from ^{56}Fe

and natural iron (^{Nat}Fe) for the neutron irradiation of 14.1 MeV neutron energy are presented in Fig. 3.4.

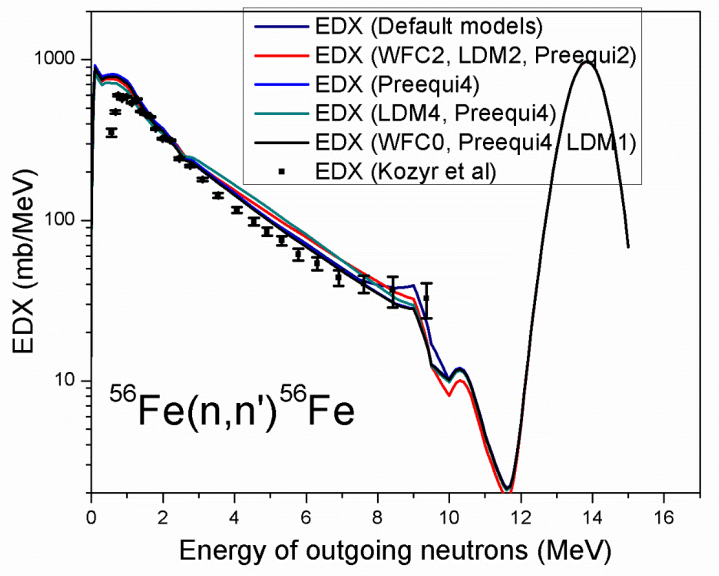

Fig. 3.3 Comparison of the predicted EDX of outgoing neutron from different nuclear models and their comparison with the experimental result

In the energy spectra of outgoing neutrons (Fig. 3.4), neutrons from (n,el), (n,inel), (n,np) and (n,2n) reaction channels are taken into consideration. The calculated EDX of outgoing neutrons, predicted with the TALYS code, are in good agreement with the experimental data. Kozyr et al. [85] and Stengl et al. [86] reported only the inelastic scattering cross-section of ^{56}Fe(n,n')^{56}Fe reaction at 14.1 MeV incident neutron energy. The EDX data predicted with the Empire code underestimates the experimental data at low outgoing neutron energies of 0-2 MeV. Present calculated data and data from the TENDL-15/17 are in good agreement with the experimental data while nuclear data from the ENDF-VIII overestimates the experimental data of EDX of outgoing neutrons. The TENDL-15/17 and ENDF/B-VIII data libraries were evaluated with the TALYS-1.8 and EMPIRE-3.2 codes, respectively using their default and modified nuclear

models. The EDX of the outgoing neutron from ^{Nat}Fe (Natural iron) is also calculated and compared with the experimental data of T. Villaithong et al. [87], S. Matsuyama et al. [88], A. Takahashi et al. [89]. These experimental data contain the high energy scattered neutrons from the shape elastic and compound elastic contributions. These experimental data are in very good agreement with the calculated data.

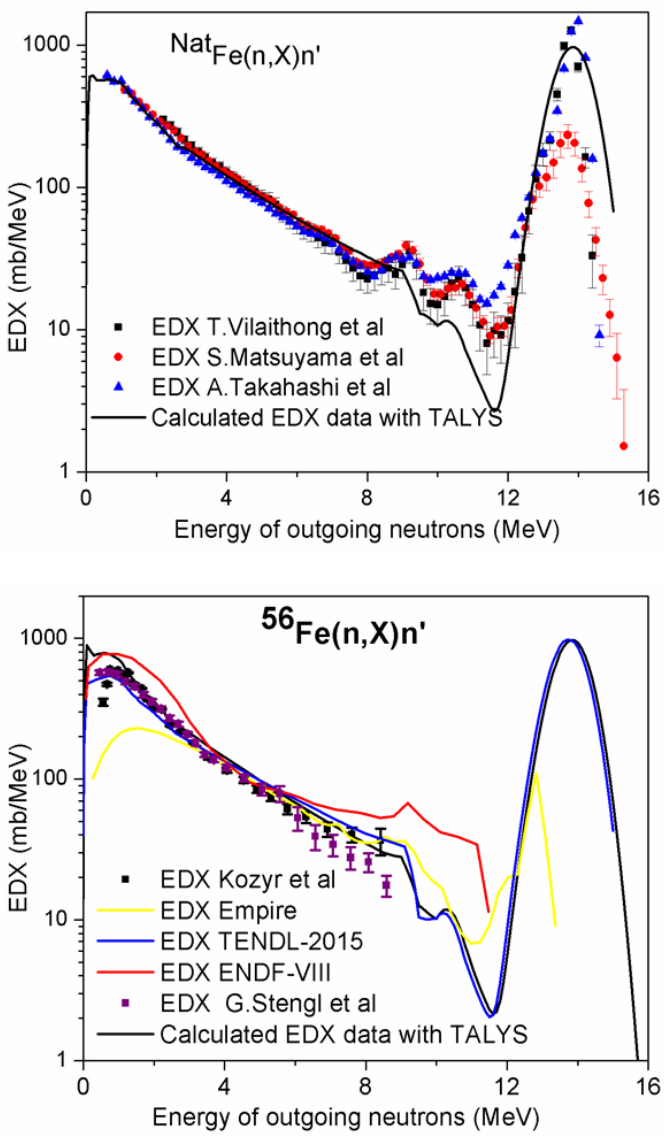

Fig. 3.4 EDX of outgoing neutron from neutron induced reactions on ^{56}Fe and ^{Nat}Fe at 14.1 MeV energy

The MPD has been calculated for all the evaluated data including the calculated work of the present thesis with respect to experimental data from the EXFOR data library for ^{56}Fe and given in Table 3.2.

Table 3.2 MPD of evaluated and calculated data with respect to experimental data for iron

Reaction channel	ENDF-VIII	Calculated data using TALYS-1.8	TENDL-15/17	Empire 3.2 with default models
(n,n')	>25 %	9.9 %	15 %	25 %

It is observed from the calculation of EDX of outgoing particles, that data obtained by the TALYS-1.8 of present work are in better agreement with the experimental work than other evaluated data libraries.

A similar technique to optimize the nuclear models has been adopted for all the stable isotopes of iron, tungsten and chromium. The nuclear data of open reaction channels in the form of EDX or reaction cross section have been calculated and discussed in the next chapter.

3.4 Summary

In this chapter, different nuclear models and reactions are explained. The contributions of different nuclear modes to the total reaction rate are also checked for iron, tungsten, and chromium. The optimization of nuclear models has been carried out for $^{56}Fe(n,n')^{56}Fe$ reaction channel. This optimization is carried out based on the comparison of calculated data with the existing experimental data. The selected nuclear

models (WFC0, Preequi4, LDM1) predict the best-fitted data that is in better agreement with the experimental nuclear data. A similar approach of nuclear models' optimization has been carried out for other reactions in iron, tungsten and chromium. Their results have been discussed in next chapter.

CHAPTER 4: CALCULATION OF DIFFERENTIAL CROSS-SECTION OF OUTGOING PARTICLE AND RECOILS

4.1 Introduction

In the previous chapter of this thesis, nuclear models and their optimization methods have been demonstrated for (n,n') reaction in ^{56}Fe at 14.1 MeV energy. In this chapter, nuclear models are validated for all the open reaction channels in the stable isotopes of iron, tungsten and chromium. These optimized nuclear models are later used to calculate the energy spectra of recoils.

Iron has ^{54}Fe, ^{56}Fe, ^{57}Fe and ^{58}Fe stable isotope with the isotopic abundance of 5.84%, 91.75%, 2.11% and 0.286 %, respectively. Different nuclear models for different reaction channels are selected to predict the nuclear cross section data and validated with the experimental data. In the previous chapter, nuclear models are optimized for (n,n') reaction channel. Similarly, nuclear models have been optimized for other reaction channels and are given as:

- For the (n,p) and (n,np) reaction channels, compound nuclear reaction calculations are calculated with the Hauser Feshbach model with the Moldauer width fluctuation factor, pre-equilibrium reaction calculations are calculated with the multistep compound nuclear model and back shifted fermi gas model is used for level density parameters.
- For the (n,α), (n,2n), and (n,ϒ) reaction channels, pure Hauser Feshbach model is adopted for compound nuclear calculations, pre-equilibrium calculations have been carried out using the multi-step compound model and constant temperature

and Fermi gas model has been adopted for level density parameters. The nuclear model other than these are default models of TALYS code.

Tungsten has ^{180}W, ^{182}W, ^{183}W, ^{184}W, and ^{186}W stable isotopes with the isotopic abundance of 0.12%, 26.50%, 14.31%, 30.4% and 28.43%, respectively. Level density model of constant temperature and fermi gas predicts the best-fitted cross-section data for the (n,p) and (n,np) reactions, Fermi back shifted model [38] predicts the best-fitted data for the (n,α) and (n,nα) reactions. Level density parameters from the Goriely's tables predict the best-fitted data for (n,n') and (n,2n) reaction channel with the pure Hauser Feshbach model of compound nuclear calculations. Other nuclear models that are used in these calculations of cross section data for tungsten are the default models of TALYS code.

Chromium has ^{50}Cr, ^{52}Cr, ^{53}Cr and ^{54}Cr stable isotopes with the isotopic abundances of 4.3%, 83.7%, 9.5%, 2.3%, respectively. For the (n,p), (n,np), (n,n') and (n,2n) reaction channels, pure Hauser- Feshback model for compound nuclear calculation, multistep compound model for preequilibrium calculations and constant temperature Fermi gas model has been used in the cross section and EDX calculations. For the (n,α), (n,nα) reaction channels, Hauser Feshback model with the Moldeur width fluctuation correction for compound nuclear calculations, multi-step compound model for pre-equilibrium calculations and fermi back shifted model for level density parameters are opted in the cross section calculations.

These nuclear models have been used to calculate the nuclear cross section data and compare this calculated data with the experimental data from the EXFOR data library and other nuclear data from evaluated nuclear data libraries. The discrepancies among

the calculated and other evaluated existed data with the experimental data are discussed in the next section.

4.2 Results and discussion

4.2.1 Validation of nuclear models and calculation of recoil spectra for iron

The EDX of outgoing protons and alpha particles are calculated with the TALYS-1.8 code (with selected nuclear models) and EMPIRE-3.2 (default nuclear models). The calculated EDX from the TALYS code have been compared with the data from Empire calculations (using its default nuclear models), experimental data of Grimes et al [35] and Fischer et al [90], and evaluated data from the ENDF/B-VIII and TENDL-17 data libraries. The comparison of calculated data, evaluated data from data libraries and experimental data are presented in Fig. 4.1 and 4.2 for the outgoing protons and alpha particles. The calculated EDX data with TALYS code compares well with the experimental data for both the outgoing particles. The results from the Empire code with its default modes overestimates the EDX data in the 3 to 9 MeV energy region for the (n,p) reaction channel and 5 to 11 MeV energy region for the (n,α) reaction channels. It is concluded after the calculation of EDX of protons that the EDX data from TENDL-17 compares well with the present calculated data while the ENDF-VIII overestimates the EDX data for protons (Fig. 4.1). It is noted from the comparison of EDX data of outgoing particles with the experimental and evaluated nuclear data that the selected nuclear models and parameters produce the best fitted nuclear data and can be used to calculate the energy spectra of recoils. Similarly, the EDX of outgoing alpha particles also compares well with the experimental data.

To check the accuracy of the calculated nuclear data and other evaluated data from the EDNF and TENDL data libraries, the mean percent deviation (MPD) has been calculated with respect to the experimental data and given in Table 4.1.

Table 4.1 MPD of evaluated and calculated data with respect to experimental data for tungsten

Reaction channel	ENDF-VIII	Calculated data using TALYS-1.8	TENDL-15	Empire 3.2 with default models
(n,p)	>40 %	4.6 %	12 %	33 %
(n,α)	-	4.9 %	21 %	>40 %

It is observed from the calculation of EDX of outgoing particles, that calculated data obtained with the TALYS-1.8 code are in better agreement with the experimental work than other evaluated data libraries. This validates the nuclear models for further calculation of recoil spectra.

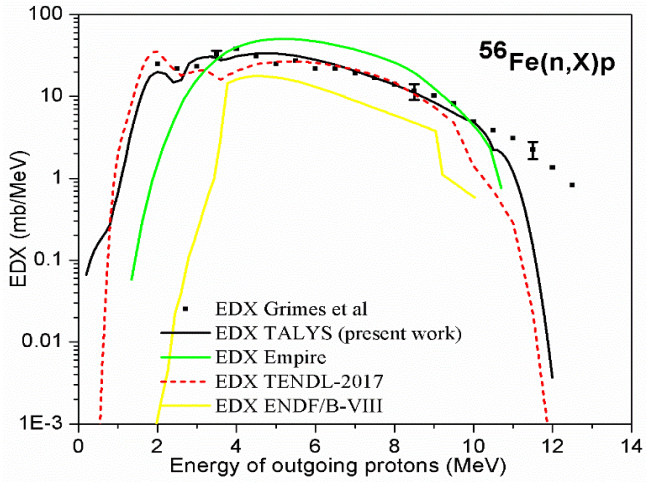

Fig. 4.1 EDX of outgoing protons from neutron induced reactions on ^{56}Fe at 14.1 MeV energy

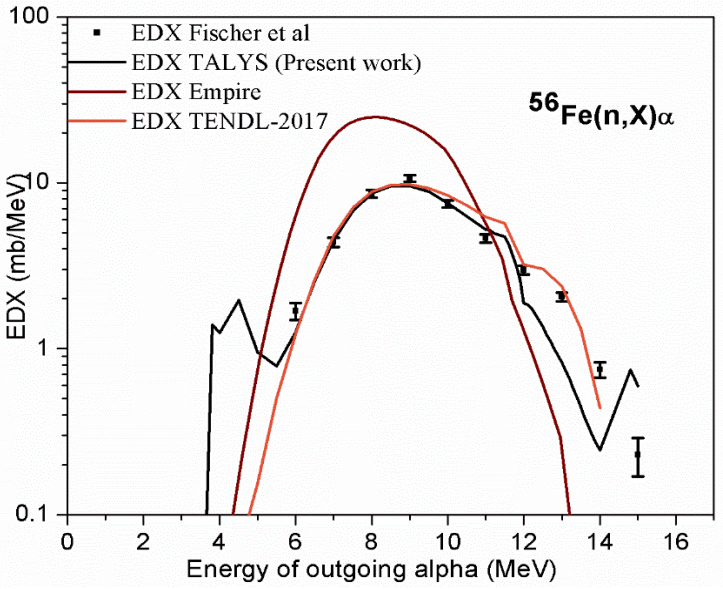

Fig. 4.2 EDX of outgoing alpha particles from neutron induced reactions on ^{56}Fe at 14.1 MeV energy

Recoil nucleus which often terms as the primary Knocked on atoms (PKA), are generated along with the outgoing particles in the nuclear reactions. The energy spectra of recoils are calculated with the adopted nuclear models and parameters for all the open reaction channels in ^{54,56,57,58}Fe. The recoil spectra from ^{56}Fe were also studied by Gilbert et al [14], [15] using the SPECTRA-PKA code. Gilbert et al produced recoil spectra using the nuclear data from the TENDL nuclear data library. Similarly, SPECTER [53] and SPKA [91] can also produce recoil spectra using nuclear data from various nuclear data libraries such as the ENDF/B and TENDL. As discussed earlier, the displacement damage cross section depends on the energy spectra of recoil or PKA, any inaccuracies in the recoil data would result in the inaccurate estimation of displacement damage cross section. In the calculation of EDX of outgoing particles, discrepancies between the experimental data and evaluated data from the ENDF/B-VIII and TENDL-2015 have been stated.

Recoil spectra of $^{56}Fe(n,p)^{56}Mn$, $^{56}Fe(n,np)^{55}Mn$, $^{56}Fe(n,n')^{56}Fe$, $^{56}Fe(n,2n)^{55}Fe$, $^{56}Fe(n,\alpha)^{53}Cr$ and $^{56}Fe(n,\Upsilon)^{57}Fe$ reaction channels have been calculated for the neutron irradiation of up to 15 MeV energy and presented in Fig. 4.3 for 14.1, 10, 6, and 1 MeV incident energy neutrons.

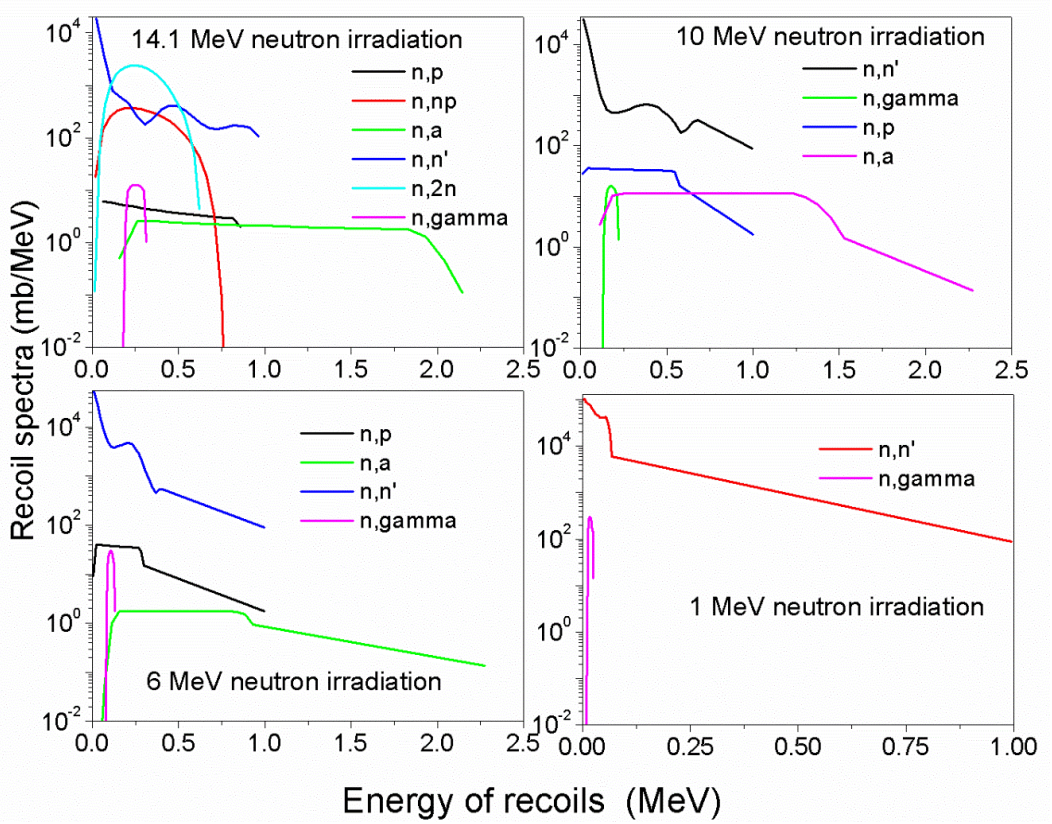

Fig. 4.3 Energy spectra of recoils from ^{56}Fe at different neutron irradiation energies

It is noted from the energy spectra of recoils for 14.1 MeV neutron irradiation that (n,n'), (n,2n), and (n,np) are among the significant contributing reaction channels that produce recoil. At lower energies of neutrons, (n,2n), and (n,np) are not contributing as threshold energies for (n,2n) and (n,np) reaction channels in ^{56}Fe are 11.37 MeV and 10.307 MeV, respectively. Similarly, the (n,p) reaction channel is open beyond 2.9 MeV neutron energy and the (n,α) reaction channel has a very low reaction cross section for neutron irradiation of less than 4 MeV energy. It is noted from Fig. 4.3 of recoil spectra

that major recoils that tend to cause displacements are from (n,n') and (n,2n) reaction channels at 14.1 MeV neutrons while at lower energies, (n,n') reaction channel comes out to be dominant one that produces PKA. The contribution from other reaction channels such as (n,p), (n,α), (n,ϒ) and (n,np) are less but not negligible.

4.2.2 Validation of nuclear models and calculation of recoil spectra for tungsten

To validate the nuclear models in the TALYS-1.8 code to predict nuclear cross section for the D-T neutron-induced reactions in tungsten, the excitation functions of (n,el), (n,2n), (n,p) and (n,α) reaction channels are calculated for the neutron irradiation of up to 16 MeV energy and compared with the existing results of evaluated data libraries e.g. ENDF-VIII, JENDL, and JEFF and experimental data from the EXFOR data library [44]. This comparison is presented in Fig. 4.4. No experimental EDX data of outgoing charged particles are available for the isotopes of tungsten. The EDX of outgoing neutrons for the neutron irradiation at 14.1 MeV energy was measured for ^{186}W by Pavlik at al. [92] and later reported by Marcinkowski et al. [93]. The calculated EDX of outgoing neutrons from (n,inel) reaction channel in ^{186}W are compared with the angle-integrated data of the ENDF-VIII, JEFF-3.3, EDX data from the TENDL-2017, ENDF-VII, and Pavlik et al and presented in Fig. 4.5. The calculated data compares very well with the experimental data of Pavlik et al in the energy region of 0-4 MeV. It slightly overestimates the experimental data in the 5-9 MeV energy region. The ENDF-VIII data overestimates the experimental data in the energy range of 2-6 MeV energy and underestimates it in the 0-2 MeV energy region. The EDX data from the TENDL-2017 also shows discrepancies with the calculated data. The discrepancies in the calculated data with the ENDF, JEFF and TENDL data libraries arise due to the usage of different nuclear models and parameters. Previously, angle energy spectra (double

differential cross section) of outgoing neutrons from (n,2n) reaction channels were not present in the ENDF-VI and ENDF-VII data libraries. From the comparison among the experimental data of Pavlik et al, ENDF-VIII, JEFF-3.3 and TENDL-2017, It is noted that the calculated data of the present work are in better agreement than the data from existing data libraries of tungsten.

Similar to the case of iron, MPD has been calculated for all the evaluated data including the calculated data of the present thesis with respect to experimental data from the EXFOR data library and given in table 4.2.

Table 4.2 MPD of evaluated and calculated data with respect to experimental data

Reaction channel	JEFF-3.2	ENDF-VIII	JENDL-4	Calculated data with TALYS-1.8	ENDF-VII	EAF-10	TENDL-17	JEFF-3.3
(n,2n)	6.3 %	15.7 %	18.1 %	7.1 %	-	-	-	-
(n,p)	17 %	-	22 %	19 %	-	-	-	-
(n,n')	<3 %	<3 %	10 %	<3 %	<3 %	-	-	-
(n,α)	-	>40 %	21 %	21.5 %	>30 %	-	-	-
EDX of outgoing neutrons from ^{186}W	-	11 %	-	7.3 %	>40 %	-	4.3 %	>40 %

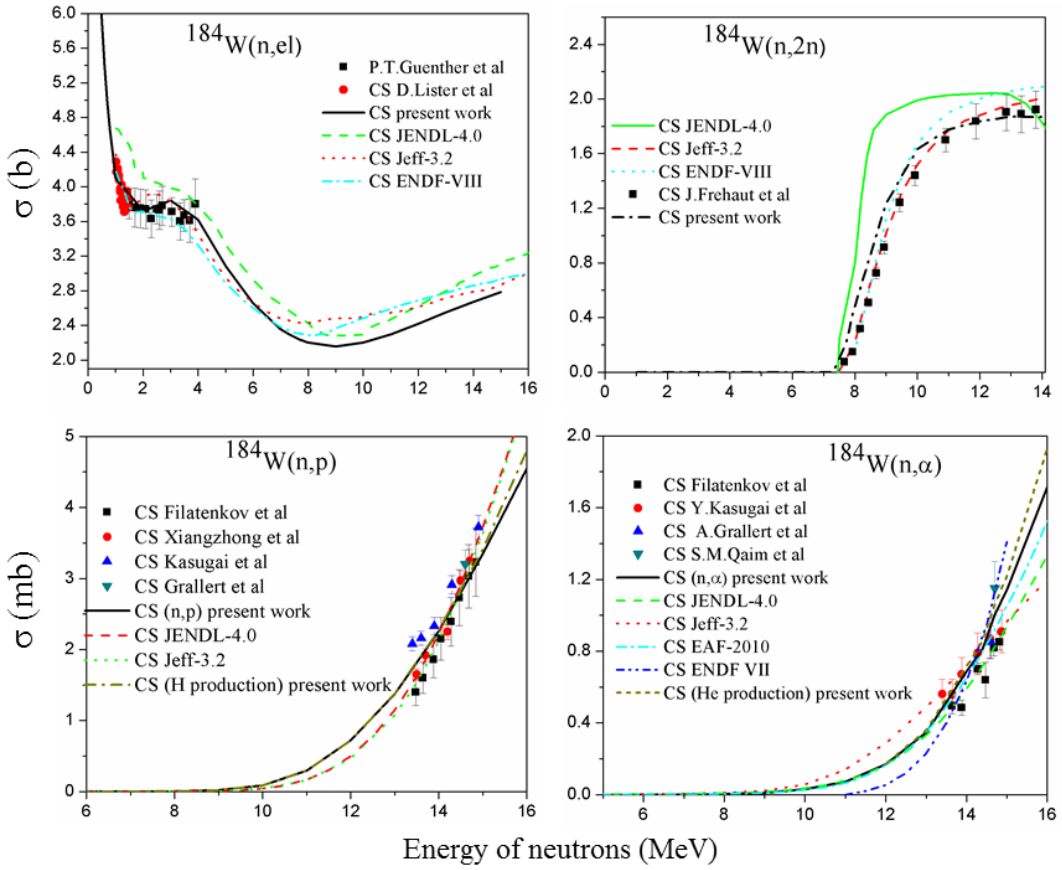

Fig. 4.4 Excitation functions for (n,el), (n,2n), (n,p) and (n,α) reactions in ^{184}W

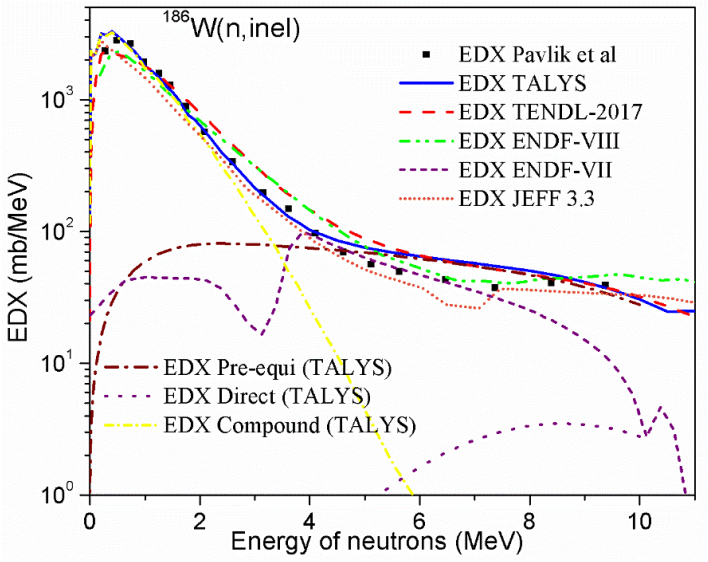

Fig. 4.5 EDX of outgoing neutron from $^{186}W(n,n')$ reactions at 14.1 MeV incident neutron energy

Recoil species of different mass and different energies are produced in the neutron induced reactions based on the open reaction channels e.g. (n,n'), (n,2n), (n,p), (n,α) and (n,γ) etc and act as the primary knocked on atoms (PKA). In the present work, the energy spectra of recoils are calculated with the TALYS-1.8 using the selected nuclear models for tungsten. The energy spectra of recoils from all the stable isotopes of tungsten and iron have been calculated for the incident neutrons of up to 15 MeV energy. The energy spectra of recoils from ^{184}W are presented in Fig 4.6 for neutron irradiation of 1, 6, 10, 14 MeV energy.

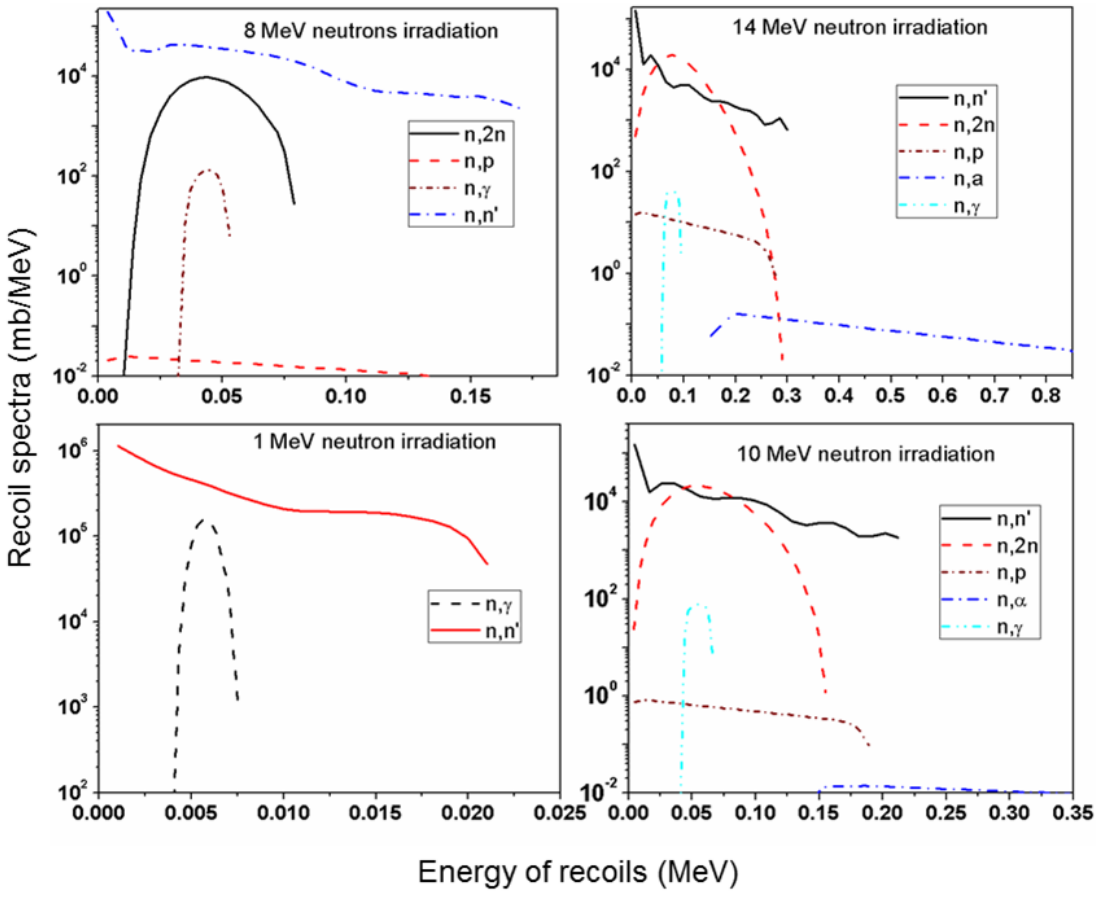

Fig. 4.6 Energy spectra of recoils from ^{184}W at incident neutron energies of 1, 8, 10, 14 MeV

It is noted from the energy spectra of recoils from ^{184}W that contribution from (n,2n) and (n,p) are open for the high energy neutrons as threshold energies for these reaction channels are 7.451 MeV and 2.095 MeV, respectively while other reaction channels such as the (n,n'), (n,α), and (n,γ) are open even for thermal neutron energies. The (n,α) reaction channel has a very low reaction cross section for incident neutrons of up to 10 MeV energy. Similar to this, the energy spectra of recoils are calculated for other stable isotopes of tungsten (^{180}W, ^{182}W, ^{183}W, ^{184}W & ^{186}W).

4.3.3 Validation of nuclear models and calculation of recoil spectra from chromium

To validate the nuclear model for the chromium, the EDX of outgoing particles are calculated and compared with the experimental data of Lychagin et al [94], Grimes et al [35] and evaluated data from the ENDF-VIII and TENDL-17 data library. These comparisons have been presented in Fig. 4.7-4.9. Similar to the iron and tungsten, the MPD has been calculated for all the evaluated data including the calculated work of present thesis with respect to the experimental data from the EXFOR data library and given in Table 4.3. It is noted from the comparison of calculated data with other experimental and evaluated data is that the calculated data are in better agreement with the experimental data than other evaluated data, thus nuclear models are validated for the further calculations of recoil spectra.

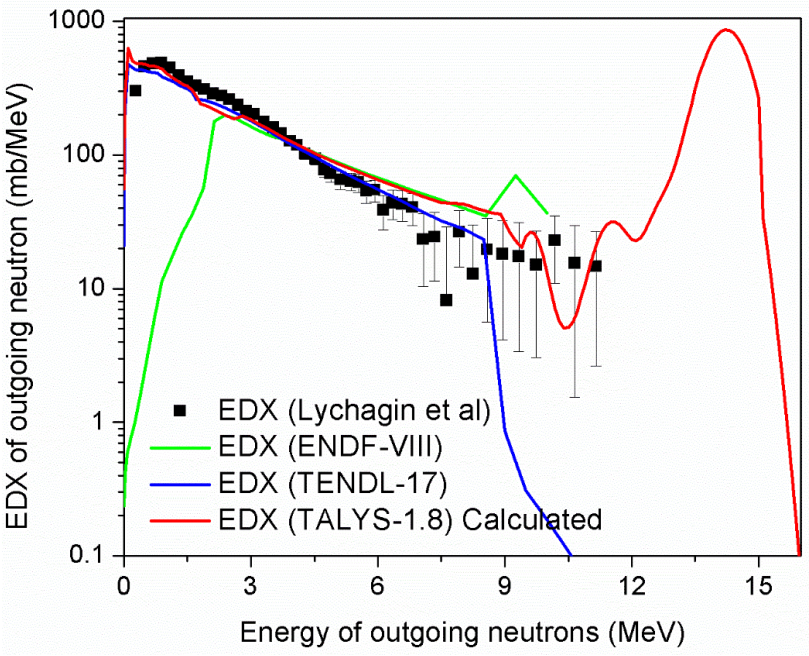

Fig. 4.7 EDX data of outgoing neutrons from ^{52}Cr at 14.1 MeV incident neutrons

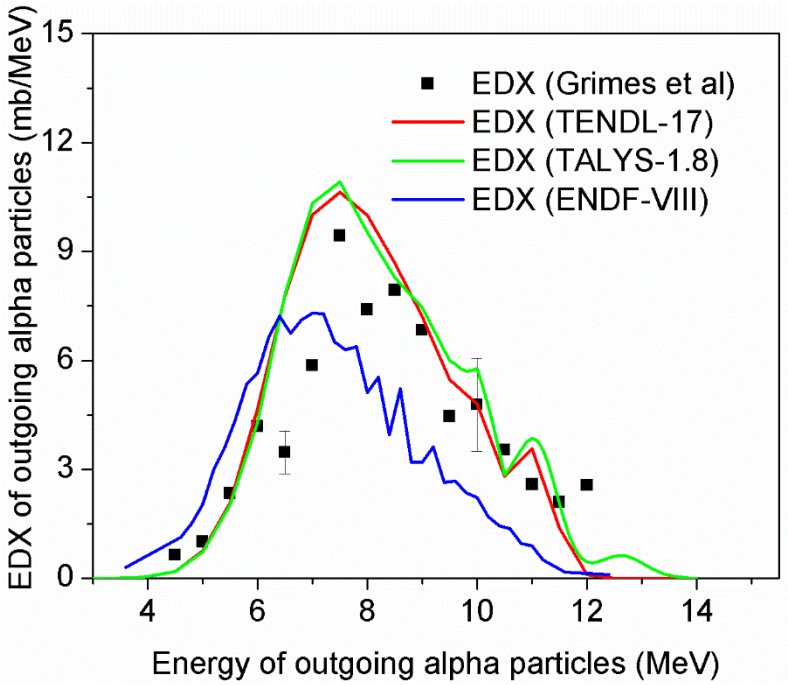

Fig. 4.8 EDX data of outgoing neutrons from ^{52}Cr at 14.1 MeV incident neutrons

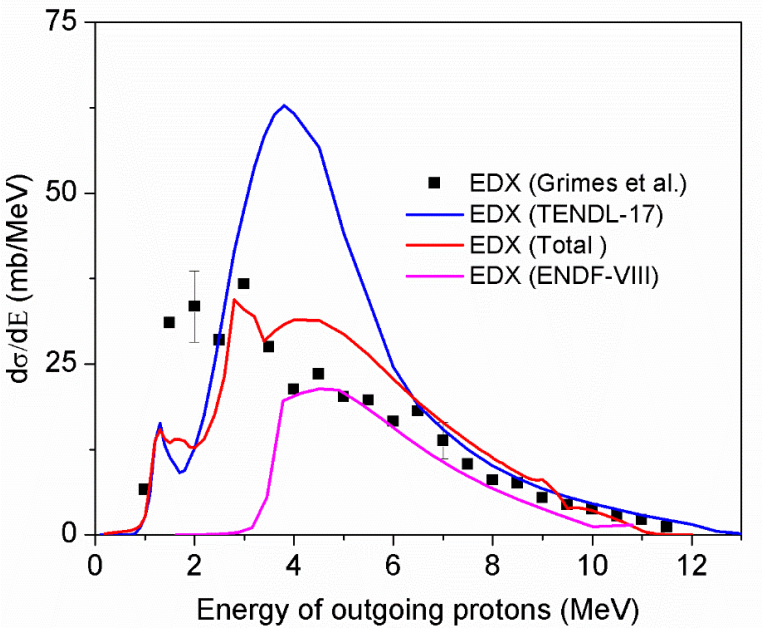

Fig. 4.9 EDX data of outgoing neutrons from ^{52}Cr at 14.1 MeV incident neutrons

Table 4.3 MPD of evaluated and calculated data with respect to the experimental data for chromium

Reaction channels	ENDF-VIII	Calculated data with TALYS-1.8	TENDL-17
(n,n')	>40 %	4.08 %	7.8 %
(n,p)	> 40 %	24 %	29 %
(n,α)	20 %	18 %	18.8 %

Reaction channels such as (n,n'), (n,2n), (n,p), (n,α) and (n,γ) yield different recoil nucleus or recoil atom of different atomic number, mass and energy. The (n,n'), (n,2n), (n,p), (n,α) and (n, γ) reaction channels in ^{52}Cr yield ^{52}Cr, ^{51}Cr, ^{52}V, ^{49}Ti and ^{53}Cr recoil nucleus, respectively. The energy spectra of recoil species are calculated for all the stable isotopes of chromium at up to 15 MeV incident neutrons. In Fig. 4.10, the recoil

spectra from all the open reaction channels in ^{52}Cr are presented for the neutron irradiation of 3, 6, 12 and 14 MeV energy.

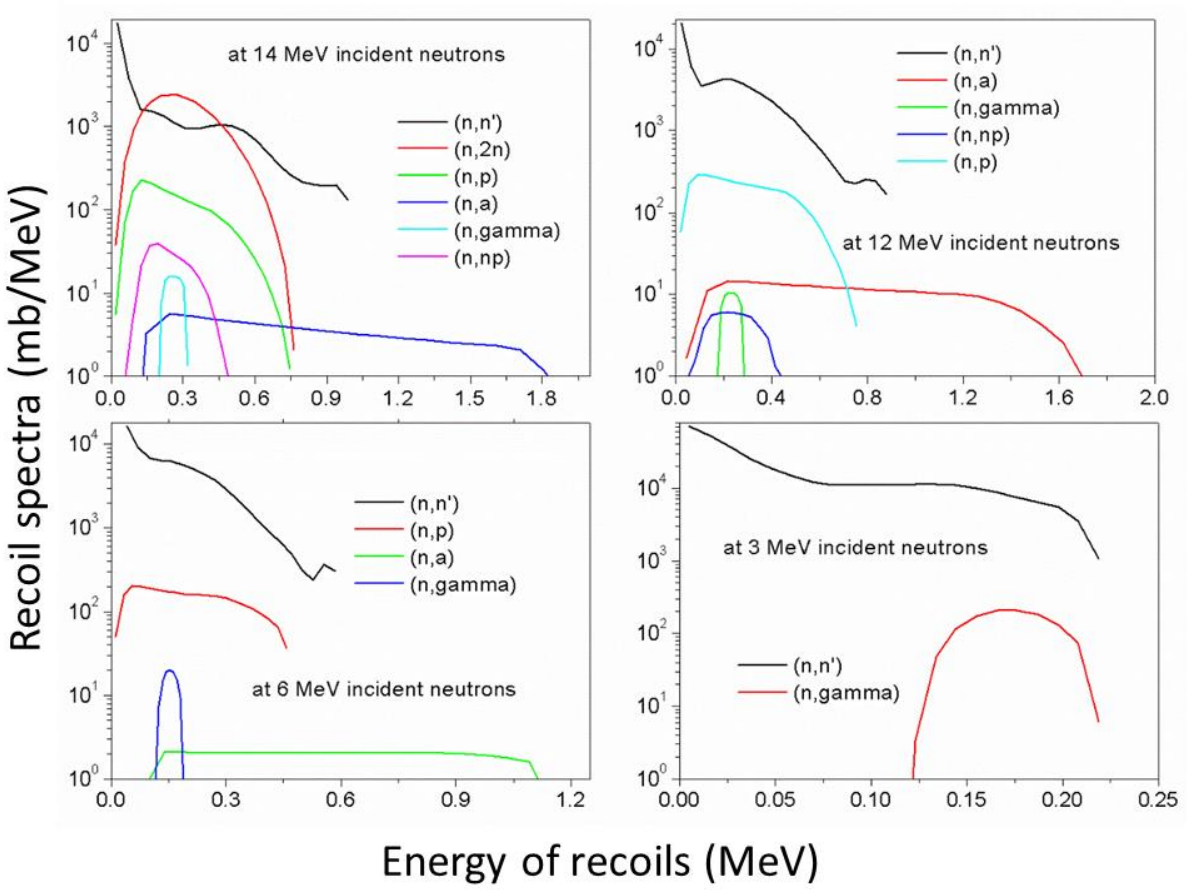

Fig. 4.10 The energy spectra of recoils from ^{52}Cr at incident neutron energies of 1, 8, 10, 14 MeV

4.4 Summary

In this chapter, the nuclear models and parameters have been validated for the prediction of energy spectra of recoils. To validate these nuclear models, the calculated nuclear data are compared with experimental data from the EXFOR and other evaluated nuclear data from evaluated data libraries. It is concluded that,

1. EDX data of outgoing particles (p and α) from ^{56}Fe, calculated with the TALYS-1.8 code using the adopted nuclear models, compares well with the experimental data while the Empire-3.2 in its default mode overestimates the EDX data for protons and alpha particles in 4 to 8 MeV energy region.
2. A good agreement between calculated excitation functions of ^{184}W and experimental results validate the theoretical calculations for the further prediction of EDX of recoils from different reaction channels in the stable isotopes of tungsten. The EDX data of outgoing neutrons from ^{186}W(n,inel) reaction channel have been calculated and compared with the experimental data of Pavlik et al, nuclear data library of TENDL-2017, JEFF-3.3, and ENDF-VIII. The calculated EDX data of outgoing neutrons compares well with the results of Pavlik et al..
3. The EDX data of outgoing neutrons, protons, and alpha particles from ^{52}Cr have been calculated and compared with the experimental and evaluated data from the ENDF-VIII and TENDL-17. The calculated nuclear data shows better agreement with the experimental data than other evaluated data.
4. Based on the adopted nuclear models, recoil spectra are calculated from all the open reaction channels in all stable isotopes of iron, tungsten and chromium.

CHAPTER: 5 GAS PRODUCTION AND TRANSMUTATION IN IRON, TUNGSTEN AND CHROMIUM

5.1 Introduction

Neutrons interact with the materials via nuclear scattering and absorption. The nuclear scattering reaction including elastic and inelastic scattering is often expressed with (n,n') reaction channel and absorption reactions are expressed with (n,γ), (n,2n), (n,p), (n,np), (n,α), (n,nα), (n,d) reaction channels. The product of these reaction channels may be a radioactive isotope and if radioactive, will further decay and change an element into another element via subsequent alpha or beta decay. The light charged particle production reaction channels such as (n,p), (n, np), (n,α), (n, nα), and (n,d) transmutate an element and can produce a proton, alpha particle, and deuterium as the outgoing particle. These outgoing particles become hydrogen, helium and deuterium gas by picking up electrons while slowing down in the reactor materials. These reaction channels along with the inelastic scattering, radiative capture and (n,2n) reaction channels following the subsequent alpha or beta decay change an element into other thus changing its engineering and structural properties. Hydrogen, trapped in the reactor components causes hydrogen embrittlement and decreases the metal-metal bonding between the reactor alloys. It also interacts with the dislocations and causes hydrogen-induced localized plasticity (HELP). Helium due to its low reactive nature can be accumulated at voids, cracks and grain boundaries. The accumulation of helium cause swelling or embrittlement. Helium production in tungsten also causes a limit on its re-weldability. These limits of re-weldability at joints are 3 appm for plates of less than 3 mm and 1 appm for plates of more than 3 mm thickness. This issue of re-weldability

limits the lifetime of tungsten at the weld-able zones. Similar to helium, hydrogen production also causes hydrogen assisted cracking (HAC) in steel weld points. Due to the impacts of helium production on the engineering properties of materials, its limit at the blanket location of EU DEMO is set to be 200 appm and materials need to be replaced after that. It was studied that after the neutron irradiation, equivalent to 52.1 dpa, on pure tungsten can convert 5 % pure tungsten into rhenium and tantalum [19]. M. Fujitsuka et al [20] had studied that this 5 % conversion of pure tungsten into rhenium would decrease its thermal diffusivity to half. Due to their huge impact on the performance and reliability of structural elements, estimation of transmutated products are essential. Similarly, these transmutation elements tend to change the electrical resistivity of W-Os alloy [21]. These problems of gas production and transmutation are not that severe in fission reactors as these reaction channels have cross section thresholds of MeV order. Due to the availability of higher energy neutrons in fusion reactors, these reaction channels take place in fusion reactors and alter the desired functional properties of reactor components. Due to transmutation and activation, several long-lived radioactive wastes are also produced. Due to some experimental limitations such as the low intensity of neutron source in the laboratories, handling of radioactive reaction products and long irradiation scenarios, it is not experimentally possible to predict the material response or inventory build-up in fusion reactor materials. Previously, these studies of transmutation were carried out with the EAF data [46], TENDL data libraries [42] and transmutated impurities were simulated for natural elements. These studies did not provide the results of long-lived radioisotopes that are produced in the fusion reactors and are very important to quantify the radioactive waste. To identify the transmutated isotopes, transmutation calculations have been carried out

with the ACTYS [55] code. The methodology and calculation methods are provided in the next section.

5.2 Methods for estimating nuclear responses

5.2.1 Methods for estimating gas production

Gas production per atom (GPA) is calculated with the gas production cross section of hydrogen and helium production. Hydrogen and helium production reaction channels are presented with (n,xp), (n,xα) reaction channels. These cross section can be extracted from the evaluated nuclear data libraries and can also be calculated with the TALYS-1.8 [32] and Empire-3.2 [33] codes. In the present thesis, these cross sections are calculated with the validated nuclear models using the TALYS code. These nuclear models are introduced and validated in Chapter 3, & 4. In the present work, hydrogen and helium production cross section of iron, tungsten and chromium are calculated for the neutron irradiation of up to 15 MeV energy. Based on these calculated gas production cross-sections, GPA values have been predicted in iron, tungsten and chromium for typical fusion neutron spectrum as:

$$GPA = \sigma(n,p/\alpha).\ \Phi(n).\ T_{irradiation} \tag{5.1}$$

Here, $\sigma(n,p/\alpha)$ is the gas production cross section, $\Phi(n)$ is the neutron flux and $T_{irradiation}$ is the total irradiation time. Neutron spectra have been taken from Gilbert et al [10] [9].

5.2.2 Methods for estimating transmutation

The transmutation studies have been carried out with the ACTYS code [55]. The nuclear cross section data of all the open reaction channels in iron, tungsten, and chromium are calculated and used along with the nuclear data of EAF-07 [46] for other secondary

isotopes. In the ACTYS code, the inventory of build-up isotopes (A→B →C) are calculated with the Bateman equation [54] as;

$$\frac{dnB}{dt} = n_B - \lambda_A n_A e^{-\lambda A t} - \lambda_B n_B \quad (5.2)$$

$$n_B = n_A \sigma(E_n). \Phi(E_n). T_{irradiation} \quad (5.3)$$

Here, $\frac{dnB}{dt}$ is the concentration of nuclide B, λ_A is the decay constant of A, n_A is the concentration of A at the initiation of irradiation, λ_B is the decay constant of B, n_B is the concentration of B, and $\Phi(E_n)$ is the neutron flux. The cross section data of all the open reaction channels in iron, tungsten, and chromium are calculated in 175 groups using the appropriate nuclear models. The nuclear cross section data of (n,n'), (n,γ), (n,2n), (n,p), (n,np), (n,α), (n,nα), and (n,d) for all the stable isotopes of iron, tungsten and chromium are replaced with the calculated data obtained with TALYS-1.8 code in the EAF-07 data library. The cross section data of isotopes other than iron, tungsten and chromium remain same as of EAF-07. In the present work, the time evolution of the concentration of different transmutated isotopes is studied and results have been discussed in next section. The study of transmutation has been carried out in the following steps;

1. The reaction cross section data of open reaction channels are calculated for all the open reaction channels in stable isotopes of iron, tungsten and chromium. This calculated cross section data along with the nuclear data of other secondary elements from EAF-07 are used to calculate the activation and transmutation in iron, tungsten and chromium.

2. The transmutation studies in tungsten are carried out for the neutron spectrum at first wall armour of EU demo reactor [10] where tungsten will be used as the divertor material. A similar study of transmutation in iron and chromium have been carried out for the neutron spectrum at the first wall of EU DEMO reactor [9] where they both are used as the constituents of the SS. These neutron spectra at different locations of fusion reactor are taken from Gilbert et al [9], [12][10]. Gilbert et al [9] had calculated the neutron spectrum at the first wall of EU DEMO having the source strength of $\approx 3.5 \times 10^{20}$ neutrons sec^{-1} per GW thermal power. As per the conceptual design of the EU DEMO, It produces the 1.6 GW thermal fusion power ($\approx 5.6 \times 10^{20}$ neutrons.sec^{-1}). Similarly, neutron spectra at the first wall of ITER were calculated for 500 MW thermal fusion power having the source strength of 1.77×10^{20} neutrons.sec^{-1} [12]. These neutron spectra are also given in chapter 1. These neutron spectra of first wall of ITER and EU demo are also used to predict the GPA and dpa.
3. In these transmutation studies, the time evolution of the concentration of transmutated isotopes have been studied and isotopes that are produced in 5 FPY are identified. Radioactive isotopes have been identified from all the stable isotopes of iron, tungsten and chromium.

Results from these gas production and transmutation studies are discussed in next section.

5.3 Results and discussion

5.3.1 Gas production in iron, tungsten and chromium

Helium and hydrogen production cross section of iron have been calculated using the validated nuclear models using the TALYS-1.8 code. The calculated values are compared with the experimental data of Kokoo et al [40], Grimes et al [35] and Haight et al [95]. The calculated data are presented in Fig. 5.1 along with the cross section data of Kokoo et al., Grimes et al., and Haight et al.. The calculated data compares very well with these experimental data. The threshold energies of hydrogen and helium production reactions in iron are 2 MeV and 4 MeV, respectively. Due to these high thresholds, gas production in iron is not of much importance in fission-based reactors.

In iron, hydrogen and helium production at the first wall armour location of ITER and EU DEMO [6] and the first wall location of EU DEMO reactor [9] are predicted and given in Table 5.1.

Table 5.1 Values of GPA in iron at different neutron spectrum of fusion reactors

Neutron Spectrum	Helium production (appm/FPY)	Hydrogen production (appm/FPY)
ITER FWArmour	490	2093
EU Demo FWArmour	1130	6860
EU Demo FW	128	561

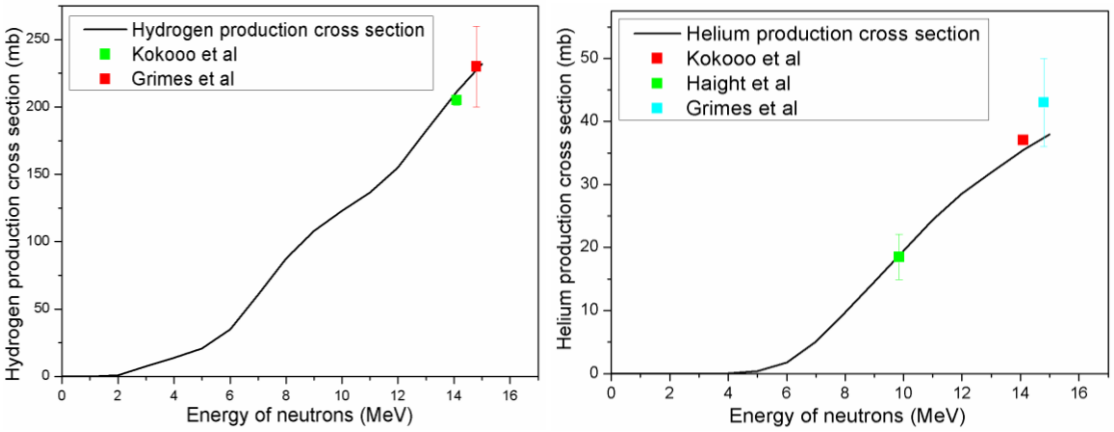

Fig. 5.1 Gas production cross section (Hydrogen and Helium production cross section) of iron

Gilbert et al [57] had also predicted helium and hydrogen production at the same first wall location of EU DEMO reactor using the nuclear data from the TENDL-2011 data library. Gilbert et al predicted hydrogen and helium production to be 615 appm/FPY and 135 appm/FPY [57], respectively. This deviation of GPA values in present and Gilbert et al is due to the usage of different nuclear models used in this work and TENDL-2011.

Similarly, σ_{GPA} (hydrogen and helium production) are also calculated for natural tungsten and chromium using the adopted nuclear models for up to 16 MeV neutron irradiation and presented in Fig. 5.2. The cross section of proton and alpha producing reaction channels have been calculated using the selected nuclear models for all the stable isotopes of tungsten (^{180}W, ^{182}W, ^{183}W, ^{184}W & ^{186}W) and chromium (^{50}Cr, ^{52}Cr, ^{53}Cr & ^{54}Cr). The cross-section data of all stable isotopes are used to get the data for natural chromium and tungsten using their respective isotopic abundances. The calculated σ_{GPA} of chromium has also been compared with the cross section of proton and alpha production [35] at 14.8 MeV neutron energy. For natural tungsten, no

experimental data for the cross section of proton and alpha emission is available in the literature. Based on the calculated gas production cross section, values of produced hydrogen and helium are predicted for the typical D-T neutron spectrum of fusion reactor and these values are given in Table 5.2. Gilbert et al had also predicted the helium production in tungsten and chromium for fusion reactor environment. Similar predictions of helium production had also carried out in Nuclear analysis report [11]. Hydrogen production in tungsten and chromium were not reported in the literature for the D-T neutron spectrum. Gilbert et al predicted the helium production in chromium and tungsten to be 100 appm/FPY and 2.4 appm/FPY, respectively, at the first wall of EU DEMO reactor using the TENDL-2011 data library.

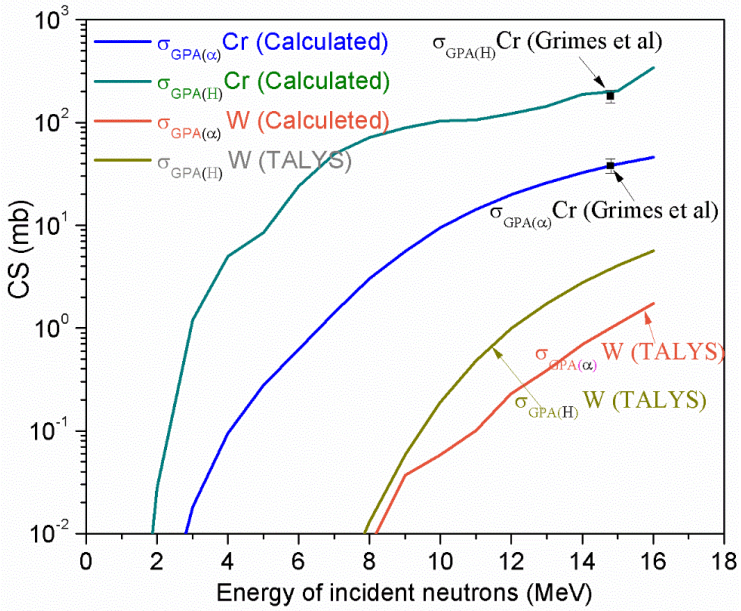

Fig. 5.2 Gas production cross section of chromium and tungsten for D-T neutron irradiation

Table 5.2. Values of gas production in chromium and tungsten for typical neutron spectrum of fusion reactor

	Helium production (aPPM/FPY)			Hydrogen production (aPPM/FPY)		
	ITER FWArmour	EU demo FWArmour	EU demo first wall	ITER FWArmour	EU demo FWArmour	EU demo first wall
Tungsten	14.2	37.3	3.94	56.8	147	13.8
Chromium	696	1760	171	4090	10050	1040

It is noted from the calculation of gas production that hydrogen and helium production in tungsten is very low due to its low reaction cross section. These predicted values of GPA in iron, tungsten and chromium play an important role in defining the lifetime of these materials and their alloys. Iron which is used in the first wall at the blanket location in EU DEMO fusion reactor produces 128 appm/FPY at the same location. As the limit of helium production is 200 appm, iron can be used in EU demo fusion reactor for 1.56 FPY or 4.734 effective operation years (at an average load factor of 33% [96]). Similarly, the lifetime of other materials can also be calculated. Iron and chromium will not be used at the armour location of divertor but GPA in them is also calculated at this location to compare their performance with tungsten. Tungsten due to low helium production cross section can be used for a longer time in a fusion reactor. Although at the weld-joint, its lifetime is limited to 3 appm helium production due to

re-weldability issues [97]. Tungsten at the blanket location in EU demo produces 3.94 appm/FPY thus can be used at connecting weld-joints for 2.30 effective operation years.

5.3.2 Transmutation in iron, tungsten and chromium

5.3.2.1 Transmutation in iron

Four stable isotopes of iron are ^{54}Fe, ^{56}Fe, ^{57}F and ^{58}Fe with the isotopic abundance of 5.84 %, 91.7 %, 2.1 % and 0.2 % respectively. Iron as the primary constituents of SS will be used at first wall, vacuum vessel and shield modules of the fusion reactors. It will face the highest neutron flux at the first wall of fusion reactors. In the present thesis, transmutation studies are carried out for the neutron spectrum at the first wall location of EU DEMO fusion reactor. EU DEMO fusion reactor of 1600 MW fusion thermal power has the neutron source strength of $\approx 5.6 \times 10^{20}$ neutrons.sec^{-1}. This study is carried out for continuous 5 FPY (full power year). The time evolution of the concentration of transmuted isotopes from major stable isotopes of iron $^{(54,56)}$Fe is presented in Fig. 5.3.

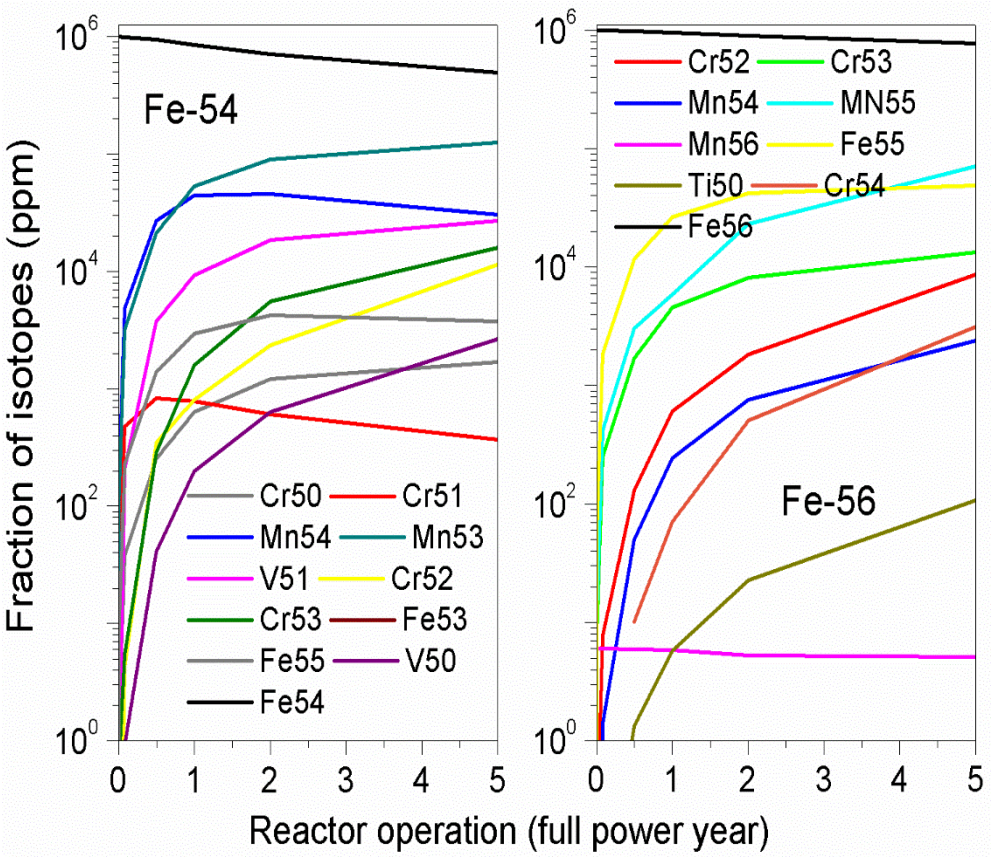

Fig. 5.3 Time evolution of transmutated isotopes from major stable isotopes of iron

In these transmutation studies, all the isotopes that can be produced during the reactor operation are included. ^{50,51,52}Cr, ^{51}V, ^{53,54}Mn, and ^{53,55}Fe are the major transmutated isotopes from ^{54}Fe. A similar assessment of transmutation reveals that ^{52,53,54}Cr, ^{54,55,56}Mn, ^{55}Fe, ^{50}Ti are the major transmutated isotopes from ^{56}Fe. Out of these transmutated isotopes, major isotopes produced during the reactor operations are ^{53}Mn, ^{54}Mn, ^{55}Mn, ^{55}Fe, and ^{51}V. Their concentration in natural iron after 5 FPY operations of the EU DEMO and half-lives are given in Table 5.3. Out of these transmutated isotopes, production of ^{55}Fe, and ^{52,53}Cr are important as ^{55}Fe is a radioactive isotope and ^{52,53}Cr are brittle in nature. The fraction of chromium in natural iron affects its mechanical properties. Other important isotopes that are produced are mentioned in Table 5.3.

Table 5.3 Important transmutated isotopes from iron

Isotopes	Half-life	% in iron after 5 FPY
^{53}Mn	3.1E6 years	1.03 %
^{54}Mn	312 days	0.7 %
^{55}Mn	stable	9.4%
^{55}Fe	2.73 years	4.49%
^{51}V	stable	0.4 %
^{54}Fe	Stable	5.8 %
^{56} Fe	Stable	71.3 %
^{57}Fe	Stable	2.19 %
^{58}Fe	Stable	0.2 %
^{52}Cr	Stable	1.8 %
^{53}Cr	Stable	2.1 %

5.3.2.2 Transmutation in tungsten

Tungsten has ^{180}W, ^{182}W, ^{183}W, ^{184}W and ^{186}W stable isotopes with isotopic abundance of 0.12%, 26.5%, 14.3%,30.6% and 28.43%, respectively. The transmutation in each isotope of tungsten are studied with the ACTYS code and presented in Fig 5.4 for ^{182}W, ^{183}W, ^{184}W and ^{186}W. Tungsten will be used at the first wall armour and at the divertor location of fusion reactors. These transmutation studies have been carried out for the neutron spectrum at the first wall armour location of EU DEMO fusion reactor.

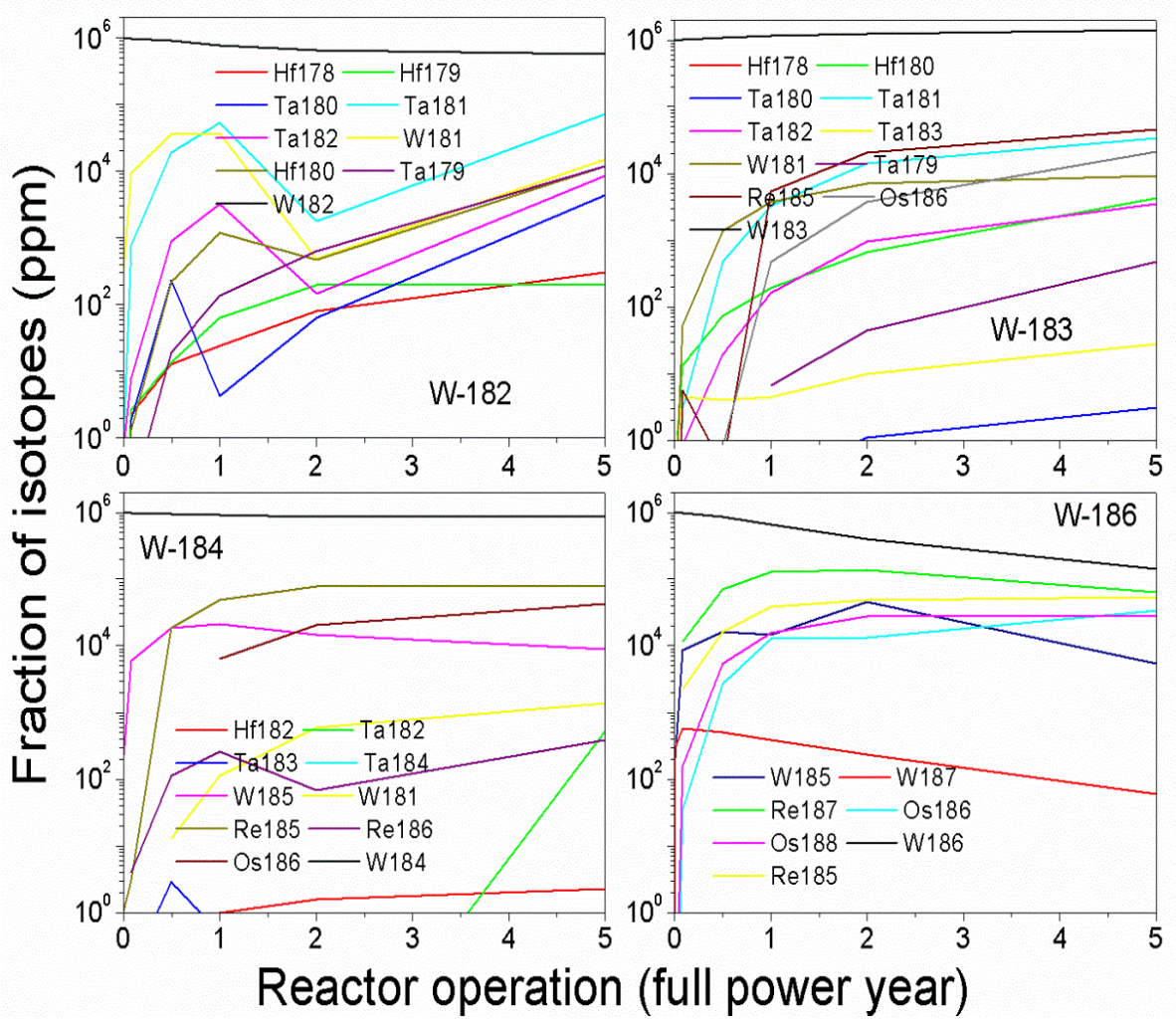

Fig 5.4 Time evolution of concentration of transmutated isotopes from major stable isotopes of tungsten

Similar to that of iron, the time evolution of the concentration of all the transmutated isotopes from stable isotopes of tungsten are studied. ^{181}Ta, ^{181}W, ^{180}Hf, ^{182}Ta, and ^{180}Ta are the major transmutated isotopes from ^{182}W. ^{185}Re, ^{181}Ta, ^{186}Os, ^{181}W are the major transmutated isotopes from ^{183}W. ^{185}Re, ^{186}Os, and ^{186}Re are the major transmutated isotopes from ^{184}W. ^{187}Re, ^{185}Re, ^{186}Re and ^{188}Os are the major transmutated isotopes from ^{186}W. The concentration of these major transmutated isotopes in natural tungsten after 5 FPY operation and their half-lives are given in Table 5.4.

Table 5.4 Important transmutated isoptopes from tungsten

Isotopes	Half-life (seconds)	% in tungsten after 5 FPY	Isotopes	Half-life (seconds)	% in tungsten after 5 FPY
^{177}Hf	Stable	0.020	^{181}W	1.05E+07	0.796
^{178}Hf	Stable	0.140	^{182}W	Stable	15.197
^{179}Hf	Stable	0.403	^{183}W	3.47E+24	19.970
^{180}Hf	Stable	1.411	^{184}W	1.26E+25	27.013
^{181}Hf	3.66E+06	0.010	^{185}W	6.49E+06	1.106
^{182}Hf	2.84E+14	0.004	^{186}W	1.86E+25	3.969
^{179}Ta	5.08E+07	0.092	^{187}W	8.59E+04	0.002
^{180}Ta	5.68E+22	0.279	^{183}Re	6.05E+06	0.008
^{181}Ta	Stable	4.063	^{184}Re	3.27E+06	0.109
^{182}Ta	9.91E+06	0.523	^{184m} Re	1.45E+07	0.077
^{183}Ta	4.40E+05	0.004	^{185}Re	Stable	8.314
^{180}W	Stable	0.486	^{186}Re	3.26E+05	0.127
^{188}Re	6.11E+04	0.002	^{187}Re	1.37E+18	1.841
^{185}Os	8.10E+06	0.243	^{188}Os	Stable	2.182
^{186}Os	6.31E+22	6.060	^{189}Os	Stable	0.624
^{187}Os	Stable	2.635	^{190}Os	Stable	1.124

5.3.2.3 Transmutation in chromium

Chromium has ^{50}Cr, ^{52}Cr, ^{53}Cr and ^{54}Cr stable isotopes with the isotopic abundance of 4.3%, 83.7%, 9.5% and 2.36%, respectively. Similar to that of iron and tungsten, the

study of transmutation and activation has been carried out in chromium for the 5 FPY. The time evolution of the concentration of transmutated isotopes from stable isotopes of chromium is presented in Fig. 5.5.

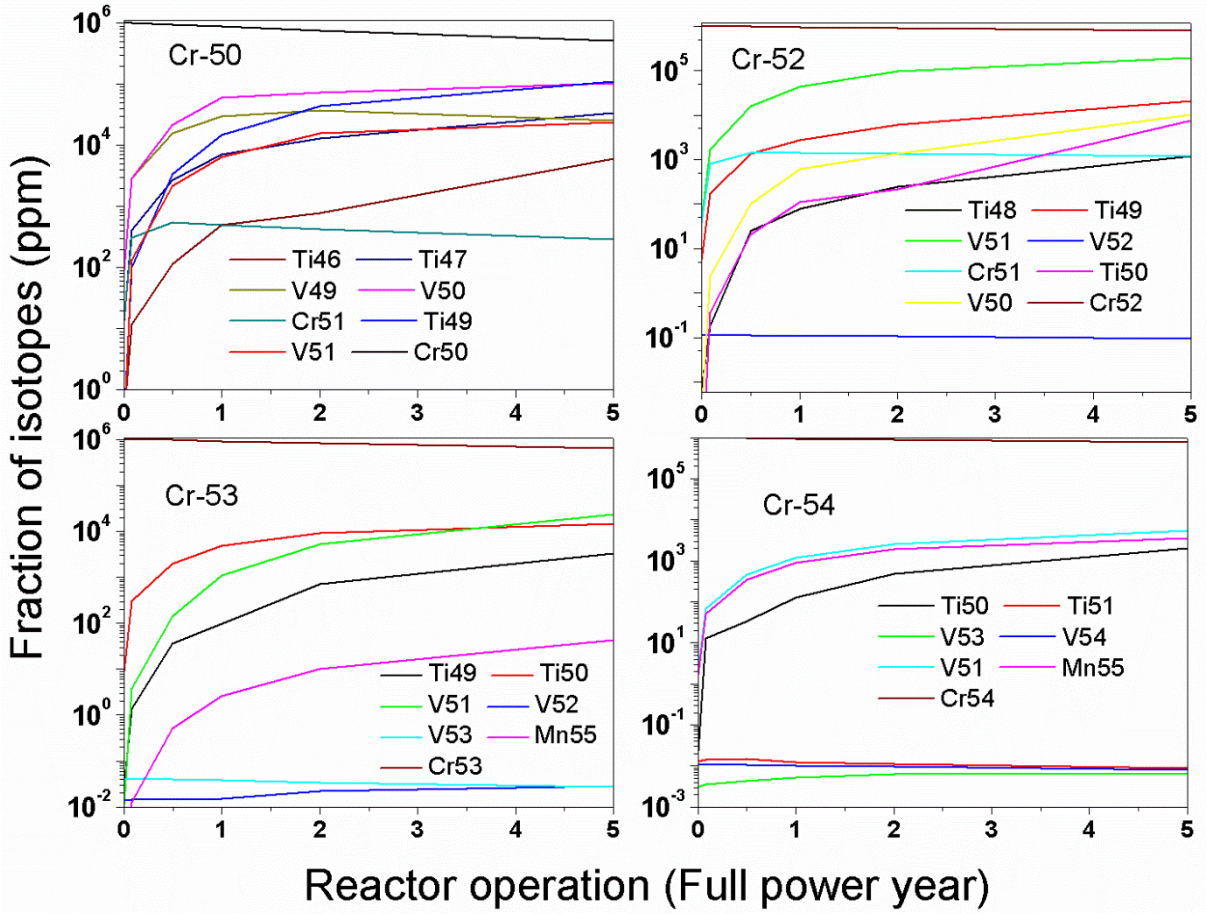

Fig. 5.5 Time evolution of concentration of transmutated isotopes from stable isotopes of chromium

These calculations have been carried out for the D-T neutron spectra at the first wall location of the EU DEMO [9]. ^{50}V, ^{47}Ti, ^{49}V, ^{49}Ti, ^{51}V are the major transmutated isotopes from ^{50}Cr. ^{51}V, ^{49}Ti, ^{50}V,^{50}Ti are the major transmutated isotopes from ^{52}Cr. ^{51}V, ^{50}Ti, ^{49}Ti, are the major transmutated isotopes from ^{52}Cr. ^{51}V, ^{55}Mn, ^{50}Ti are the major isotopes from chromium that are produced during the 5 FPY. The concentration

of these major transmutated isotopes in natural chromium and their half-lives are given in Table 5.5.

Table 5.5 Important transmutated isotopes from chromium

Isotopes	Half-life (seconds)	% in chromium after 5 FPY
^{46}Ti	Stable	0.032
^{47}Ti	Stable	0.148
^{48}Ti	Stable	0.568
^{49}Ti	Stable	2.037
^{50}Ti	Stable	0.641
^{49}V	2.85E+07	0.200
^{50}V	4.42E+24	2.508
^{51}V	Stable	16.310
^{50}Cr	5.68E+24	2.224
^{51}Cr	2.39E+06	0.100
^{52}Cr	Stable	66.989
^{53}Cr	Stable	6.257
^{54}Cr	Stable	1.791
^{55}Mn	Stable	0.008

One important observation from this transmutation study in chromium is that it mostly produces stable isotopes. Radioactive isotopes produced in chromium are comparatively lower than that of iron and tungsten.

It is noted form this calculation of transmutations that original isotopic composition of reactor elements gets changed during the reactor operation and radioactive isotopes are also produced. These transmutation impurities affect the materials' engineering properties drastically and their estimation is very important to predict the lifetime of reactor components.

5.4 Summary and conclusion

The study of transmutation reveals that chromium will produce a smaller number of radioactive isotopes in the D-T neutron spectrum of a fusion reactor as compared to iron and tungsten. It mostly produces stable isotopes in its burn up except for ^{49}V and ^{51}Cr having a half-life of 2.48E7 seconds and 2.3E6 seconds, respectively. After 5 full power year operation of EU DEMO, ^{55}Mn, ^{52}Cr and ^{53}Cr will have a concentration of 9.4%, 1.8% and 2.1%, respectively in iron. These isotopes will behave as impurities in iron and affect its microstructural and engineering properties. Mn shares some of its chemical and physical properties with iron but is more brittle and harder than iron. Similarly, chromium is also more brittle than iron and will be having a significant percentage in iron after the 5 FPY. These impurities alter the functional properties of iron and its alloys. Engineering properties such as tensile strength, thermal expansion, elasticity, etc. are needed to be quantified experimentally to understand the effects of these transmutation impurities of fusion reactor materials in D-T neutron irradiation. The transmutation studies in tungsten reveal that the concentration of ^{186}W decreases drastically and drops to 3.9% after 5 FPY. The concentration of isotopes of rhenium (Re) and osmium (Os) also increases significantly. In chromium, the concentration of ^{52}Cr decreases to 66.9 % and concentrations of ^{49}Ti, ^{50,51}V become significant.

CHAPTER: 6 DISPLACEMENT DAMAGE IN IRON, TUNGSTEN AND CHROMIUM

6.1 Introduction

Materials in fusion reactors have to endure high neutron flux of up to 14.1 MeV energy. These fusion neutrons produce different species of recoils in the reactor materials based on different reaction channels e.g. (n,n'), (n,2n), (n,α), (n,p) and (n,γ), etc. If the energy of recoil nuclei is more than the threshold displacement damage energy of target material, recoil atoms are displaced from its origin and act as primary knocked on atom (PKA). This PKA will further interact with the other atoms of the target material and transfers a fraction of its energy to other atoms. This results in the production of other knocked on atoms and damage cascade. This damage cascade of displacement damage has four stages namely; 1) collisional stage, 2) thermal spike, 3) quenching, and 4) annealing. In the collisional stage, the energetic recoil initiates the displacement collisions and continues until the energy of all the atoms involved in the cascades decreases to less than that of the displacement threshold energy of target. At the end of this stage, the number of displaced atoms reaches its maximum values. This stage lasts up to 5 ps depending on the damage energy of recoil. In the thermal spike stage, the remaining energy of knocked on atoms after the collisional stage is shared with the neighbouring atoms in the solid. In the third stage of quenching, the thermodynamic equilibrium of all the atoms is attained. This stage may take up to several ps and at the end of this stage, surviving or stable defects are formed. During this stage, the interstitials and vacancies recombine with each other, thus decreasing the numbers of Frenkel pairs until the saturated values of Frenkel pairs are attained. The fourth and last stage of annealing includes rearrangement and interaction of stable defects between

themselves and atoms of the target. It lasts from nanoseconds to month. The interactions between these energetic recoil atoms or primary knocked on atoms (PKA) and target atoms are complex many body processes that lead to the production of interstitials and vacancies in the target, both collectively known as the Frenkel pairs. At the time of initiation of damage cascade, a large number of Frenkel pairs are yielded due to dynamics of PKA but during the relaxation of collision cascade in the quenching stage, some of the displaced atoms tend to return to equilibrium crystal lattice positions. This effect results in the self-mitigation and recombination of interstitials and vacancies. The surviving Frenkel pairs are formed at the end of damage cascade. These surviving Frenkel pairs or point defects induce segregation, embrittlement, hardening, irradiation creep and swelling in the reactor materials thus affecting their engineering properties. Point defects and clusters increase the hardness of reactor materials which leads to the embrittlement [98] [99]. Earlier studies reveals that the ductility reduces from 20-30% to < 1% in Austenite SS at 4 dpa [98] [99]. Fracture toughness of structural material e.g., SS also drops rapidly with increasing point defects and drops to 50 $M.Pa.m^{-2}$ at 10 dpa from 100 $M.Pa.m^{-2}$ [100], [101]. Creep is also accelerated with the increasing void formation due to the accumulation of vacancies. All these studies confirm that the displacement of atoms has adverse effects on the microstructure and engineering properties of reactor materials and is the first step to estimate the radiation induced damages in the reactor materials.

The prediction of displacement per atom (dpa) is required to accurately predict the lifetime, and change in microstructural and engineering properties of reactor materials. Accurate values of dpa are also important in the field of the accelerated driven subcritical systems (ADSS) and ion irradiation on nanofilms. The dpa is calculated with

the displacement damage cross section which is the probability of producing displacements through neutron induced reactions. Displacement damage cross section and dpa are calculated as;

$$\sigma_{dpa}(E_n)_i = \int_{Ed}^{Tmax} \left(\frac{d\sigma}{dE}\right)_I \upsilon(T)_I \, dT \tag{6.1}$$

$$dpa/sec = \int_0^{En} \sigma_{dpa}(E_n).\Phi_n \, dE \tag{6.2}$$

where $\left(\frac{d\sigma}{dE}\right)_i$ is the Rutherford scattering cross section of a projectile of energy En to transfer of T energy to the recoil atom, $\upsilon(T)_i$ is the number of Frenkel pairs, E_n is the energy of incident neutron, E_d is the threshold displacement damage energy of target material, T_{max} is the maximum energy of recoil and Φ_n is the neutron flux on the target material. It is noted from Equation 6.1 that accurate prediction of displacement damage cross section requires accurate energy spectra of recoil and accurate damage matrices. The energy spectra of recoils from all open reaction channels can be calculated with the TALYS-1.8 [18] and Empire-3.2 [33] codes. In the previous chapters of this thesis, the appropriate nuclear models are optimized to calculate the best fitted nuclear data for stable isotopes of iron, tungsten, and chromium. The nuclear data obtained with these nuclear models compares very well with the experimental data from the EXFOR data library. The energy spectra of recoils are calculated with these optimized nuclear models and are explained in chapter 4. The damage matrices or the number of Frenkel pairs can be quantified with Norgett, Robinson and Torrens (NRT) [23], binary collisional approximation (BCA) [24], athermal recombination corrected-dpa (Arc-dpa) [25] and molecular dynamics (MD) simulations [67] methods. The NRT model does not include many body interactions and interactions of interstitials and vacancies in its

approach, thus it overestimates the actual number of defects. Despite the overestimation of defects, it is still an optimizing method of material selection in ITER and other fusion reactors due to its fast and straight forward approach. DART [24] and SRIM [102] are BCA based codes that can be used to predict the number of Frenkel pairs. DART code numerically solves the Lindhard equations for polyatomic materials while SRIM code solves the same using the Monte Carlo method. DART and SRIM codes do not include thermal recombination effects in their approach thus predict overestimated values of displacement damage similar to the NRT approach. Both of these models, NRT and BCA do not explain the time evolution of defects. The MD simulations include many body interactions in its approach and can explain the time evolution of defects, thus is considered as one of the most accurate methods to predict the number of displacements based on the realistic interatomic potentials and boundary conditions. Nordlund et al modified the NRT approach and introduced the athermal recombination corrected-dpa (arc-dpa) method [25]. In the Arc-dpa method, defect generation efficiency term is additionally included in the NRT approach to account for recombination of the interstitials and vacancies. The constant parameters of defect generation efficiency are either calibrated with the MD simulations or with the experimental damage data. As the Arc-dpa method is based on the results of MD simulations, it predicts real values of dpa. Previously, the MD simulations of damage cascade in tungsten were carried out by Warrier et al [68], Fikar et al [26] and Nordlund et al [25]. Stoller et al [103] had carried out the MD simulations in iron to quantify the number of Frenkel pairs but they did not include the energy loss of PKA in electronic excitations and stopping. As per the explored literature, the MD simulation of damage cascade were not carried out for pure chromium.

In this thesis, the MD simulations of damage cascade at up to 200 keV damage energies of PKA in iron, tungsten, and chromium are carried out using the LAMMPS code [104]. Later these results of MD simulations are used to calibrate the constant parameters of the Arc-dpa method. The neutron induced displacement damage cross section of iron, tungsten, and chromium are calculated with the NRT and Arc-dpa method. This calculated displacement damage cross section is used to predict the values of dpa in iron, tungsten, and chromium for different fusion reactor environments. The MD simulations, NRT and arc-dpa methods are briefly explained in next section.

6.2 Methodology to predict displacement damage

6.2.1 Molecular dynamics simulations

The Molecular dynamics simulations are the computational approach to model perturbations in the atomic systems caused by the energetic recoils. The MD simulations provide a realistic description of displacement damage. In the MD simulations, radiation damage is simulated using the appropriate interatomic potentials and boundary conditions. The position of all the atoms in the solid lattice is identified at different stages of cascade development. In the present work, the MD simulations are carried out with the LAMMPS code [104]. The MD simulations have some limitations e.g. 1) they require huge computation cost and time, 2) they require the interatomic potentials for the interactions between target atoms and recoil atoms, 3) they can simulate only up to nano second-order time and sample size is also limited. It includes many body interactions and can provide insight into the time evolution as well as the spatial distribution of interstitials and vacancies. In the present work, damage cascades

are simulated for damage energy of up to 200 keV of self PKA in tungsten, iron, and chromium.

The interatomic potentials of tungsten are adopted from Warrier et al. [69]. They were previously used by Warrier et al. in the simulation of damage cascade in tungsten at up to 5 keV damage energy of PKA. Warrier et al [69] stiffened the potentials of Zhou et al [105] with a short-range Ziegler- Biersack-Littmark (ZBL) potential at interatomic separations of less than 1.2 Angstroms. The interatomic potentials of Zhou et al. were embedded atom method (EAM)/alloy type. The lattice parameter, cohesive energy, and vacancy formation energy, reproduced by the Warrier et al., are 3.12 angstrom, 8.75 eV/atom and 3.56 eV, respectively [69].

The interatomic potentials of iron are adopted from Malerba et al [106]. These potentials of Malerba et al [106] are a Mendelev-type potential and point defects energies are calculated with density functional theory (DFT). These potentials are smoothened with Biersack–Ziegler potentials at short distances using the exponential function. The lattice parameter, cohesive energy and vacancy formation energy, reproduced with these interatomic potentials, are 2.86 angstroms, 4.122 eV/atom, 2.10 eV, respectively [106]. These values are within the acceptable limits of experimental data according to which lattice parameter, cohesive energy, and vacancy formation energies are 2.856 angstrom, 4.280 eV/atom, and 2.02-2.15 eV, respectively. The average threshold energy of iron, based on these potentials are 37.20±0.5 eV.

The interatomic potentials of chromium are taken from Howell et al [107]. These potentials are angular dependent potentials (ADP) type potentials and are fitted with the experimental values of a_0, E_0, B, elastic constants, vacancies formation energies, and

DFT surface energies for the (111) and (110) crystal orientations. Other input parameters were selected from the DFT database [107]. These fitting parameters had been optimized by minimizing the weighted mean square deviation of computed DFT properties using the simulated annealing method. Different sets of weight were selected and several versions of potentials were generated and tested against a set of experimental and the DFT calculations that were not included in the earlier fitting database. Based on the test results, final potentials are selected and it was concluded that the quadrupole term describing the potentials were sufficient [107]. These potentials are able to reproduce experimental and the DFT calculations [107]. Linear thermal expansion of chromium was calculated by the NPT Monte-Carlo simulations and included in these interatomic potentials. The results are in good agreement with the experimental data at up to 1200 Kelvin temperature [107]. Generally, thermal expansion is not included in the potentials fits thus stiffening of potentials is required to accurately predict the atomic interactions at the short distances. Due to the inclusion of thermal expansion in the potentials of Howells et al, these potentials are not needed to be stiffened. The MD simulations of damage cascade in chromium for the PKA of 1, 2, 10, 50, 100 and 200 keV damage energies are carried out to study the time evolution of Frenkel pairs and to predict the number of Frenkel pairs. MD simulations of displacement damage have been carried out for the first time for pure chromium.

The recoils of up to 200 keV damage energies are generated in the <100>, <010>, <001>, <112>, <120>, and <211> directions. In these simulations, the lattice is equilibrated at 500 K and periodic boundary conditions are adopted in these simulations so that no interstitial and vacancy would be lost at the boundaries of the target. These simulations are performed with the NVE ensemble. These simulations are carried out

at a time step of 0.001 picosecond and simulations are carried out at up to 30 picoseconds. The location of each atom is stored at every 0.1 picoseconds. Debye temperature of iron, tungsten, and chromium are 470 K, 400 K, and 424 K, respectively. In the present MD simulations, the energy loss of PKA in electronic excitation is calculated with the Lindhard-Scharff-Schiott theory [108] and two temperature method [109]. In the classical MD simulations, electronic stopping and excitations are not included in the damage cascade. Due to these electronic interactions, recoils lose a fraction of their energy in the electronic excitation and this fraction of energy does not contribute to the displacement damage. For iron and tungsten, damage energies of recoil atoms are calculated with LSS potentials [108]. In this approach, all the energy that is transferred to the electrons in electronic excitation and stopping are calculated in a single-shot. For chromium, these damage energies are calculated using the two-temperature method of MD simulations [109]. In the two-temperature model, a friction coefficient to account electronic stopping is included in the MD simulations. This friction coefficient becomes non-zero when atoms move faster than the electron stopping critical velocity. The time evolution of damage cascade in the MD simulations are described with the Langevin thermostat as:

$$m\frac{dv_i}{dt} = F_i(t) - \gamma_i v_i + f(t) \quad (6.3)$$

Here, v_i is the velocity of i^{th} atoms of mass m, F_i is the force subjected to other atoms and γ_i is the friction term. γ_i term represents the electron-ion interactions and electronic stopping and is calculated if an atom has energy more than the cut off energy. This cut off energy is equal to twice the cohesive energy. The magnitude of random force f(t) is

calculated by the local electronic temperature. The prediction of electronic temperature is described by the heat diffusion equations as:

$$C_e . \frac{\partial Te}{\partial t} = \Delta (k_e . \Delta T_e) - g_p(T_e - T_a) - g_s T_{a'} \quad (6.4)$$

Here, C_e is the electronic specific heat, k_e is the electronic thermal conductivity, T_e is the local electronic temperature, T_a is the effective atomic temperature and $T_{a'}$ has the dimension of temperature. $T_{a'}$ is equivalent to the kinetic energies of atoms if greater than the electronic threshold stopping power. The term $(g_p(T_e-T_a)-g_sT_{a'})$ represents the energy exchange between the target atoms via electron-ion interactions and electronic excitations. The constant terms g_p and g_s are calculated as:

$$g_p = \frac{3NK_b\gamma_p}{\Delta Vm} \quad (6.5)$$

$$g_s = \frac{3N'K_b\gamma_s}{\Delta Vm} \quad (6.6)$$

Here, N is the number of atoms in a simulation cell, ΔV is the volume of a simulation cell, N' is the number of atoms having energies higher than the threshold cut off energies, K_b is the Boltzmann constant and $\frac{\gamma s}{m}$ is the electronic stopping coefficient. $\frac{\gamma s}{m}$ is calculated with the data obtained from the SRIM/TRIM [102]. $\frac{\gamma p}{m}$ is approximated to be 9.09 ps^{-1} which is equivalent to electron-phonon coupling constant of chromium (12.2 X 10^{16} $W.m^{-3}.K^{-1}$). E_{cutoff} is taken to be the twice of the cohesive energy of chromium which is 4.10 eV/atom. The electronic stopping and excitation in MD simulations are incorporated using the TTM command of LAMMPS code [104]. The sample size of target and number of atoms in the sample have been given in Table 6.1.

Table. 6.1 Details of MD simulation of PKA cascades

Sample	Damage energy of PKA (keV)	Sample size (Angstrom)	Number of atoms in the sample
Tungsten (BCC) (Lattice constant= 3.16)	5	221.2*221.2*221.2	686000
	30	284.8*284.8*284.8	1458000
	50	316.5*316.5*316.5	2000000
	100	379.8*379.8*379.8	3456000
	200	474.7*474.7*474.7	6687324
Iron (BCC) (Lattice constant = 2.87)	5	199.3*199.3*199.3	686000
	30	256.9*256.9*256.9	1458000
	50	314.5*314.5*314.5	2000000
	100	344.4*344.4*344.4	3456000
	200	430.5*430.5*430.5	6687324
Chromium (BCC) (Lattice constant= 2.851 A)	1	199.57*199.57*199.57	686000
	2	199.57*199.57*199.57	686000
	10	256.59*256.59*256.59	1458000
	50	285.1*285.1*285.1	2000000
	100	342.12*342.12*342.12	3456000
	200	427.65*427.65*427.65	6687324

Visualization and identification of defects are carried out with the Ovito tool [110]. In the Ovito tool, Wigner-Seitz analysis is performed to simulate the time evolution of interstitials and vacancies. In the Wigner-Seitz analysis [111], trajectories of each atom

are checked in every Wigner-Seitz cell. If any Wigner-Seitz cell is vacant, it represents a vacancy and if any cell is occupied with more than one atom, it represents an interstitial. The numbers of Frenkel pairs after the generation of PKA are identified at every 0.1 picoseconds to up to 30 picoseconds. The results from the MD simulations and Wigner-Seitz analysis are explained in the results and discussion section. The standard error has been also assessed for these MD simulations using the block averaging method of MD simulation [112][113].

6.2.2 NRT and Arc-dpa method

Energetic recoils or PKA of energy E_{pka} lose their energy via electronic excitations and via collision with atoms. Damage energy (T_{dam}) which is the energy available to cause displacement damage (E_{pka} -$E_{electronic\ losses}$) is calculated with the Lindhard-Scharff-Schiott functions [108];

$$T_{dam} = \frac{E_{pka}}{1+k_{LSS}\,(g(\varepsilon))} \tag{6.7}$$

where k_{LSS} is the constant parameter which represents the Thomas-Fermi description of atomic interactions between recoil and target atom, and $g(\varepsilon)$ is the universal function. For a recoil of atomic mass and atomic number A_R and Z_R, respectively, and a target of atomic mass and atomic number A_L and Z_L, respectively, k_{LSS} is calculated as:

$$k_{LSS} = \frac{0.079 Z_R^{2/3} Z_L^{1/2} (A_R+A_L)^{3/2}}{(Z_R^{2/3}+Z_L^{2/3})^{3/4} A_R^{3/2} A_L^{3/2}} \tag{6.8}$$

$g(\varepsilon)$ is calculated based on the numerical approximation [23] as:

$$g(\varepsilon) = (3.4008\varepsilon^{1/6}+0.40244\varepsilon^{3/4}+\varepsilon) \tag{6.9}$$

$$\varepsilon = \frac{E_{pka}}{30.724 Z_R Z_L (Z_R^{2/3}+Z_L^{2/3})^{1/2}} \frac{A_L}{(A_R+A_L)} \quad (6.10)$$

Norgett, Robinson and Torrens (NRT) modified the Kinchin-Pease formula to predict the number of Frenkel pairs ($\upsilon(E_{pka})$) produced by a PKA of E_{pka} energy and target of having displacement damage energy, E_d as:

$$\upsilon(T)_{i=} k_{displacement} \frac{T_{dam}(Epka)}{2E_d} \quad (6.11)$$

where, displacement efficiency, $k_{displacement}$ is independent of the mass of the PKA, target, and energy of the PKA. It was simulated using the binary collision simulations of energetic ions in the target. These simulations predicted $k_{displacement}$ to be 0.8 as the 20 % of the atomic locations that were vacated due to ion interaction with the target atoms, were refilled with another knocked on atoms even in random binary collision sequence [23]. The NRT model does not include the many body interaction and interaction between interstitials and vacancies in its approach, thus athermal recombination corrected-dpa (Arc-dpa) approach were proposed by Nordlund et al [25] to predict the number of Frenkel pair more precisely by modifying the NRT formulation as:

$$\upsilon(T)=\frac{0.8}{2Ed}. T_{dam}. \varepsilon_{arc\text{-}dpa} \quad (6.8)$$

$$\varepsilon_{arc\text{-}dpa}= \frac{1-C_{arc\text{-}dpa}}{(2Ed/0.8)^{b_{arc-dpa}}} T_{Dam}^{b_{arc\text{-}dpa}}+C_{arc\text{-}dpa} \quad (6.9)$$

Where, $\upsilon(T)$ is the number of Frenkel pairs, $\varepsilon_{arc\text{-}dpa}$ is the defect generation efficiency, and $C_{arc\text{-}dpa}$ and $b_{arc\text{-}dpa}$ are the constant parameters of arc-dpa method. Constants $C_{arc\text{-}dpa}$ and $b_{arc\text{-}dpa}$ are either calculated with the fitting of the experimental data or fitting with the data from molecular dynamics simulations. In the present work, these constant

parameters are calibrated with results of the MD simulations in iron, tungsten, and chromium. T_{dam} is the damage energy of the PKA and is calculated with LSS functions (Eq. 6.7). The details of the constant parameters of arc-dpa method and their values are given in the upcoming sections.

6.3 Methodology and calculation methods

In the present work, the study of displacement damage in iron, tungsten and chromium is carried out in the following steps;

1] The first step in calculating displacement damage cross sections is to select the appropriate nuclear models in the TALYS-1.8 code to calculate the energy spectra of recoils. The validation of nuclear models and calculation of recoil spectra have been explained in 3rd and 4th chapter of this thesis. The damages matrices from the calculated recoil spectra have been evaluated with the MD simulations, NRT method, and arc-dpa methods.

2] In the present work, Molecular dynamics simulations of damage cascade due to the PKA of up to 200 keV damage energies are carried out for tungsten, iron, and chromium. The MD simulations have been carried out in the <100>, <010>, <001>, <112>, <120>, and <211> directions. The constant parameters of the Arc-dpa method have been calibrated with the results of the MD simulations of displacement damage cascade. The number of Frenkel pairs predicted with the MD simulations and arc-dpa are compared with the results from NRT, and other arc-dpa models. The MD simulations have been carried out with the Large-scale Atomic/Molecular Massively Parallel Simulator (LAMMPS) code [104].

3] Based on the results of the MD simulations, displacement damage cross section of iron, tungsten, and chromium are calculated with the NRT and arc-dpa methods. The values of dpa in tungsten, iron, and chromium are predicted for the first wall neutron spectrum of ITER and EU DEMO reactor [9], [10].

6.4 Results and discussion

6.4.1 Molecular dynamics simulation of damage cascade

In the present work, the MD simulations of damage cascade are carried out with the LAMMPS code [104]. In the present MD simulations, a self recoil atom is generated within the solid lattice of iron, tungsten and chromium. The condition of periodic boundaries is applied so that no interstitial or vacancy would leave the system. In the present work, the damage cascades are simulated for up to 200 keV damage energy of self- recoil and its effect on the displacements of atoms have been recorded at the time interval of 0.1 picoseconds. In the MD simulations of tungsten, the energy loss of PKA in electronic excitations and stopping are calculated with the LSS potential functions. The damage cascade caused by the self recoil of 5 keV damage energy in tungsten is presented in Fig. 6.1 at different time stages. In Fig. 6.1, it is noted that the vacancies and interstitials are less in number in the beginning of the cascade (at 0.6 picoseconds after PKA initiation) but as the time increases, the number of Frenkel pairs increases and attains their maximum value at 1 picosecond. This yield of maximum numbers of Frenkel pair represents the collisional stage of damage cascade. After the collisional stage, the vacancies and interstitials tend to return to the equilibrium lattice positions and their number decreases as they occupy the interstitial and vacant sites in the lattice (near to 2 picoseconds for 5 keV PKA damage energy). Beyond this time, defects tend

to stabilize and their number further decrease to the minimum saturated value (close to 4 picoseconds). This stage represents the quenching stage of displacement cascade. The time evolution of Frenkel pairs for the tungsten target is presented in Fig. 6.2 to study the time dynamics of defects at different damage energies of PKA. It is noted from Fig. 6.2 that the number of Frenkel pairs attains their maximum values and after this, knocked-on atoms tend to attain the vacant and interstitial positions in the target thus their number decreases with the increasing time. These defects become stable at the end of damage cascade. The number of Frenkel pairs attains a saturated value at 2.5 ps, 5 ps, 6 ps, 9 ps, and 12 ps for the PKA of damage energies of 5 keV, 30 keV, 50 keV, 100 keV, and 200 keV, respectively and become surviving or stable defects.

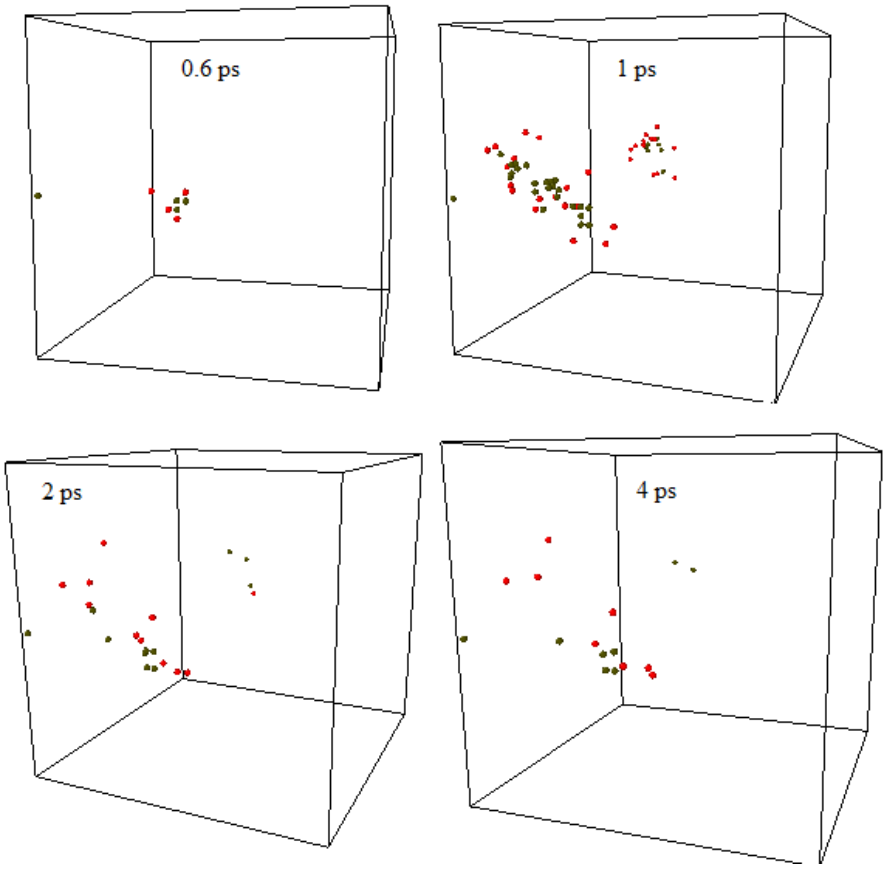

Fig. 6.1 Visualization of vacancies (red) and interstitials (black) in tungsten for 5 keV damage cascade at different times from PKA initiation

For iron, the PKA of the same damage energies are generated in the same directions and their effect on the location of other atoms are recorded. For the energies of 5 keV, 30 keV, and 50 keV, the number of Frenkel pairs attains a saturated value before 6 ps, but at higher PKA damage energies of 100 keV and 200 keV, the number of Frenkel pairs attains a saturated value near to 10 ps. The number of Frenkel pairs at different PKA damage energies as a function of time is presented in Fig. 6.3 for iron. In the MD simulations of iron, the energy loss of PKA in electronic excitations and stopping are calculated with the LSS potential functions.

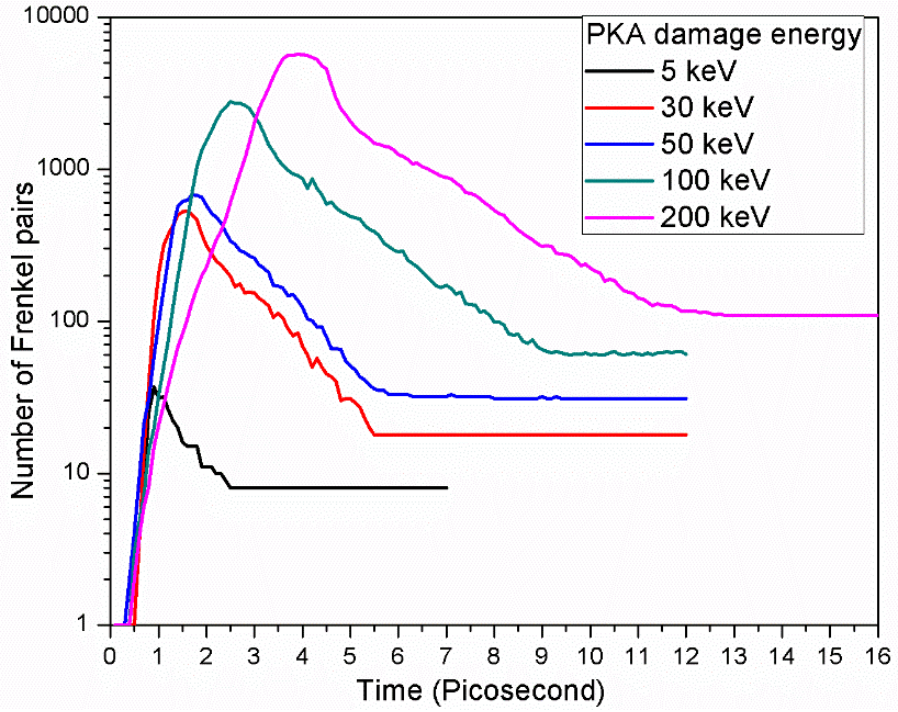

Fig. 6.2 Time evolution of Frenkel pairs for different recoils (PKA) energies in tungsten

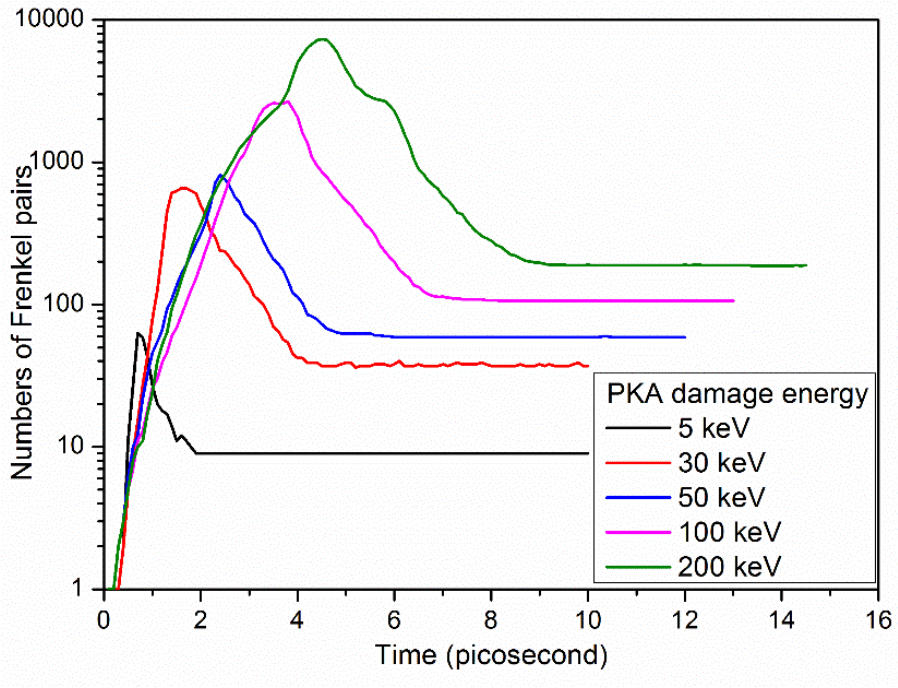

Fig. 6.3 Time evolution of Frenkel pairs for different recoils (PKA) energies in iron

Similarly, the time evolution of interstitials and vacancies for chromium have been studied at every 0.1 ps to 30 ps for recoils of different damage energies (1, 2, 10, 50, 100 and 200 keV) and presented in Fig. 6.4. The stable defects are formed at 3, 4, 5, 6, 11, and 18 ps after initiation of PKA of 1, 2, 10, 50, 100, and 200 keV damage energies, respectively. The time evolution of displacement damage is presented in Fig. 6.4 for chromium. The energy loss in the electronic excitation and stopping are calculated with the two-temperature model in these MD simulations. The two-temperature model is explained in Section 6.2.1.

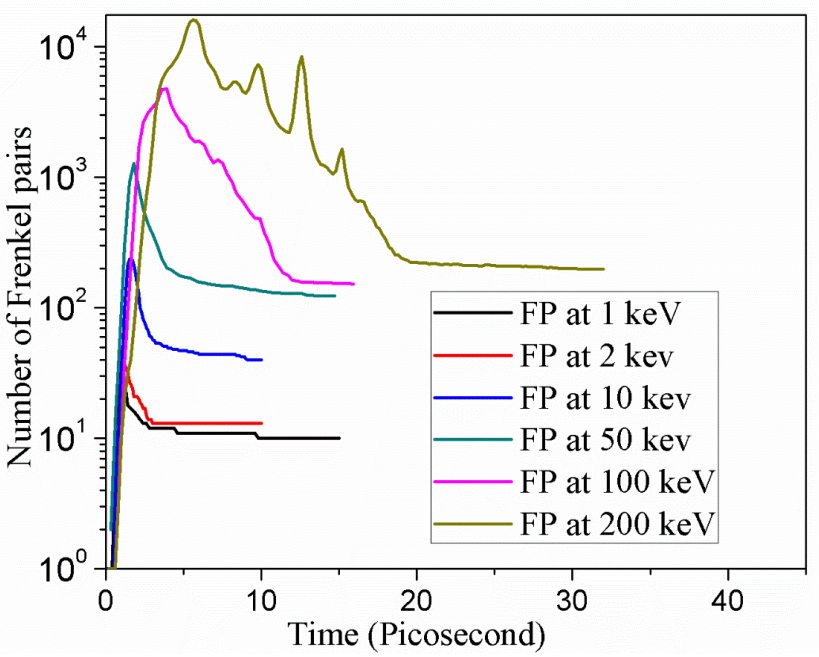

Fig. 6.4 Time evolution of Frenkel pairs for different recoils (PKA) energies in chromium

6.4.2 Error analysis of MD simulations

The standard error (SE) in these MD simulations have been simulated with the block averaging method of MD simulations [112], [113]. To estimate the SE in these MD simulations, the MD simulations are divided into the small blocks $(\Delta_{MD})_i$ of n intervals for all the 6 MD simulations of different directions. The mean of these blocks $\Delta_{(mean)i}$ is calculated at every time interval using all the 6 MD simulations of single incident energy. The average of Frenkel pairs, $\Delta_{(avg)i}$ for gradually increasing segments i=1, 2, 3.., n is calculated. Further, the standard deviation between the Δ_{mean} and $\Delta_{(avg)i}$ in subsequent blocks are calculated up to the n^{th} segment. This standard deviation becomes saturated at the end of damage cascade and represents the overall error of the MD simulations. The accuracy of the block average method depends on the block size and correlation time. The simulation blocks should remain independent of other blocks. This

condition requires total simulation time to be a large multiple of correlation time. In the present analysis, the block sizes are of 0.1 picoseconds and total simulation time comes out to be ≈200-300 times of correlation time. This condition ensures that the results are within the acceptable range [112], [113].

Table 6.2: Values of damage energies of the PKA, FP and SE of MD simulations for Fe, W and Cr

For tungsten			**For iron**			**For chromium**		
Energy	FP	SE	Energy	FP	SE	Energy	FP	SE
5 keV	8	0.94	5 keV	9	0.88	1	10	1.1
30 keV	18	1.87	30 keV	37	3.64	2	13	1.3
50 keV	31	3.08	50 keV	59	5.31	10	40	3.9
100 keV	61	5.5	100 keV	106	9.1	50	124	17.7
200 keV	109	9.14	200 keV	188	15.71	100	152	20.2
-	-	-	-	-	-	200	192	21.5

These results of MD simulations are used to calibrate the constant parameters ($b_{arc\text{-}dpa}$ and $C_{arc\text{-}dpa}$) of arc-dpa method and explained in the next section.

6.4.3 Calibration of constant parameters of arc-dpa method and estimation of Frenkel pairs with NRT and arc-dpa approach

Based on the performed MD simulation of self PKA species in iron, tungsten and chromium, constant parameter ($b_{arc\text{-}dpa}$ and $C_{arc\text{-}dpa}$) of the Arc-dpa method are calibrated and later used to calculate the damage matrices or the number of Frenkel pairs from all other recoil species in iron, chromium and tungsten. The results from the MD

simulations, NRT and Arc-dpa method have been presented in Fig. 6.5, 6.6 and 6.7 for tungsten, iron, and chromium, respectively. For the low energy recoils (<100 eV), the NRT and MD simulations predict a similar number of Frenkel pairs. As the energy of the PKA increases, the NRT model begins to deviate from the MD simulations and predicts values higher than the MD simulations. This overestimation of Frenkel pairs is due to the exclusion of thermal recombination effect in the NRT approach. The constant parameters that are used in the Arc-dpa calculations are given in Table 6.3.

Table 6.3 Constant parameter of arc-dpa method

Parameter	Values	
	$b_{arc\text{-}dpa}$	$c_{arc\text{-}dpa}$
Iron	-0.586±0.01 [25]	0.31±0.09 [25]
	-0.71±0.01 (Derived from present MD simulations)	0.12±0.02 (Derived from present MD simulations)
Tungsten	-0.56±0.02 [25]	0.12±0.01 [25]
Chromium	-0.45±0.03 (Derived from present MD simulations)	0.12±0.01 (Derived from present MD simulations)

Based on the constant parameters given in Table 6.3, the number of Frenkel pairs, generated due to the energetic recoils are calculated with the Arc-dpa method. The results of the MD simulations of the damage cascade in tungsten carried out by Fikar et al [26] and Nordlund et al [25] are compared with the present MD simulations. Nordlund et al. [25] also calibrated the constant parameters of the Arc-dpa method and predict the Frenkel pairs. The Arc-dpa predictions of Nordlund et al. [25] compares well with present MD simulations for tungsten.

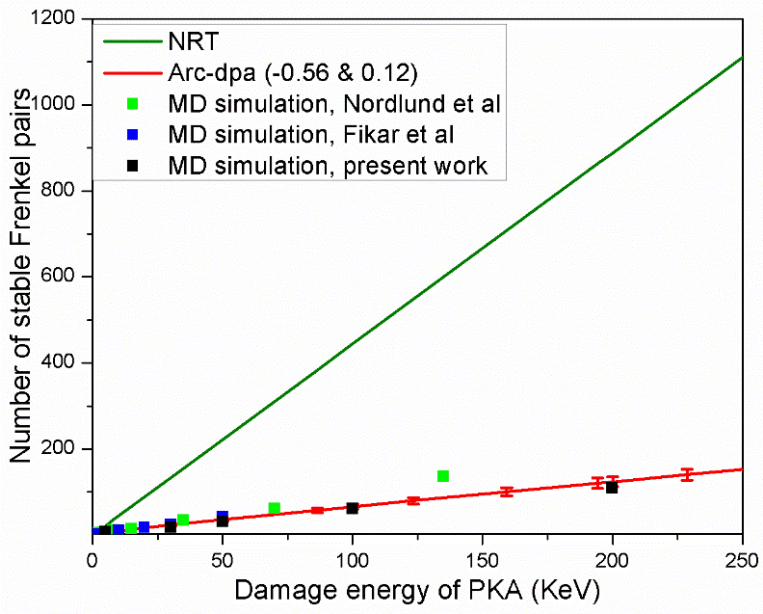

Fig. 6.5 The number of Frenkel pairs calculated with the MD simulation, NRT and arc-dpa approach for W PKA in W target

The MD simulations of damage cascade in iron are compared with the existing results of Stoller et al [70] and arc-dpa predictions of Nordlund et al. [25]. The number of Frenkel pairs calculated with the arc-dpa method using the constant parameters of Nordlund et al. [25] overestimates the present MD simulation results. Nordlund et al. calibrated the $b_{arc\text{-}dpa}$ and $C_{arc\text{-}dpa}$ with the MD simulations of Stoller et al. Stoller et al [70] [103] had simulated the damage cascade caused by the self PKA in the iron target using the MOLDY code [114]. Stoller et al. did not include the electronic losses of PKA in their approach thus had not calculated the damage energy in their model. Due to this, Stoller et al. predicted the overestimated values of Frenkel pairs. Nordlund et al. had calibrated the Arc-dpa parameters using the same MD data of Stoller et al., thus also overestimated the number of Frenkel pairs. In the present work, energy loss of PKA in the electronic excitation is calculated with the Lindhard-Scharff-Schiott (LSS) function

and included in the damage cascade. For iron, constant parameters are calibrated with the results of performed MD simulations.

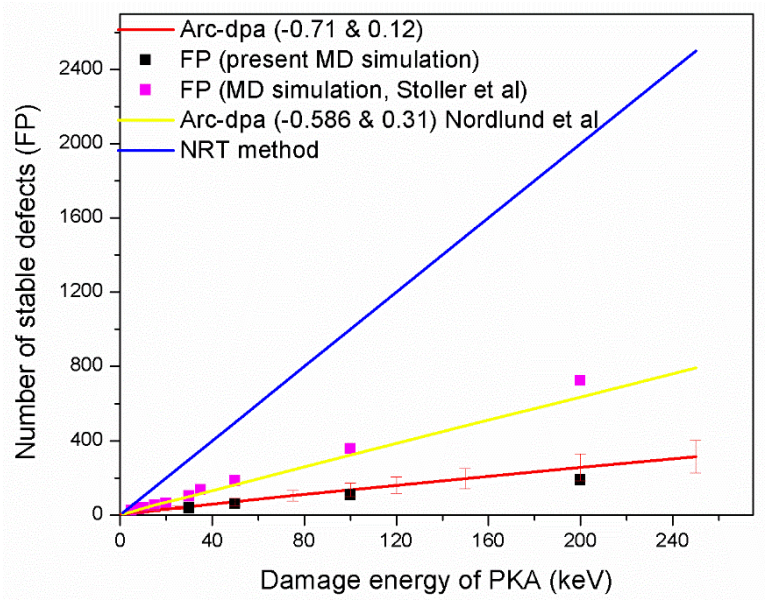

Fig. 6.6 The number of Frenkel pairs calculated with the MD simulation, NRT and arc-dpa approach for Fe PKA in Fe target lattice

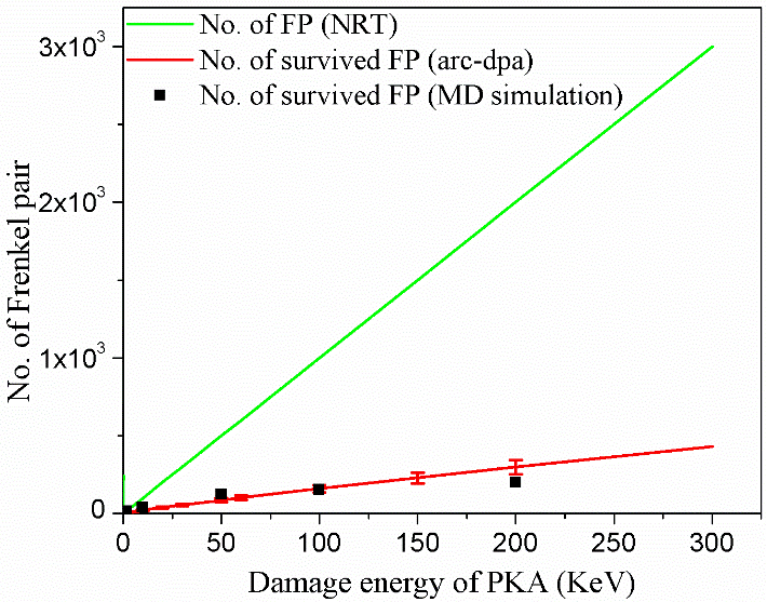

Fig. 6.7 The number of Frenkel pairs calculated with the MD simulation, NRT and arc-dpa methods for Cr PKA in chromium target

For chromium, these Arc-dpa parameters are calibrated with the performed MD simulation results. The number of Frenkel pairs obtained with the Arc-dpa, NRT and MD simulations are compared and presented in Fig. 6.7. The number of Frenkel pairs produced due to other recoil species is predicted using the calibrated constant parameters of the Arc-dpa method.

6.4.4 Displacement damage cross section of tungsten, iron, and chromium

In most of the previous studies of displacement damage, the displacement damage cross section (σ_{dpa}) was calculated with the NRT approach which always overestimates the displacement defects. The lifetime of reactor components, predicted with the NRT method, are always underestimated and this increases the maintenance of reactor components. In the present work, σ_{dpa} is calculated for all the stable isotopes of iron, tungsten, and chromium considering all the open reaction channels with the Arc-dpa and NRT methods. These σ_{dpa} of individual isotopes are used to predict the σ_{dpa} of natural iron, tungsten, and chromium using their respective isotopic abundances. σ_{dpa} of natural iron, tungsten, and chromium for neutron irradiation of up to 15 MeV energy are calculated and presented in Fig. 6.8-6.10. It is noted from the displacement damage cross section of iron that displacement damage cross section with the Arc-dpa approach are seven times less than the NRT approach. The displacement damage cross section of iron increases beyond 10 MeV due to the contributions of (n,2n) and (n,np) reaction channels as their threshold energies are 11.3 MeV and 10.303 MeV, respectively in ^{56}Fe. σ_{dpa} of tungsten obtained by the Arc-dpa method are six higher than the arc-dpa approach. It is noted from the calculation of displacement damage cross section of chromium that beyond 12 MeV, it increases sharply. It is due to the contribution of the (n,np) and (n,2n) reaction channels in ^{52}Cr. The threshold energies for these reaction

channels in ^{52}Cr are 10.7 and 12.23 MeV, respectively. These displacement damage cross section of iron, tungsten, and chromium are later used to predict the number of dpa in iron, tungsten, and chromium for typical fusion reactor neutron spectrum and explained in the next section.

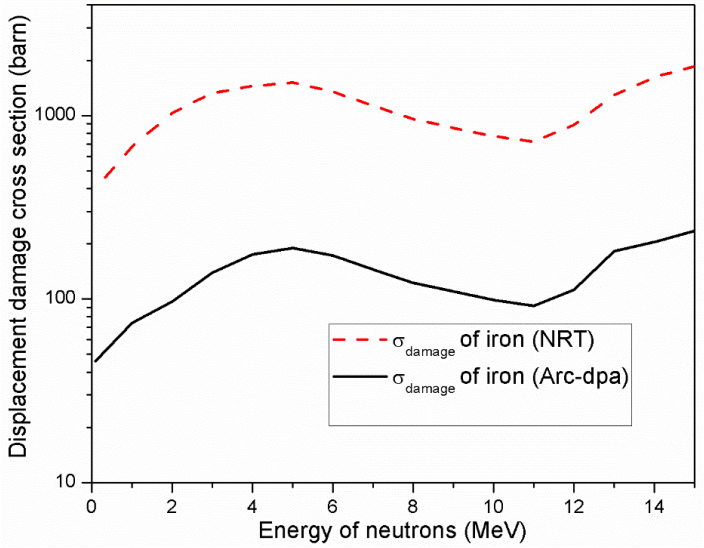

Fig. 6.8 Displacement damage cross section of natural iron with the NRT and arc-dpa methods for neutron irradiation of up to 15 MeV energy

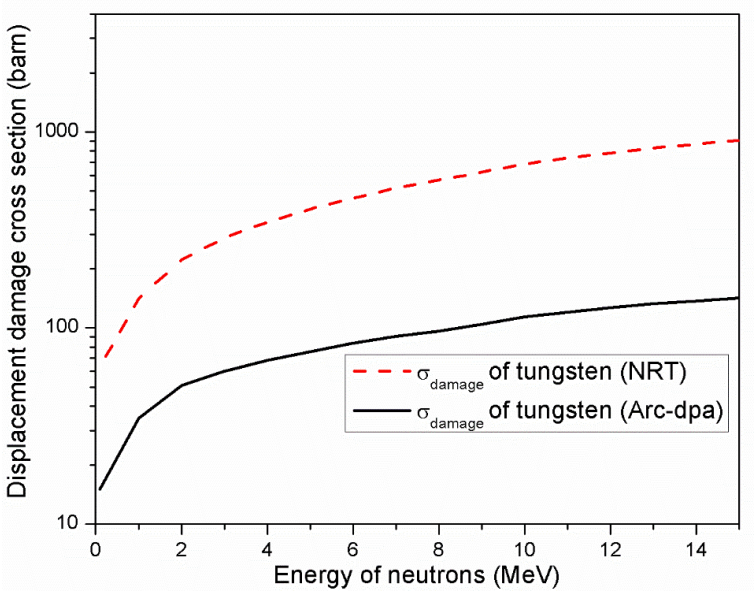

Fig. 6.9 Displacement damage cross section of natural tungsten with the NRT and arc-dpa methods for neutron irradiation of up to 15 MeV energy

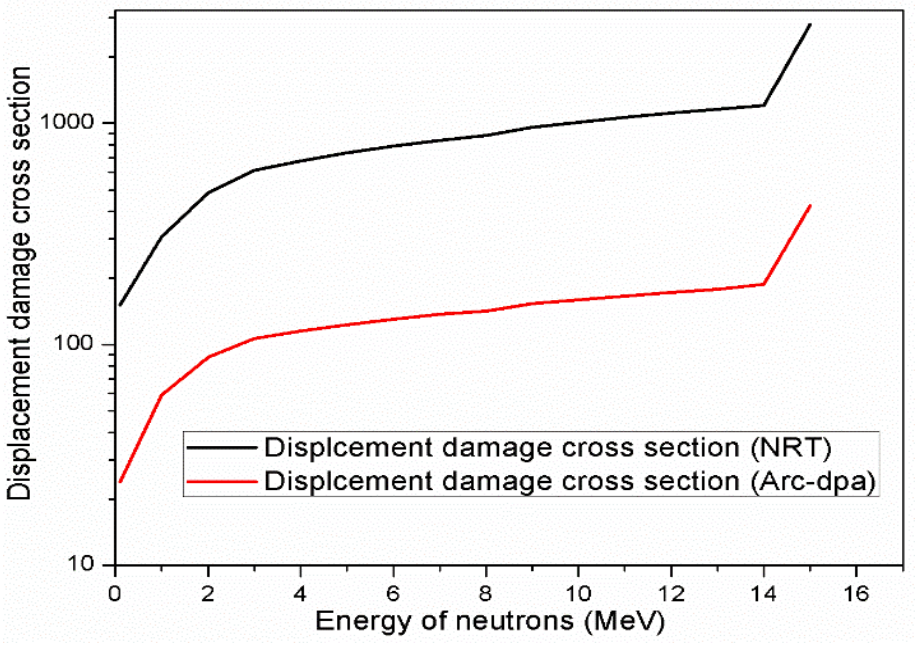

Fig. 6.10 Displacement damage cross section of natural chromium with the NRT and arc-dpa methods for neutron irradiation of up to 15 MeV energy

6.4.5 dpa values in tungsten, iron, and chromium for fusion reactor environment

The values of dpa in iron, tungsten and chromium which are the key parameter in defining their lifetime in fusion reactors, are calculated for the neutron spectra at the first wall armour of ITER [10] and EU DEMO [9], and at the first wall of EU DEMO [10]. Neutron spectra at these locations are also given in Fig. 6.11-6.13. These neutron spectra were calculated by Gilbert et al [9] [10] using the MCNP code. Gilbert et al [9] had calculated the neutron spectrum at different locations of EU DEMO having the source strength of ≈3.5 X 10^{20} neutrons sec^{-1} per GW thermal power. As per the conceptual design of the EU DEMO, it produces the 1.6 GW thermal fusion power (≈5.6 X 10^{20} neutrons.sec^{-1}). Similarly, neutron spectra at the first wall of ITER were calculated for 500 MW thermal fusion power having the source strength of 1.77 X 10^{20} neutrons.sec^{-1} [12].

The dpa values per full power year (FPY) in iron are predicted and presented in Fig. 6.11. In iron, the values of $dpa_{Arc\text{-}dpa}$/FPY are 8.24, 3.2 and 1.19 at the armour location of the first wall of EU DEMO and ITER, and at the first wall location of EU DEMO, respectively. The dpa values, predicted by The NRT model, are 52.6 dpa (NRT)/FPY, 19.3 dpa (NRT)/FPY and 7.59 dpa (NRT)/FPY at the same locations. Gilbert et al [22] predicted dpa_{NRT} values to be 9.2/FPY at the first wall location of EU DEMO using the nuclear data from the TENDL-2017 data library. As per the present calculation, dpa_{NRT} comes out to be 7.59/FPY at the same first wall location of EU DEMO. The reason for this discrepancy is the usage of different data by Gilbert et al. Gilbert et al had obtained nuclear data from TENDL-17 data library.

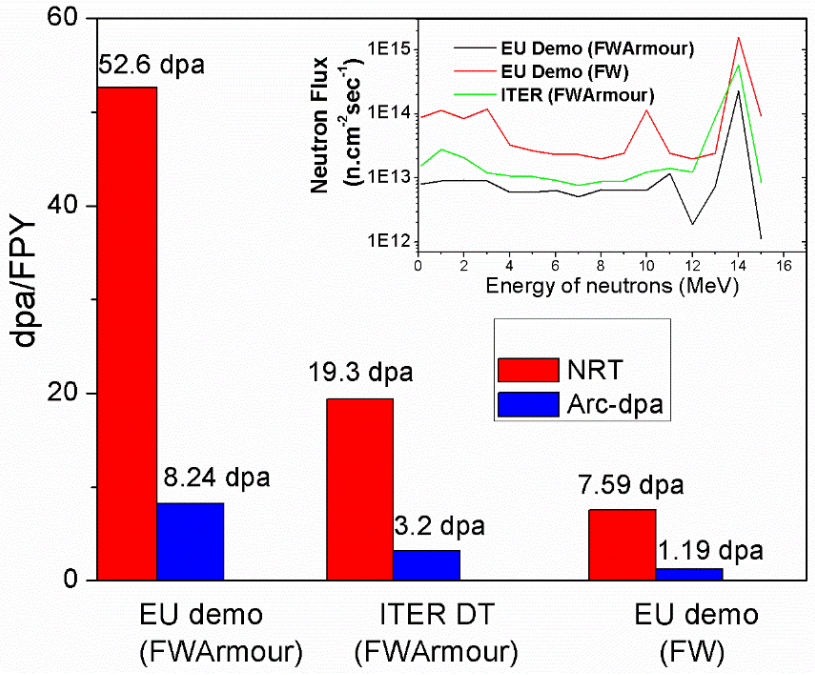

Fig. 6.11 Values of dpa in iron for the neutron spectrum at the first wall armour location of ITER and EU DEMO and at the first wall location of EU DEMO fusion reactor

The dpa values in tungsten are calculated at the first wall armour location of ITER and EU DEMO, and the first wall location of EU DEMO and presented in Fig. 6.12. In tungsten, 5.37 dpa (Arc-dpa)/FPY, 2.15 dpa(arc-dpa/FPY) and 0.93 dpa(arc-dpa/FPY) are observed at the armour location of the first wall of EU DEMO and ITER, and at the first wall location of EU demo, respectively. These dpa values predicted by the NRT method, are 32.5 dpa (NRT)/FPY, 13.3 dpa (NRT)/FPY and 5.44 dpa (NRT)/FPY at the same locations. Gilbert et al [22] predicted dpa_{NRT} values to be 4.9 dpa/FPY at the first wall location of the EU DEMO using the nuclear data from the TENDL-2017 data library.

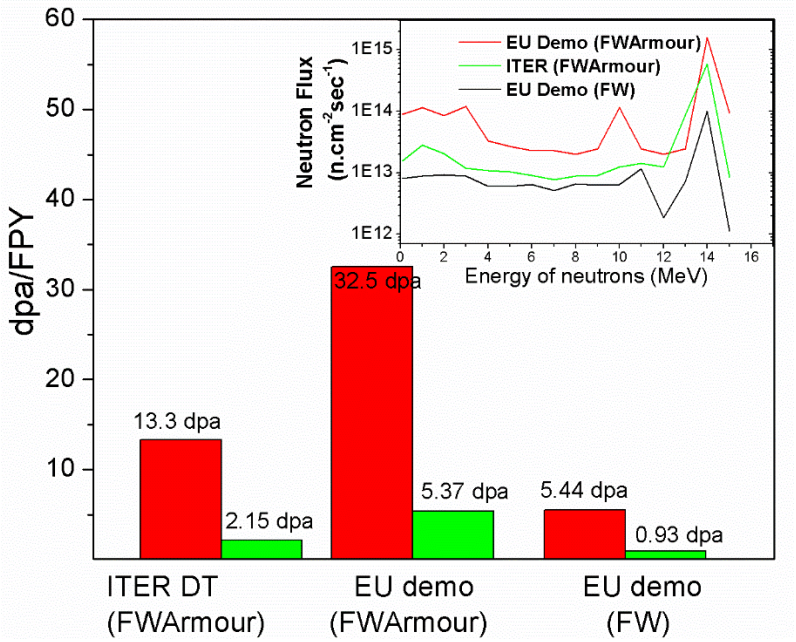

Fig. 6.12 Values of dpa in tungsten for the neutron spectrum at the armour location of first wall of ITER and EU DEMO and at the first wall location (FW) of EU DEMO fusion reactor

The dpa values in chromium have been calculated at the first wall armour location of ITER and EU DEMO, and at the first wall location of EU DEMO. This assessment of

the dpa is presented in Fig. 6.13. In chromium, 7.58 dpa (Arc-dpa)/FPY, 2.98 dpa(arc-dpa/FPY) and 1.13 dpa(arc-dpa/FPY) are observed at the armour location of the first wall of EU DEMO and ITER and at the first wall location of EU DEMO, respectively. The dpa values, predicted by the NRT model, are 47.8 dpa (NRT)/FPY, 19 dpa (NRT)/FPY and 7.1 dpa (NRT)/FPY at the same locations.

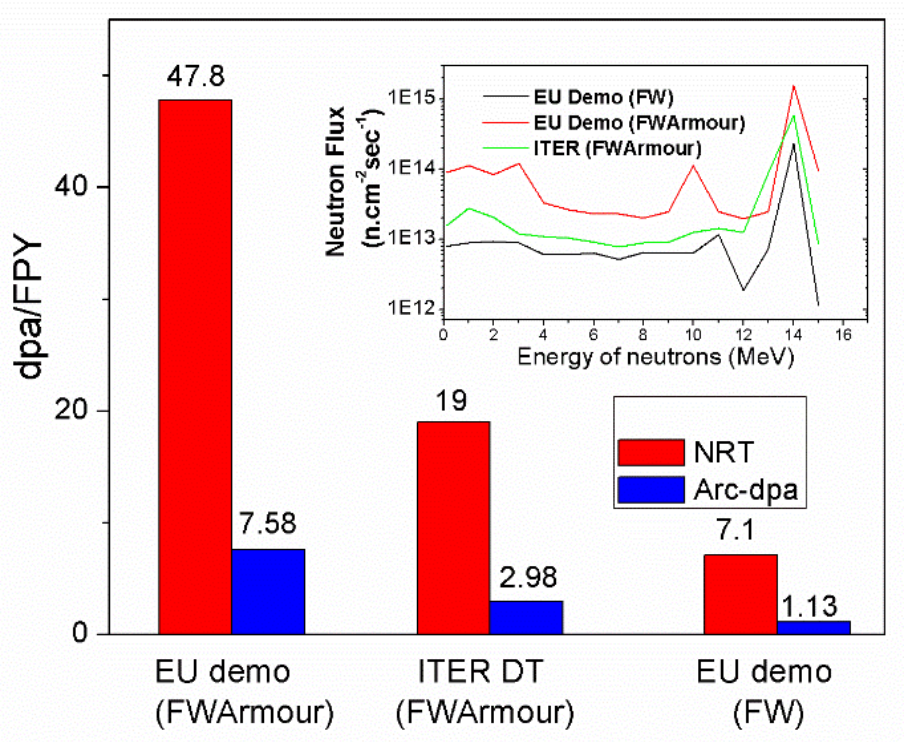

Fig 6.13 Values of dpa in chromium for the neutron spectrum at the armour location of first wall of ITER and EU demo and at the first wall location of EU DEMO fusion reactor

Out of these three materials, tungsten comes out to be more radiation-resistant due to low reaction rate of open reaction channels and having high displacement threshold energy compared to iron and chromium. Iron and chromium are not planned to be used at the armour location of the fusion reactors. They will be used at the first wall location of fusion reactors. The prediction of dpa in iron and chromium at the armour location

is carried out to predict their lifetime if they are to be used at that location for experimental purposes. It is noted from the above calculations that dpa values predicted by arc-dpa values come out to be six times lower than the NRT method. A similar approach can also be adopted to assess the displacement damage in other fusion reactor materials.

6.5 Summary

The energy spectra of recoils from the neutron induced reactions and quantification of Frenkel pairs by the energetic recoils are the two essential input parameters to evaluate the dpa in fusion reactor materials. In the present work, the energy spectra of recoils from all the open reaction channels for all the stable isotopes of tungsten (^{180}W, ^{182}W, ^{183}W, ^{184}W, & ^{186}W), iron (^{54}Fe, ^{56}Fe, ^{57}Fe, & ^{58}Fe) and chromium (^{50}Cr, ^{52}Cr, ^{53}Cr, & ^{54}Cr) have been predicted with the validated nuclear models using the TALYS-1.8 code. The quantification of Frenkel pairs produced by the energetic native recoils in iron, tungsten, and chromium for the damage energy of up to 200 keV have been carried out with the MD simulation using the LAMMPS code. The results of the MD simulations are used to calibrate the constant parameters of the Arc-dpa method and their predictions are compared with the NRT and other Arc-dpa models. The number of Frenkel pairs predicted with the Arc-dpa method using the constant parameters of Nordlund et al are in good agreement with the performed MD simulation for tungsten and overestimate the results of MD simulations for iron. For iron and chromium, the constant parameters have been fitted with the performed MD simulation results. Based on the results of the energy spectra and damage matrices from the Arc-dpa and NRT approaches, displacement damage cross section of iron, tungsten, and chromium are calculated. The dpa values in iron, tungsten, and chromium are predicted for neutron

spectrum at the first wall of the ITER machine and European DEMO fusion reactor. A similar assessment of dpa can also be carried out for other important fusion reactor materials.

CHAPTER: 7 ENERGY LOSS CORRECTION OF CHARGED PARTICLE USING MONTE CARLO APPROACH

7. 1 Introduction

The accurate energy differential cross section of outgoing charged particles from neutron-induced reactions on different materials are important in the area of nuclear reactions [35], fusion-based nuclear reactors [95] [38], and in the treatment of cancer with fast neutrons [115]. The neutron-induced reactions at higher energies can provide insight into the study of different modes of nuclear reactions namely, compound nuclear reaction, pre-equilibrium, and direct nuclear reactions. Grimes et [35] have studied the energy spectrum of charged particles to study the direct and pre-equilibrium reaction mechanisms. In the fusion reactor, most of the energy of DT reactions are shared by neutrons (14.1 MeV). These high energy neutrons interact with the surrounding materials and produce different charged particles species such as protons, deuterons and alpha particles. In the 1^{st} and 2^{nd} chapters, the importance of the EDX data of outgoing particles is provided. The EDX of outgoing charged particles is required to calculate the gas production, transmutation and also required to validate nuclear models for the further prediction of energy spectra of recoil. The EDX of charged particles are measured with the silicon surface barrier detector arranged in the telescopic manner [38]. The charged particles produced in neutron induced reactions at the target foils lose a fraction of their energy due to the elastic scattering with the atoms of target foils. Due to this energy loss in the target foil, charged particles are recorded with the decreased energy in the silicon surface barrier detector. These charged particles are sometimes absorbed in the target foil during their transport in the foil. To accurately predict the energy of the produced charged particles in nuclear reactions, it is essential to model

this loss of energy and particles in the target foil. There are methods developed earlier using the Fredholm equation [27]–[30][74] to predict the true energy spectrum of charged particles. In the present thesis, the Monte Carlo approach is used to identify the true spectrum of charged particles. The results for alpha particles and protons are compared with the results of earlier methods. The requirement of energy loss correction, details of previous methods and the proposed method are explained in the next section.

7.2. Need for energy loss correction in scattering experiments

The low reaction cross section of charged particle production reaction channels in neutron induced reactions and low intensity of neutrons on the target foils are the two major limitations in the measurement of the EDX data of charged particles. To counteract these two limitations, thick target samples are used to achieve the high yield of charged particles. Charged particles in neutron induced reactions are produced uniformly throughout the sample thickness. Charged particles which are produced inside the target foil interact with the atoms of target foil and lose a fraction of their energy while coming out of target foil. The phenomenon of energy loss is explained in Fig. 7.1. Charged particles are produced in the foil with the true energy (E_t) and lose fractions of their energy (ΔE) while transporting through the foil. Later these charged particles are measured with the measured energy (E_m), by the detector placed outside of the foil. If the energy of charged particle becomes zero within the foil, then it cannot escape the foil and is lost in the measured spectrum. This loss of energy and particles in the measured energy spectra of charged particles depends on the thickness of target foil. Thus, the measured energy spectrum is downgraded in the energy and particles and needs to be corrected for the loss of energy and loss of particles in the target foil to have the true energy spectrum of charged particles.

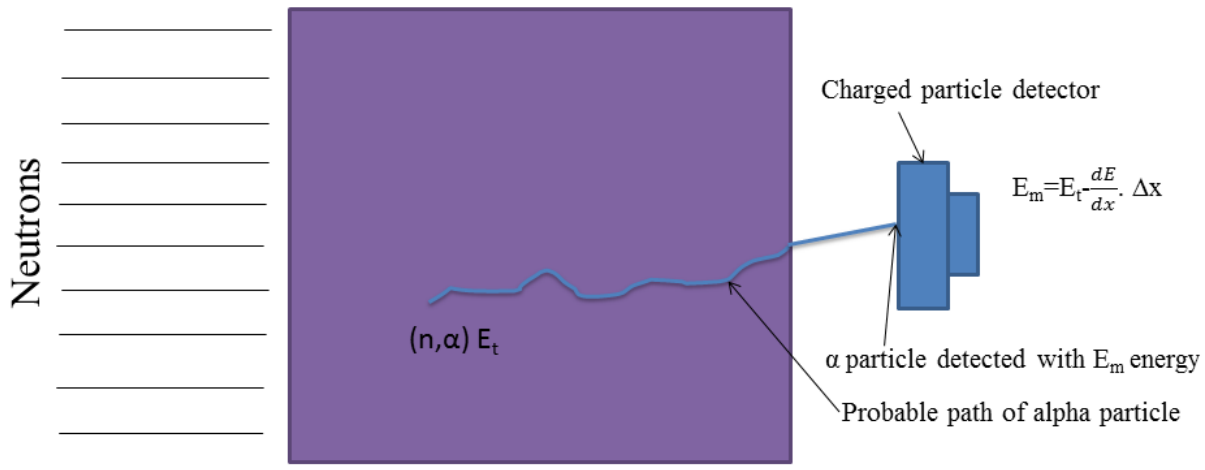

Fig. 7.1 Energy loss phenomenon of produced charged particles in the target foil, here $\frac{dE}{dX}$ is the stopping power of α particle and Δx is the total distance travel by α particle in the foil.

Previously, Johnson et al [74], Slypen et al [29], Rezentes et al [28], Soderberg et al [27] and Pomp et al [30] had solved this problem using the integration method of the Fredholm equation [73]. The reproduction of the true spectrum of charged particles had been treated with the general method of solving the Fredholm integral equation and is given below:

$$M(E) = \int_0^\infty R(E,E')\,T(E')dE' \tag{7.1}$$

Where M(E) is the measured energy spectrum of charged particles, R(E, E') is the response function of charged particles and T(E') is the true energy spectrum of charged particles. Johnson et al derived the following equation (Eq. 7.1) to reproduce the true spectrum:

$$\text{M(E)}=\frac{1}{\text{T'S(E)}}\int_E^{Em} X(U)dU \tag{7.2}$$

$$T' = T/\cos(\theta) \quad (7.3)$$

Where S(E) is the stopping power of charged particles at energy E, X(U) is the true energy spectrum, M(E) is the measured energy spectrum, U is the true energy, E is the measured energy, T is the thickness of foil and θ is the angle of detection. Johnson et al had calculated the stopping power data with Zeigler's formula [116] and didn't include successive interactions of charged particles with the target atoms. Johnson et al had solved the Fredholm equation in the matrix form as;

$$M=N.X+e \quad (7.4)$$

Where N is the $\frac{\Delta E}{T' S(E)}$, X is the true energy spectrum, and e is the error term. This eq. 7.4 had been solved using the Lagrange multiplier technique. Slypen et al had developed a code-named PERTEN to reproduce the true energy spectrum of charged particles. Slypen et al had reproduced true energy with the formula, $E_t=E_m+\Delta E$ where ΔE is the energy loss of the charged particles in the foil. Slypen et al had calculated the true energy spectrum in the following two steps; 1) Energy shift, ΔE was calculated and added to the measured energy to get the true energy. 2) If particles were lost in foil, correction of lost particles were also applied. Slypen et al had taken the energy loss data from Northcliffe et al [117].

Rezentez et al [28] had used the following equation (Eq. 7.5) to reproduce the true energy spectrum of charged particles;

$$M(E)= [d.\ S(E)]^{-1} \int_E^{Em} X(U)dU \quad (7.5)$$

Where, d is the thickness of the foil, S(E) is the alpha stopping power, X(U) is the true energy spectrum of charged particles, and E_m is the maximum energy of produced

charged particles in the foil. Rezentes et al had derived Eq. 7.5 as M=RT, where R refers to the matrix of the response function, M refers to the matrix of the measured spectrum and T refers to the matrix of true energy spectrum. Rezentes et al [28] reproduced the true energy spectrum as T=R'M where R' is the inverse of the response function matrix. Rezentes et al had calculated the R' with the Moore–Penrose generalized method. Soderberg et al [27] had also treated this problem with the Fredholm method using the upper triangular matrix form of the response function. Soderberg et al [27] had also considered the energy straggling in their calculations. Pomp et al [30] had used the inverse of response function to reproduce the true energy spectrum of charged particles using following Eq. 7.6;

$$T(E_t)=P(E_t).\sum_{j=0}^{j=i} R_{inv}(E_j,E'_J)m(E'_j) \quad (7.6)$$

Where $R_{inv}(E_i,E'_J)$ is the inverse matrix of the response function of measured energy E'_j and true energy E_j and $P(E_t)$ is the particle loss correction factor. Pomp et al had calculated R_{inv} using the iterative method.

These reported works had been carried out by solving the Fredholm equation. Out of these works, only Soderberg et al [27] had considered the multiple scattering of charged particles with the atoms of the target foil. Johnson et al, Slypen et al, Rezentes et al, and Pomp et al had solved this problem considering the single incident energy of charged particles as they had calculated the response function of charged particles based on their initial energy. Subsequent increase in the stopping power of charged particles as their energy decreases while passing through the target foil has not been accounted by Johnson et al, Slypen et al, Rezentes et al, and Pomp et al. In the present work, a Monte Carlo method, based on the transport of charged particles and successive interactions of

charged particles with the atoms of target foil has been developed. The proposed method has been explained and validated in the next sections.

7.3 Monte Carlo method to reproduce the true energy spectrum of charged particles

In the proposed method, charged particles are generated randomly in the foil of given thickness and are transported to the exit of the foil. At the exit of the foil, they are weighted with the given measured spectrum, transported back to their origin, and counted with their respective weighted fractions. The flow chart of the proposed method has been given in the fig. 7.2. The steps that have been followed in the proposed method are explained below;

1) A charged particles radiation detector measures the energy spectrum of charged particles which is downgraded in the energy and number of particles due to the loss of energy of charged particles and loss of charged particles in the target foil while escaping the foil. The measured spectrum from the radiation detector is binned and read as $E_m(i)$ (measured energy) and $S_m(i)$ (measured cross section). In the present work, the measured spectrum has been simulated with the GEANT-4.1 code.

2) In this step, the differential scattering cross section data of charged particles interaction with the atoms of the foil have been calculated. A charged particle interacts with the foil atoms via the multiple scattering [118] and absorption. For the multiple scattering, Rutherford scattering [119] differential cross section has been calculated with the following formula;

$$\frac{d\sigma}{d\theta} = \pi D^2 \frac{Cos(\theta)}{Sin^3(\theta)} \tag{7.7}$$

$$D = zZ\frac{e^2}{4\pi\varepsilon_0 T} \quad (7.8)$$

Where z is the atomic number of produced charged particles, Z is the atomic number of target foil, θ is the scattering angle, T is the kinetic energy of charged particles and D is the closest approach of charged particles to the atoms of target foil. The absorption cross section of charged particles has also been checked using the TALYS code and experimental data from the EXFOR data library. Their contribution comes out to be very less, hence have not been considered in the transport of the charged particles in this work. The scattering differential cross section predicts the infinite value of cross section at 0^0 and 360^0 thus scattering differential cross section has been calculated at 0.05^0 to 359.95^0 for the initial energies of charged particles and stored in a text file for their further use in the particle transport.

3) The charged particles are generated randomly in the foil with the position (x_0, y_0) and energy, E_0. Following this, the charged particles are transported in the foil. The first step in their transport is the generation of scattering angles based on the differential scattering cross section at different incident energies of charged particles. The generation of scattering angles has been carried out with the interpolation method of the Locate function [120] using the calculated scattering differential cross section. The second step is the calculations of scattering cross section at incident energy E_0, and scattering angle θ, which have been again calculated with the Eq. 7.7, 7.8. The third step is the calculation of stopping power of charged particles ($\frac{dE}{dx}$) for the initial energy E_0. The stopping power of charged particles is calculated with the SRIM code [102]. The energy straggling has also been considered in the calculation of stopping power. The fourth step is the successive interactions of charged particles with the atoms of

target foils. For each interaction of the charged particle with the atoms of target foil, mean free path (MFP) and true flight path (TFP) have been calculated with the given formulas;

$$MFP = \frac{1}{N_0 . \frac{d\sigma}{d\theta}} \tag{7.9}$$

At higher scattering (10^0 - 180^0), mean free path becomes large and energy loss in that interaction becomes high. This large mean free path is sometimes larger than a few microns and results in high energy loss in that subsequent step. This high energy loss in one step of interaction results in the high statistical uncertainty in the spread of energy loss. To decrease this spread in the energy loss, this mean free path is corrected to true flight path (TFP) if MFP is more than 0.1 μm. The true flight path (TFP) has been calculated and used instead of the mean free path for the condition of MFP > 0.1 μm in the transport equations. The formulas that have been used to calculate TFP [118] have been given below;

$$TFP = -MFP(n).\log\left(1 - z_0\left(\frac{1}{mfp(n)}\right)\right) \tag{7.10}$$

$$z_0 = MFP(n-1).\left[1 - \exp\left(\frac{t_0}{MFP(n-1)}\right)\right] \tag{7.11}$$

$$t_0 = \frac{MFP(n-1) - MFP(n)}{a0.MFP(n-1)} \tag{7.12}$$

$$a0 = \frac{1}{r0} \tag{7.13}$$

$$r0 = \frac{ei}{\left(\frac{dE}{dx}\right)} \tag{7.14}$$

Where z_0 is the geometrical mean path, t_0 is the average true flight path, r_0 is the range of charged particles in the target foil, n is the number of interactions during transport of charged particles in the foil, and $\frac{dE}{dx}$ is the stopping power of charged particles in the target foil. After each interaction, X_0, Y_0, and E_0 becomes X_i, Y_i, and E_i as follow;

$$E_i=E_0-\frac{dE}{dx}*TFP \quad (7.15)$$

$$X_i=X_0+TFP*\cos(\theta) \quad (7.16)$$

$$Y_i=Y_0+TFP*\sin(\theta) \quad (7.17)$$

Where (X_0, Y_0) is the origin coordinates of the charged particles. After each interaction, a charged particle shifts to a new location (X_i, Y_i) with decreased energy (E_i). These calculations are repeated until either the energy of a charged particle becomes zero or it leaves the foil. When it leaves the foil ($X_i \geq$ thickness of the foil), its final energy (E_f) and final location (X_f,Y_f) are stored. This step is referred to as the forward transport step in the upcoming sections of this paper.

4) Now particles, that have escaped the foil in the previous step, are transported back to their origin from (X_f,Y_f), and with energy E_f. In this step, the energy of charged particles increases after each step and particle shift to a new location (X_i,Y_i) as;

$$E_{Rep}= E_f + \frac{dE}{dx}*TFP \quad (7.18)$$

$$X_i= X_f-TFP*\cos(\theta) \quad (7.19)$$

$$Y_i= Y_f-TFP*\sin(\theta) \quad (7.20)$$

Here, (X_f, Y_f) is the final position of the charged particle at the end of the forward transport step. The charged particles gain energy until they reach their origin ($X_i \leq X_0$) and their final energy at the end of this step is the reproduced true energy (E_{rep}). Any particle that is absorbed during the forward transport of charged particles will have the reproduced energy equal to the initial energy with which it is produced in the foil at the beginning of the forward transport step. The initial energy, final energy, reproduced energy and their locations have been saved in the text file. This step is referred to as the backward transport step in the upcoming section of this paper.

5) The final energy data (E_f) at the exit of the foil at the end of forward transport step are binned and divided with the measured spectrum (S_n) of the same bin to have the weightage of each particle in the transport. Any particle that is absorbed during the forward transport, will be weighted with the lowest energy bin of the measured energy spectrum, hence will decrease the noise in the low energy spectrum region. Now, reproduced true energy data (E_{rep}) from backward transport step have also been binned and counted with the weightage of each particle to reconstruct the true energy spectrum of charged particles.

The method has been implemented with the FORTRAN language and flowchart of the proposed method is given in Fig 7.2.

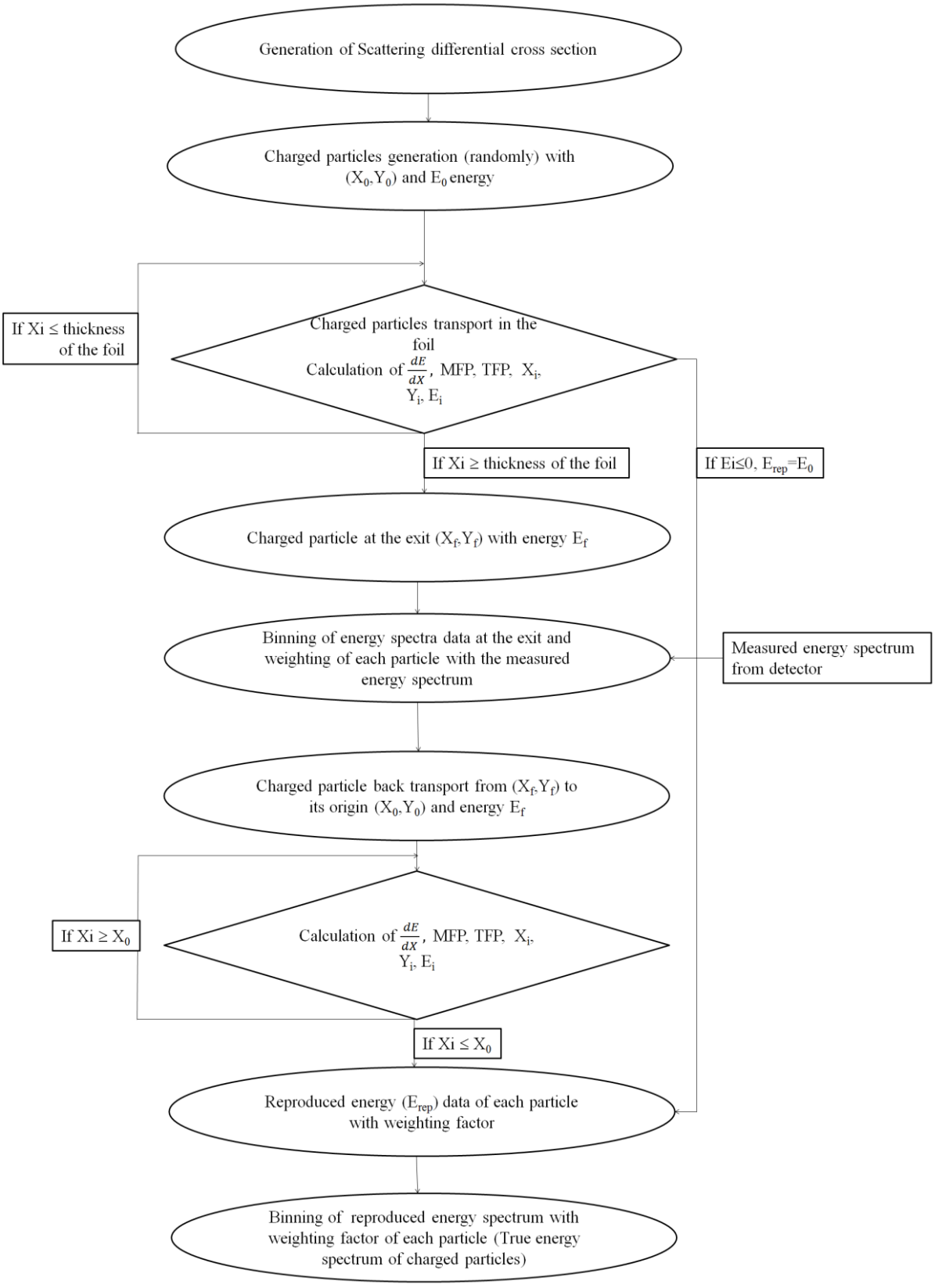

Fig. 7.2 Flow chart of Monte Carlo based transport code for the energy loss correction

7.4 Validation of method, results, and discussions

7.4.1 True energy spectrum of alpha particles

In the proposed method, the energy loss of charged particles is calculated for each interaction between charged particles and atoms of the foil, thus it predicts energy loss of charged particles more accurately as compared to be calculated with single incident energy. After each interaction, the energy of charged particle decreases and in its next interaction, its stopping power is again calculated with the decreased energy. As per the Bethe Bloch formula, the stopping power increases with the decrease in the energy of incident charged particles [102]. Pomp et al [30], Rezentes et al [28], and Slypen et al [29] had calculated the response function of energy loss data based on single incident energy. They had not considered the successive interactions of charged particles thus the subsequent increase of stopping power as the energy of charged particles decreases, had not been considered. Soderberg et al [27] had calculated the energy loss in successive steps in their method. Alpha particles lose energy and get absorbed due to their high stopping power in target foils. To validate our method, we have used the DDX data of outgoing alpha particles from $^{56}Fe(n,x\alpha)$ reaction channel for the neutron irradiation of 175 MeV. This DDX cross section is calculated with the TALYS-1.8 code [18] and considered as the true energy spectrum of alpha particles. In the present work, the measured spectrum has been simulated with the GEANT-4.1 [121]. In GEANT-4.1 simulations, alpha particles are generated randomly in the iron foil of 221 μm thickness and their energies at the exit of the target foil are calculated using the GEANT-4.1. These randomly produced alpha particles are binned and weighted with the true

spectrum of the TALYS code. Each particle is counted with their respective weightage factor at the end of the foil to have measured spectrum with the GEANT-4.1 code. Pomp et al [30] had also used the similar cross section data of alpha particles as the true energy spectrum and transported this data in 200 μm thick iron foil with the TARGSIM code [30]. Pomp et al had calculated the measured data at 45^0 to the foil, thus the effective thickness of the foil for the transport becomes 221 μm. TARGSIM code is a Monte Carlo transport code which is based on the methodology of the GEANT-3.21 [121]. The measured spectrum of alpha particles from GEANT-4.1 and Pomp et al comes out to be same as both follow the similar methodology. The measured energy spectrum from GEANT-4.1 has been corrected with the proposed method. The reproduced true energy spectrum or corrected energy spectrum with the proposed method have been compared with the true spectrum of TALYS code and presented in Fig. 7.3. The reproduced spectrum compares very well with the true spectrum. The calculations have been carried out with the 1 million incident particles.

The energy loss of charged particles is a statistical process that results in the spread of the energy deposition in each interaction and this spread is known as straggling. This spread in the energy loss is minimized by implementing the concept of a true flight path. To check the spread in the energy loss, alpha particles of 5 MeV and 100 MeV energy have been transported in the iron foil of 5 μm and 100 μm, respectively with the proposed algorithm. The alpha particles have been simulated from x=0 to the exit of both the foil and their true energy are reconstructed with the proposed algorithm. The full width at half maximum (FWHM) of the reconstructed spectrum comes out to be ~1.4 keV for both the energies. For continuous spectra of charged particles, the number of particles in each bin and size of energy bin are key factors in minimizing the standard

deviation and relative error in these calculations. The standard deviation and relative error have been calculated using the following formulas for the continuous spectrum;

$$\text{Std}=\sqrt{\frac{1}{N}(E_{Rep}-E_m)} \tag{7.20}$$

$$E_m=\frac{1}{N}(E_{Rep1}+E_{Rep2}+\ldots\ldots+E_{Repn}) \tag{7.21}$$

$$\text{R.E}=\frac{1}{E_{mean}}\sqrt{\frac{\text{Std}^2}{(N)}} \tag{7.22}$$

Here, Std is the standard deviation in the calculation, E_{Rep} is the reproduced true energy, E_m is the mean of randomly reproduced true energies in an energy bin, N is the number of particles in each energy bin, and R.E. is the relative error in the calculation. In the present work, the R.E per unit mean value has been calculated for different numbers of particles and different energy bin sizes. In the energy spectrum of alpha particles, different bin sizes of 1 MeV, 2.5 MeV and 5 MeV have been used in the calculations. The relative error is calculated for the total particles of 10^4, 10^5 and 10^6 with different bin sizes and results have been presented the results in Table 7.1. The relative error comes out to be higher for larger bin sizes. Increasing the number of particles in each bin and reducing the energy bin width in the reproduced spectrum reduce the relative error. In order to select the smaller bin size, the measured data from the detector also needs to be rebinned to the reduced bin size to calculate the weightage of all the charged particles. An important point is to be noted in the calculation of relative error that it only includes the statistical error that gets added into the reproduced energy spectrum due to the processing of measured data. Other experimental errors will remain same and need to be addressed with the reproduced data if any. In the reproduction of true energy

spectrum of alpha particles, 10^6 particles have been generated uniformly in the foil with the energy bin width of 1 MeV.

Table 7.1: Standard deviation and relative error for different bin sizes with different numbers of particles

Energy bin size	Standard deviation			Relative error (%)/mean value		
	10^4 particles	10^5 particles	10^6 particles	10^4 particles	10^5 particles	10^6 particles
1 MeV	0.294	0.29	0.26	3.764	1.174	0.332
2.5 MeV	0.73	0.72	0.69299	9.346	2.915	0.887
5 MeV	1.44	1.423	1.417	18.437	5.761	1.814

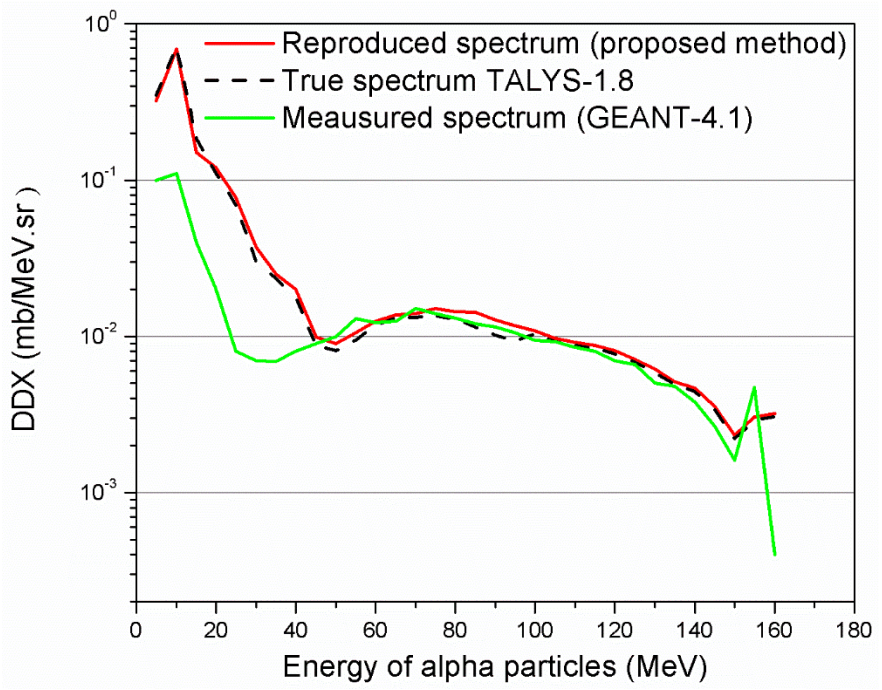

Fig. 7.3 Comparison of the reproduced spectrum and true spectrum for alpha particles production in iron foil of 221 μm. Green line represents the measured spectrum,

simulated with Geant4.1, black dashed line is the true spectrum calculated with the TALYS-1.8 code and red line represents the reproduced energy spectrum with the proposed method.

Johnson et al. [74] had measured the DDX data of alpha particles from $^{12}C(n,x\alpha)$ reaction channel for the neutron irradiation of 39.7 MeV using the ΔE-E silicon surface barrier detectors. The true energy spectra from the same measured spectra has been reproduced by Slypen et al, Rezentes et al, and Soderberg et al. True energy spectra of the same measured spectrum of alpha particles have been reproduced with the proposed method and compared with the results of Slypen et al, Rezentes et al, and Soderberg et al.. Rezentes et al., Slypen et al. and Soderberg et al. had reproduced true energy spectrum based on the solution of Fredholm equation. Soderberg et al. have also considered the successive interactions of charged particles in their approach. The comparison of the proposed method with the other three methods has been presented in Fig. 7.4. The proposed method predicts results similar to Slypen et al. but predicts lower true energy spectrum in the range of 4-5 MeV compared to the reproduced energy spectrum of Rezentes et al and Soderberg et al. Rezentes et al upgraded the method of Johnson et al and reproduced the true energy spectrum based on a small strip method. In their approach, Rezentes et al and Johnson et al divided the target foil into the small strips of thickness dt and integrate the measured spectrum for the entire thickness of the foil with the lower limit as the least measurable energy or threshold energy of the detector setup. This results in the overestimation of energy distribution near to the lowest measurable energy or threshold energy of detector setup. Soderberg et al had calculated the true spectrum in two steps; 1) in the first step, Soderberg et al calculated the energy shift ΔE, based on the measured energy from each energy bin, and add this

shift in the measured spectrum. 2) Soderberg et al had calculated the fraction of particles that are absorbed in the foil and used this fraction to get the lost particles correction factor in the true energy spectrum. Soderberg et al had used the robust energy loss calculation procedure and also considered multiple scattering and energy straggling. In the region of low energy alpha particles where it could not reach the detector, energy bins of such particles in the reproduced energy spectrum overlap with the threshold energy of detector in true energy spectrum calculations, which is 4 MeV in this case. This results in the overestimation of the energy spectrum near to detector threshold energy. The reconstructed energy spectrum with the proposed method compares well with the results of Slypen et al. Slypen et al. had considered the detector cut off energies in its calculation of lost particle correction thus does not overestimate the data at the lower energies. Soderberg et al had not rebinned the experimental data in its approach that results in the large statistical errors in their approach while Slypen et al had rebinned the large binned experimental data to the smaller binned data and then reconstruct the true spectrum. The rebinning of measured data to the smaller bins results in the smoothening the reconstructed true energy spectrum. The energy loss of charged particle considering multiple scattering predicts higher energy loss compared to the energy loss predicted with the single incident energy. The final Energy of 5 MeV and 100 MeV incident alpha particles in 5 μm and 100 μm thick iron foils, respectively comes out be 2.850 MeV and 95.41 MeV with multiple scattering method whereas final energy predicted by single incident energy comes out 3.133 MeV and 95.48 MeV for the same. At lower energies, the difference in the energy loss predicted by both the approaches is higher whereas, at higher energies, this difference is negligible. In the present work, if the particle is lost in its transport during the forward transport step then

its true energy with which it has been produced at the beginning of the forward transport is considered as its reproduced energy. Later all the particles are binned at the exit of the foil and weightage of each particle have been calculated with the given measured spectrum.

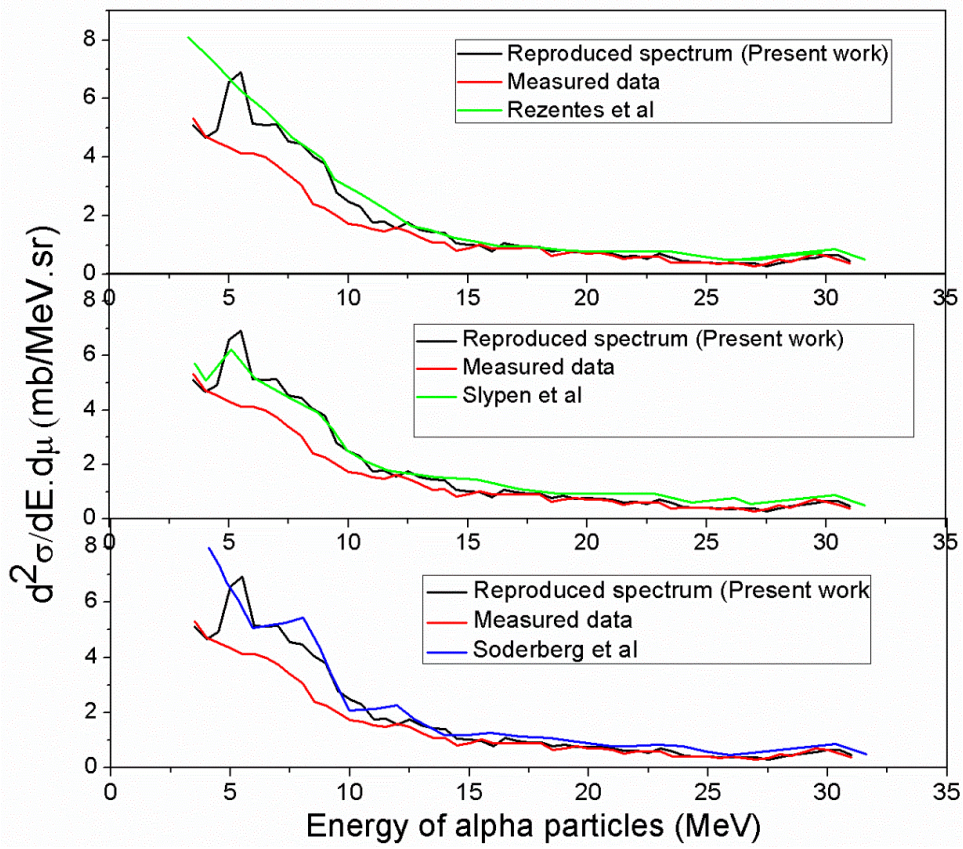

Fig.7.4 Comparison of present method with the methods of Rezentes et al, Slypen et al and Soderberg et al.

7.4.2 True energy spectrum of protons

Similarly, protons also lose a fraction of their energy and particles while transporting through target foils. The true energy spectra of protons are also reproduced to check the applicability of the proposed method for other charged particle species. Similar calculations for the reproduction of true energy spectrum of protons have also been

performed using the proposed method. The energy differential cross section data (EDX) of outgoing protons from $^{56}Fe(n,xp)$ reaction channel at 20 MeV incident neutrons have been calculated with the TALYS code. The EDX data from TALYS code have been considered as true energy spectrum of protons. Uniformly generated protons are transported in the iron foil of 200 µm thickness with the GEANT-4.1 code. Data at the exit have been converted to the measured spectrum using the same approach that has been carried out for alpha particles. The transported data from the GEANT-4.1 have been used to reproduce the true spectrum of protons with the proposed method and reported in fig. 7.5. The proposed method successfully reproduces the true energy spectrum of protons which compares very well with the true spectrum (TALYS data in this case). The reproduction of the energy spectrum of protons has also been carried out using the 10^6 particles with the energy bin size of 1 MeV.

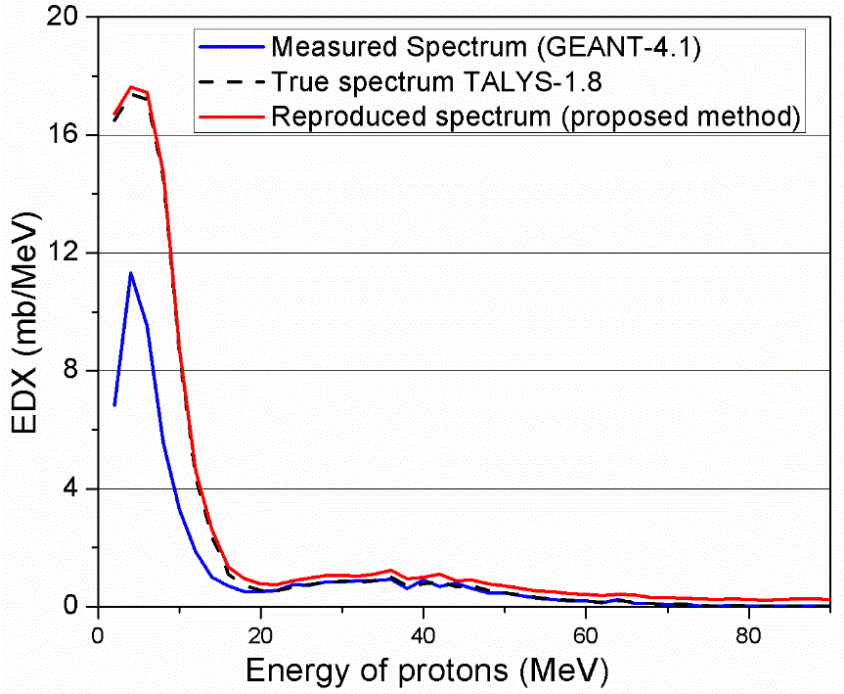

Fig. 7.5 Comparison of the reproduced spectrum and true spectrum for protons production in iron foil of 200 µm. blue line represents the measured spectrum,

simulated with Geant4.1, dashed black line represents true energy spectrum of protons, calculated with TALYS-1.8 and red line represents the reproduced true energy spectrum, calculated with the proposed method.

7.5 Summary

In the present thesis, a Monte Carlo method based on the transport of charged particles has been developed to reproduce the true energy spectrum of charged particles from the measured energy spectrum. This method has been validated with the charged particle transport code, GEANT-4.1 and nuclear reaction data code TALYS-1.8 for alpha particles and protons. The reported method sucessfully produce the true spectrum of charged particles from neutron induced reactions. The true energy spectra of alpha particles are reconstructed from the measured energy spectra of neutron induced reactions on carbon foil of 0.0186 mm thickness at 39.7 MeV energy incident neutrons. This calculated true spectrum has been compared with the results of Rezentes et al, Slypen et al and Soderberg et al. The reconstructed true energy spectra of alpha particles compare well with the results of Slypen et al. Slypen et al had considered the detector threshold energy in its calculations thus didn't overestimate the data near to detector threshold energy. The methods of Soderberg et al and Rezentes et al overestimate the true spectrum near to the detector threshold energy compared with the proposed method. High numbers of incident particles in the energy bin and smaller energy bin size reduce the statistical error to the minimum in these calculations. The proposed method can be used to calculate the true spectrum from the given measured spectrum of different charged particles.

CHAPTER: 8 SUMMARY AND FUTURE WORK

Fusion reactors are the endless energy source to produce electricity due to the availability of nuclear fuel. Deuterium (D) and tritium (T) are chosen as the primary constituents of nuclear fuel to be used in the fusion reactors due to their higher reaction cross-section, low threshold energy, and higher energy release compared to other nuclear fusion reactions. The D-T reaction produces 14.1 MeV neutron and 3.5 MeV alpha particle and these outgoing neutrons induce nuclear responses like transmutation, gas production and displacement damage in fusion reactor materials. These nuclear responses have adverse effects on the microstructural and engineering properties of reactor materials. It is important to quantify these responses accurately to design an economically viable fusion reactor. The typical fusion reactor materials presently proposed are iron, tungsten, and chromium where iron and chromium are used as the structural materials and tungsten is used to take high heat load as the divertor material. In the earlier studies of transmutation and gas production, the time evolution of inventory build-up of overall elemental change in the concentration of reactor materials, helium production in iron, chromium and tungsten, and hydrogen production in iron were reported. The time evolution of transmutated isotopes including the radioactive ones and hydrogen production in tungsten and chromium were not reported. In the earlier studies of displacement damage, molecular dynamics simulations of displacement cascade were carried out in iron and tungsten. The energy loss of recoil atom (PKA) in electronic excitation was not included in the earlier MD simulations of iron, thus it overestimated the numbers of Frenkel pairs. The MD simulations of damage cascade were not carried out for pure chromium. Most of the earlier estimations of dpa

in fusion reactor material were carried out using the NRT method which has some well-known limitations in its approach.

In the present thesis, these three nuclear responses have been studied using the appropriate nuclear models and advance radiation damage mechanisms. To calculate the transmutation and gas production, nuclear cross-section data of all the open reaction channels are required. These cross-section data either can be taken from the evaluated data libraries such as ENDF and TENDL or can be calculated with the nuclear reaction code TALYS-1.8. The nuclear models are optimized for each element of our interest to reproduce the available experimental data. These best-fitted models are used to predict the cross section of all the open reaction channels for the D-T neutron spectra to estimate the nuclear responses. The discrepancies between the nuclear cross-sections from the evaluated nuclear data and experimental data libraries have been identified and compared with the data obtained through the best fitted nuclear models. Helium and hydrogen production cross-section of iron, chromium, and tungsten are calculated and based on that, gas production per atom (GPA) in iron, chromium, and tungsten is predicted for typical D-T neutron spectra of fusion reactors. Hydrogen production in tungsten and chromium is reported for the first time in this thesis. It is identified that hydrogen production is a dominant mechanism in chromium. The production of important transmutated isotopes has been studied in all the stable isotopes of iron, tungsten, and chromium using the ACTYS code. The time evolution of transmutated isotopes including the radioactive ones is reported. It is found that the production of tungsten isotope, ^{183}W is not saturating even after the 5 full power year (FPY) due to its production from ^{182}W and ^{184}W through (n,γ) and (n,2n) reaction channels, respectively. This study of transmutation in chromium reveals that the concentration of ^{52}Cr

decreases to 67% in 5 FPY operations at the first wall location of the EU DEMO. Its original concentration is 83% in natural chromium. A similar assessment of transmutated impurities is carried out for all stable isotopes of iron. To predict the displacement damage for a given neutron energy spectra, the energy spectra of recoils and quantification of Frenkel pairs due to the energetic recoil atoms are the two essential input parameters. In this thesis, the energy spectra of recoils from all the stable isotopes of iron, tungsten, and chromium are calculated with the TALYS-1.8 code using the best fitted nuclear models. Molecular dynamics simulations of damage cascade of self PKA of up to 200 keV damage energies in iron, chromium, and tungsten are carried out to predict the number of Frenkel pairs using the LAMMPS code. The time evolution of Frenkel pairs has also been studied and discussed. In the MD simulations of iron and tungsten, the energy loss of PKA in electronic excitation is calculated with the Lindhard-Scharff-Schiott (LSS) function and is included in the MD simulations. The MD simulation of self PKA in pure chromium is carried out for the first time and energy loss of the PKA in electronic excitation is predicted with the two-temperature model of the MD simulations. The results obtained from MD simulations have been used to calibrate the constant parameters of the Arc-dpa method. The displacement damage cross section has been calculated for the neutron irradiation of up to 15 MeV energy with the NRT and arc-dpa methods. The values of dpa in iron, chromium, and tungsten are predicted for the typical D-T neutron spectra of fusion reactors using the MD simulations data and Arc-dpa method for the first time in this thesis. The dpa (arc-dpa)/FPY in iron, tungsten, and chromium at the first wall location of EU DEMO comes out to be 1.19, 0.93 and 1.13, respectively.

To validate the nuclear models, the energy spectra of outgoing charged particles are required. The measured energy spectra of charged particles are degraded in energy and number of particles due to the loss of energy and particles within the target foil itself. Thus, the measured energy spectra of outgoing charged particles need to be corrected to have the true energy spectrum. A Monte-Carlo method based on the transport of charged particles is developed and validated with GEANT-4.1. This method includes multiple scattering and the concept of true flight path in its approach. This method has been compared with the existing methods used in earlier experiments. The inclusion of the threshold energy of the detector set up in the proposed method reduces noise at the lower energy region of outgoing charged particles.

Long term effects of transmutation, gas production and displacement damage in iron, tungsten and chromium, and their effects on their microstructural and engineering properties can be studied in the future. The effects of the produced gas products on the reactor material e.g. iron, chromium and tungsten can also be studied as a future work of this thesis. Ion irradiation studies using the surrogate method are also planned to further study the displacement damage. Similar studies can also be extended to the high entropy metallic alloys. The experimental measurements of the differential cross section of charged particles for fusion reactor materials are also planned as the future work of this thesis. In these experimental measurements of the differential cross section, the true energy spectrum of charged particles will be reconstructed with the developed method explained in chapter 7. The validation tests of the calculated nuclear cross section data against the integral benchmark experiments can also be performed as a future study of this thesis.

BIBLIOGRAPHY

[1] G. McCracken and P. Stott, Fusion, Academic press pp. 1–5, 2007, https://doi.org/10.1016/B978-012481851-4/50003-2.

[2] "Nuclear engineering theory and technology of commercial nuclear power," *Environ. Int.*, vol. 19, no. 2, p. 214, 2003.

[3] Zohuri, Bahman, Inertial Confinement Fusion Driven Thermonuclear Energy, Springer, pp 31-45 2017.

[4] C Huang, "Magnetic confinement fusion : a brief review,", Springer, vol. 3, pp. 1–9, 2018.

[5] Y.C. Saxena and SST-1 Team, *Nuclear Fusion*, Vol 40, pp.12, 2000.

[6] R.L. Tanna1, J. Ghosh et al. *Nuclear Fusion*, Volume 57, pp. 10 2017.

[7] F. Romanelli et al. *Nuclear Fusion*, Volume 49, pp. 10 2009.

[8] K. Tomabechi, J. R. Gilleland, Y. A. Sokolov, and R. Toschi, *Nucl. Fusion*, vol. 31, no. 6, pp. 1135–1224, 1991.

[9] M. R. Gilbert, T. Eade, C. Bachmann, U. Fischer, and N. P. Taylor, *Nucl. Fusion*, vol. 57, pp. 4, 2017.

[10] M. R. Gilbert and J. C. Sublet *Nucl. Fusion*, vol. 51, pp 4, 2011.

[11] H. Iida, V. Khripunov, and L. Petrizzi, "Nuclear Analysis Report-2003," pp. 229, 2001.

[12] M. R. Gilbert, S. L. Dudarev, S. Zheng, L. W. Packer, and J. C. Sublet, *Nucl. Fusion*, vol. 52, pp. 8, 2012.

[13] V. Valkovic, "14 MeV Neutrons: Physics and Applications", CRC press 1st Edition pp. 31-121 2015.

[14] Gilbert et al, *J. Nucl. Mater.*, vol. 504 pp. 101-108 2018 .

[15] M. R. Gilbert, J. Marian, and J. C. Sublet, *J. Nucl. Mater.*, vol. 467, pp. 121–134, 2015.

[16] U. Fischer, C. Bachmann, I. Palermo, P. Pereslavtsev, and R. Villari, *Fusion Eng. Des.*, vol. 98–99, pp. 2134–2137, 2015.

[17] Y. Iwamoto, H. Iwamoto, M. Harada, and K. Niita, *J. Nucl. Sci. Technol.*, vol. 51, no. 1, pp. 98–107, 2014.

[18] A. J. Koning and D. Rochman, *Nucl. Data Sheets*, vol. 113, no. 12, pp. 2841–2934, 2012.

[19] T. Noda, M. Fujita, and M. Okada, *J. Nucl. Mater.*, vol. 258–263, pp. 934–939, 1998.

[20] M. Fujitsuka et al., *J. Nucl. Mater*, vol. 283, pp. 1148-1151, 2000.

[21] T. Tanno et al., *J. Nucl. Mater.*, vol. 386–388, pp. 218–221, 2009.

[22] M. R. Gilbert, S. L. Dudarev, D. Nguyen-Manh, S. Zheng, L. W. Packer, and J. C. Sublet, J. Nucl. Mater., vol. 442, pp 1 2013.

[23] M. I. Norgett and M. T. Robinson et al., *Nucl. Eng. Des.*, vol. 33, pp. 50–54, 1975.

[24] L. Luneville and D. Simeone, *EPJ Web Conf.*, vol. 115, pp. 20, 2016.

[25] K. Nordlund et al., *Nat. Commun*., vol. 9, no. 1, pp. 1–8, 2018.

[26] J. Fikar and R. Schäublin, *J. Nucl. Mater.*, vol. 386, pp. 97–101, 2009.

[27] J. Söderberg, S. Dangtip et al., *Nucl. Instruments Methods Phys. Res. Sect. B Beam Interact. with Mater. Atoms*, vol. 195, no. 3–4, pp. 426–434, 2002.

[28] Rezentes et al., *Nuclear Instruments and Methods in Physics Research A*, vol. 361, pp. 574-580 1995.

[29] I. Slypen et al., *Nucl. Phys. A*, vol. 726, no. 3–4, pp. 210–230, 2003.

[30] S. Pomp and U. Tippawan, *Nucl. Instruments Methods Phys. Res. Sect. A Accel. Spectrometers, Detect. Assoc. Equip*., vol. 572, no. 2, pp. 893–898, 2007.

[31] G. F. Knoll et al., "Radiation Detection and Measurement john", Wiley and sons, 3rd edition, pp. 165-190, 2000.

[32] A. Koning et al., *Nuclear Data Sheets*, vol. 1132, pp. 841-2934, 2012.

[33] M. Herman et al., *Nucl. Data Sheets*, vol. 148, pp. 214–253, 2018.

[34] H. Wienke et al., *Nucl. Data Sheets*, vol. 108, no. 12, pp. 2655–2715, 2008.

[35] S. M. Grimes, R. C. Haight, K. R. Alvar, H. H. Barschall, and R. R. Borchers *Phys. Rev. C*, vol. 19, pp. 2127-2235, 1979.

[36] Neutron Generators for Analytical Purposes, *IAEA Techdoc-1535*, 2012.

[37] Use of Accelerator Based Neutron Sources, *IAEA-Techdoc-1153*, 2000.

[38] K. Kondo et al., *Fusion Eng. Des.*, vol. 81, pp. 8-14, 2006.

[39] B. Lalremruata, S. D. Dhole, S. Ganesan, and V. N. Bhoraskar, *Nucl. Phys. A*, vol. 821, no. 1–4, pp. 23–35, 2009.

[40] Kokoo, I. Murata, and A. Takahashi *Nucl. Sci. Eng.*, vol. 132, no. 1, pp. 16–29, 2017.

[41] D.A. Brown, M.B. Chadwick et al., *Nuclear Data Sheets,* vol. 148, pp. 1–142, 2018.

[42] D. Rochman and A. J. Koning, "TENDL-2011 : TALYS-based Evaluated Nuclear Data Library," 2012.

[43] P. Batistoni et al., "Validation of FENDL-2.1 nuclear data library for use in ITER nuclear analysis," pp. 1–4, 2008.

[44] Experimental Nuclear Reaction Data (EXFOR), database version-4/2019, https://www-nds.iaea.org › exfor, 2019.

[45] R. E. Macfarlane et al., "The NJOY Nuclear Data Processing System, Version 2012," LA-UR-12-27079, Los Alamos Natl. Lab., 2012.

[46] J. Kopecky, "The European Activation File : EAF-2001 cross section library," 2001.

[47] S. M. Grimes, R. C. Haight, and J. D. Anderson, *Phys. Rev. C,* vol. 17, pp. 508, 1978.

[48] R. A. Forrest et al., "Nuclear data for fusion applications," *International Conference on Nuclear Data for Science and Technology*, 2007.

[49] U. Fischer et al., *Fusion Eng. Des.*, vol. 37, Issue 1, pp. 9-21, 1997.

[50] T. Bohm et al., *Nucl. Data Sheets*, vol. 120, pp. 230–234, 2014.

[51] M. Harmen et al., "ENDF-6 Formats Manual", CSEWG Document ENDF-102, report BNL-90365, 2010.

[52] M. R. Gilbert, J. Marian, and J. C. Sublet, *J. Nucl. Mater.*, vol. 467, pp. 121–134, 2015.

[53] L. R. Greenwood, "SPECTER computer code for radiation damage calculations," *Proc. of an IAEA Consult. Meet. on Nucl. Data for Radiation Damage Estimates for Reactor Struct. Mater*., Santa Fe, New Mexico, pp. 13, 1986.

[54] Jerzy Cetnar et al., *Annals of Nuclear Energy*, vol. 33, no. 7, pp. 640-645, 2006.

[55] P. Kanth, S. C. Tadepalli, and P. V. Subhash, *Nucl. Fusion*, vol. 58, no. 12, 2018.

[56] J. W. Eastwood and J. G. Morgan, The FISPACT -II User Manual, no. 6. 2014.

[57] M. R. Gilbert, S. L. Dudarev, D. Nguyen-Manh, S. Zheng, L. W. Packer, and J. C. Sublet, *J. Nucl. Mater.*, vol. 442, no. 1-3, pp. 755–760, 2013.

[58] M. R. Gilbert and R. A. Forrest, "Handbook of activation , transmutation , and radiation damage properties of the elements simulated using FISPACT-II & TENDL-2014 ;," December, 2015.

[59] C. B. A. Forty, G. J. Butterworth, and J. C. Sublet, *J. Nucl. Mater.*, vol. 212–215, pp. 640–643, 1994.

[60] M. Kinchin and P. Model, "Modified Kinchin-Pease Model," pp. 144–145.

[61] James F. Ziegler et al., *Nuclear Instruments and Methods in Physics Research Section B: Beam Interactions with Materials and Atoms*, vol. 268, no. 11, pp. 1818-1823 (2010).

[62] J. Chang, J. Y. Cho, C. S. Gil, and W. J. Lee, *Nucl. Eng. Technol.*, vol. 46, no. 4, pp. 475–480, 2014.

[63] C. H. M. Broeders, A. Y. Konobeyev, and C. Villagrasa, *J. Nucl. Mater.*, vol. 342, no. 1–3, pp. 68–76, 2005.

[64] H. L. Heinisch, L. R. Greenwood, W. J. Weber, and R. E. Williford, *J. Nucl. Mater.*, vol. 307–311, pp. 895–899, 2002.

[65] C. H. M. Broeders and A. Y. Konobeyev, *J. Nucl. Mater.*, vol. 336, no. 2–3, pp. 201–209, 2005.

[66] ASTM E693: Standard Practice for Characterizing Neutron Exposures in Iron and Low Alloy Steels in Terms of Displacements Per Atom (DPA) (ASTM International) 2006.

[67] F. Granberg et al., *J. Nucl. Mater.*, vol. 512, pp. 450–479, 2018.

[68] M. Warrier and M. C. Valsakumar, *Fusion Sci. Technol.*, vol. 65, no. 2, pp. 229–234, 2014.

[69] M. Warrier, A. Mutzke, U. Bhardwaj, R. Schneider, and H. Hemani, *J. Nucl. Mater.*, vol. 467, pp. 457–464, 2015.

[70] R.E. Stoller, A.F. Calder *J. Nucl. Mater.* vol. 283-287 pp. 746-752, 2000.

[71] A. Y. Konobeyev, U. Fischer, and S. P. Simakov, "Neutron Displacement Cross-Sections for Materials From Be To U Calculated Using the Arc-Dpa Concept," no. 1, pp. 0–9.

[72] A. Y. Konobeyev, U. Fischer, Y. A. Korovin, and S. P. Simakov, *Nucl. Energy Technol.*, vol. 3, no. 3, pp. 169–175, 2017.

[73] N. Tsoulfanidis et al., "Measurement detection of radiation", 4th Edition, CRC Press, pg. 330–336, 2010

[74] M. L. Johnson, J.L. Romero, T.S. Subramanian and F.P. Brady, *Nucl. Instrum. Meth. A*, vol. 169, pp. 179, 1980.

[75] V. Barabash et al., *J. Nucl. Mater.*, vol. 367-370, pp. 21–32, 2007.

[76] S. N. Ghoshal, *Phys. Rev.*, vol. 80, no. 6, pp. 939–942, 1950.

[77] C. Bertalni *Lect. Notes Phys*., vol. 812, no. 2, pp. 461–489, 2011.

[78] Kalbach, *Physical review C*, vol. 32, no. 4, pp. 111–144, 2018.

[79] R. Bonetti, M. B. Chadwick, P. E. Hodgson, B. V. Carlson, and M. S. Hussein, *Phys. Rep.*, vol. 202, no. 4, pp. 171–231, 1991.

[80] M. K. Grossjean and H. Feldmeier, *Nucl. Physics, Sect. A*, vol. 444, no. 1, pp. 113–132, 1985.

[81] P. Demetriou and S. Goriely, *Nucl. Phys. A*, vol. 695, no. 1–4, pp. 95–108, 2001.

[82] A. Gilbert et al., *Canadian Journal of Physics*. Vol. 43, p.1446, 1965.

[83] V. Avrigeanu et al., *Nucl. Phys. A*, vol. 765, no. 1–2, pp. 1–28, 2005.

[84] J. Koning, D. Rochman et al. TENDL-2017: TALYS-based evaluated nuclear data library, https://tendl.web.psi.ch/tendl_2017/tendl2017.html, 2017.

[85] Yu .E. Kozyr et al. *Soviet Journal of Nuclear Physics*, vol. 27, pp. 329-335 1978.

[86] G. Stengl et al., *Nuclear Physics Section A*, vol. 290, no. 1, pp. 109, 1977.

[87] T. Villaithong et al., *Nucl. Instrum. Methods in Physics Res Sect.A*, vol. 332, pp. 561, 1993.

[88] S. Matsuyama et al., *JAERI-M Reports No.92-027*, pp. 309, 1992.

[89] Takahashi et al., *Osaka Univ Oktavian Reports, No.92-01*, (1992).

[90] R. Fischer et al. *Physical Review C*, vol. 34, pp. 460-467 (1986).

[91] S. P. Simakov, SPKA code, FZK, 2007.

[92] A. Pavlik, et al., *Proc. Final Coordinated Research Meeting, RCM-3, on Measurements and Analysis of 14MeV Neutron Induced Double Differential Neutron Emission Cross Sections for Fission and Fusion Reactor Technology*, Chiang Mai, 1992.

[93] A. Marcinkowski, P. Demetriou, and P. E. Hodgson, *J. Phys. G*, vol. 22, no. 8, pp. 1219–1222, 1996.

[94] Lychagin et al., *Symp.on Nucleon Induced Reactions, Smolenice*, pp.272, 1988.

[95] R. C. Haight et al., *Nuclear Science and Engineering*, vol.124, pp.219, 1996.

[96] G. Federici et al., *Nucl. Fusion,* vol. 57, no. 9, 2017.

[97] R. Villari et al., *Fusion Eng. Des.*, vol. 88, no. 9–10, pp. 2006–2010, 2013.

[98] G. S. Was et al, Radiation damage to structural alloys in nuclear power plants: mechanisms and remediation, DOI: 10.1533/9780857097552.2.355.

[99] C. Lemaignan, "Nuclear Materials and Irradiation Effects In: Cacuci D.G. (eds) *Handbook of Nuclear Engineering*. Springer, Boston, MA."

[100] O. K. Chopra et al., *Journal of Nuclear Materials,* vol. 412, no. 1, pp. 195-208, 2011.

[101] M. Thuvander, "Lecture on ss hardening, swelling and creep." Chalmers University of Technology, , 2016.

[102] R. E. Stoller et al., *Nuclear Instruments and Methods in Physics Research Section B: Beam Interactions with Materials and Atoms,* vol. 310, pp. 75-80, 2013.

[103] R. E. Stoller, "Primary radiation damage formation," *Compr. Nucl. Mater.*, vol. 1, pp. 293–332, 2012.

[104] S. Plimpton, *Journal of Computational Physics*, vol. 117, no. 1. pp. 1–19, 1995.

[105] Zhou et al., *Acta Mater.,* vol. 49 no. 19, pp. 4005, 2001.

[106] Malerba et al. *Journal of Nuclear Materials*, vol. 406, no. 1, pp. 19-38, 2010.

[107] CA Howells et al., *Modelling Simul. Mater*. Sci. *Eng.*, vol. 26, pp. 85, 2018.

[108] J Lindhard et al. *Mat. Fys. Medd. Dan. Vid. Selsk.* vol. 33, pp. 1-42, 1963.

[109] A. M. Rutherford and D. M. Duffy, *J. Phys. Condens. Matter*, vol. 19, no. 49, pp. 0–9, 2007.

[110] Stukowski et al., *Modelling Simul. Mater. Sci. Eng*., vol. 18, pp. 150, 2010.

[111] K. Nordlund and R. S. Averback, *Physical review B*, vol. 56, no. 5, pp. 2421-2431, 1996.

[112] A. Grossfield and D. M. Zuckerman, *Annu. Rep. Comput. Chem.*, vol. 5, pp. 23–48, 2009.

[113] H. Flyvbjerg and H. G. Petersen, *J. Chem. Phys.*, vol. 91, no. 1, pp. 461–466, 1989.

[114] G. J. Ackland et al., *Computer Physics Communications*, vol. 182, no. 12, pp. 2587-2604, 2011.

[115] R. Orecchia et al., *Eur. J. Cancer*, vol. 34 , pp. 459, 1998.

[116] F. Ziegler, "Helium stopping power and ranges in all elements", Pergamon Press, Elmsford, New York, U.S.A., (1977)

[117] L.C. Northcliffe and R.F. Schilling, *Nucl. Data Tables A*, vol. 7, pp. 233, 1978.

[118] "Physics Reference Manual", Geant4 collaboration, Release 10.4, 2017.

[119] H. Paetz gen. Schieck, "Nuclear Reactions", *Lect. Notes Phys*., vol. 882, Springer-Verlag, 2014.

[120] Locate function, http://www.phys.ufl.edu/~coldwell/interpolation/Locate.htm

[121] J. Allison et al., *IEEE Trans. Nucl. Sci.*, vol. 53, pp. 270, 2008.